Spring 5-10-2019

Algorithmic Multi-Color CMOS Avalanche Photodiodes for Smart-Lighting Applications

Md Mottaleb Hossain
Doctoral Student, Optical Science and Engineering

Md Mottaleb Hossain

Candidate

Electrical & Computer Engineering

Department

This dissertation is approved, and it is acceptable in quality and form for publication:

Approved by the Dissertation Committee:

Daniel Feezell, Chairperson

Majeed M. Hayat, Research Advisor

Payman Zarkesh-Ha

Mansoor Sheik-Bahae

ALGORITHMIC MULTI-COLOR CMOS AVALANCHE PHOTODIODES FOR SMART-LIGHTING APPLICATIONS

by

MD MOTTALEB HOSSAIN

M.S., Optical Science & Engineering, 2015

The University of New Mexico, Albuquerque, NM, USA

B.S., Electrical & Electronic Engineering, 2009

Khulna University of Engineering & Technology, Khulna, Bangladesh

DISSERTATION
Submitted in Partial Fulfillment of the
Requirements for the Degree of

Doctor of Philosophy

Optical Science & Engineering

The University of New Mexico
Albuquerque, New Mexico, USA

May, 2019

Dedication

To my beloved parents, wife, and siblings

Acknowledgement

I would like to gratefully acknowledge my research and academic advisor, Prof. Majeed M. Hayat, for his proper guidance, support and inspiration throughout the entire research works. Dr. Hayat is currently a Professor and Department Chair of Electrical and Computer Engineering (ECE) at Marquette University, WI, USA. I am thankful to ECE Prof. Daniel Feezell for serving as my academic advisor after departure (August 2018) of my long term Ph.D. advisor, Dr. Hayat. Thanks a lot to the Lighting Enabled Systems & Applications-a National Science Foundation (NSF) Engineering Research Center (ERC) and Sandia Nationals Labs (SNL) for providing financial and technical support. I would also like to express my sincere gratitude to the following people who have enriched my academic and research accomplishments through their guidance and technical insights:

Dr. John P. R. David, Professor of EEE, University of Sheffield, UK

Dr. Steven R. J. Brueck, Distinguished Professor, Emeritus, CHTM, UNM, USA

Dr. Payman Zarkesh-Ha, Associate Professor of ECE, CHTM, UNM, USA

Dr. Mansoor Sheik-Bahae, Distinguished Professor of P & A, UNM, USA

Dr. Mona M. Hella, Professor of ECSE, RPI, USA

Dr. Sagar Ray, Sr. Analog/RF IC Design Engineer, Intel Corporation, CA

Dr. Pankaz Das, Postdoctoral Scholar of ECE, Marquette University, USA

Md. Rashidul Hasan, Ph.D. Candidate, Mathematics and Statistics, UNM

Dr, Samana Tasnim (spouse), Pharm.D., UNM College of Pharmacy, USA

Finally, I would like to thank to my parents (Md. Abdul Khaleq and Lucy Ara), siblings (Md. Abdul Kader, Md. Munir Hossain, and Munira Khatun), in-laws (Dr. Mohammad Ali, Shakinara Ali, and Fabiha Sabin), family and friends for their continuous support and encouragement.

Algorithmic Multi-Color CMOS Avalanche Photodiodes for Smart-Lighting Applications

By

Md Mottaleb Hossain

Ph.D., Optical Science & Engineering, 2019
The University of New Mexico, Albuquerque, NM, USA

M.S., Optical Science & Engineering, 2015
The University of New Mexico, Albuquerque, NM, USA

B.S., Electrical & Electronic Engineering, 2009
Khulna University of Engineering & Technology (KUET), Bangladesh

ABSTRACT

Future smart-lighting systems are expected to deliver adaptively color-tunable and high-quality lighting that is energy efficient while also offering integrated visible-light wireless communication services. To enable these systems at a commercial level, inexpensive and fast sensors with spectral-sensing capability are required. CMOS-compatible silicon avalanche photodiodes (APDs) can be an excellent fit to this problem due to their excellent sensitivity, high speeds and cost effectiveness; however, color sensing is a challenge without resorting to expensive spectral filters, as done in commercially. To address this challenge, we have recently designed and modeled a novel CMOS-compatible dual-junction APD. The device outputs two photocurrents simultaneously, one for each junction, and each junction is controlled independently via a

bias voltage so that each photocurrent can exhibit its own avalanche amplification factors and sensitivity. What is unique here is that each APD responds differently to different wavelengths because of (1) the wavelength-dependent nature of the light-absorption profile in the device, and (2) the dependence of the avalanche multiplication process on the location of photon absorptions (and hence on wavelength). The idea is to produce a series of photocurrent pairs, at judiciously prescribed pairs of biases for each acquisition, which would contain sufficient spectral information about the light as well as its intensity, which can be extracted from the data via an algorithm. Modeling shows that we can ideally use a pair of biases to detect the color and intensity within 10 nm spectral resolution in the 440-650 nm wavelength range using a maximum likelihood (ML) algorithm. In practice, however, the spectrum and intensity must be calculated from the series of measured photocurrent pairs using a ML algorithm, which would employ the wavelength and bias-voltage dependent joint probability density function (pdf) of the two photocurrents. The pdf accounts for both APDs' responsivities in the presence of Johnson (electronic amplifier) noise, dark current, and most importantly, the avalanche gain uncertainty, represented by the excess-noise factor at each wavelength.

We have designed a programmable, inexpensive (CMOS compatible) dual-junction silicon APD that outputs the intensity and spectrum of the sensed illumination that addresses the needs of smart lighting without the use of any spectral filters. The efforts include: (1) the computation of the mean gain, excess noise factor and avalanche breakdown voltage for the dual APD as a function of bias and wavelength, (2) development of an exact analytical formula for excess noise factor under mixed injection, and (3) development of an exhaustive computation of the ML estimates of the intensity

and spectral profile. The ML computations include an exhaustive search of a multidimensional space of wavelength and intensity values.

As mentioned earlier, each APD responds differently to different wavelengths due to the dependence of the avalanche multiplication process on the location of photon absorptions. This phenomenon leads to the mixed-injection avalanche multiplication process and the mean gain uncertainty, i.e., excess noise factor. Note that the well-known analytical formula for the excess noise factor associated with avalanche photodiodes (APDs), developed by R. J. McIntyre in 1966, assumes the injection of either an electron or a hole at the edge of the APD's avalanche region. This formula, however, is not applicable in cases when photons are absorbed inside the avalanche region, and its use may severely underestimate or overestimate the actual excess noise factor depending on the absorption profile and the hole-to-electron ionization coefficient ratio, *k*. Here, an easy-to-use exact analytical formula is derived for excess noise factor while taking into account a mixed-carrier initiated avalanche multiplication process, which is triggered by a parent electron-hole pair at an arbitrarily specified location within the multiplication region. In addition, an expression for the excess noise factor is presented in the case when the location of the parent electron-hole pair within the multiplication region obeys an arbitrary exponential distribution. The results show that in contrast to the case of edge parent-electron injection, when mixed injection is allowed even a small level of hole ionization (e.g., small k~0.0001) causes the excess noise factor to increase dramatic, depending on the absorption profile as it ranges from narrow to flat within the multiplication region. The theoretical results are validated against experimental results for Si APDs.

Table of Contents

List of Figures

List of Tables

Chapter 1

Introduction

1.1 Motivation

The future solid-state smart-lighting system is a promising technology which will deliver high quality, energy efficient, color tunable lighting and integrated wireless communication services automatically and with minimal human intervention [1]. The light sources and sensors are managed with robotic control architectures powered by new control algorithms that process networked sensor data to simultaneously optimize energy utilization and lighting system ergonomics (visual acuity, cognition, comfort and health, and wireless data access). The benefits include improved energy savings, human health and well-being, and greater worker productivity [1].

There is a need for the aforementioned emerging smart-lighting concepts for an inexpensive and high-speed spectral sensing capability to enable adaptive lighting (smart spaces) and visible-light communication [2]. One approach to address this need is to design and fabricate a novel CMOS-compatible, cost-effective, high-speed multi-junction Si avalanche-photodiode (APD) structure [3]. The novel color sensor will process light with right color and intensity which will enable automatic adjust of right lighting for us at any given time, optimized for human health and productivity. Aside from wavelength selectivity, the dual-junction device can provide wavelength-dependent photocurrent amplification to amplify any losses due to any filter-based selectivity as reported in literature [4]. This in turn will provide better noise performance over ordinary

photodiodes where thermal noise is a limiting factor. The use of avalanche gain to improve and unify responsivity across the visible spectrum is desirable because the gain is generated internally within the detector (without the need for external amplifiers), which offers an signal to noise ratio (SNR) advantage (without compromising speed) as well as simplicity of design.

Recently, color detection methods have been reported [5], [6] for the buried double-junction (BDJ) CMOS detector, without the need for any optical filters. The first method [5] took into account the ratio of the two photo-currents (from two photodiodes) at a very low reverse bias voltage which yields monotonically increasing function of the wavelength, resulting in wavelength determination. This method of color detection suffers from wavelength resolution. In this regard, the photo-current noise fluctuations were taken into account to determine minimum distinguishable wavelength difference, i.e., wavelength resolution [6]. However, this wavelength resolution degrades with the decrease in the incident signal level. Note that both of the methods took into account unity gain photo-current ratios for color determination. Therefore, a sophisticated spectral and light intensity detection method is required which takes into account APD gains at different bias voltages as well as photo-current noise fluctuations. The avalanche effect in silicon can be exploited to increase their responsivity while using dual-junctions to offer wavelength selectivity. This method can offer better wavelength resolution even at the presence of low level of incident signal.

In this dissertation report, we propose a simple, inexpensive and high responsivity CMOS-compatible dual-junction separate absorption and multiplication (SAM) APD (two APDs in tandem) to be operated in the linear avalanche mode (breakdown voltage

below ~12 V). The design is based on an earlier single-junction design that operated at a low reverse-bias voltage (below ~12 V) [7]-[8]. In order to detect the color and intensity within 10 nm spectral resolution in the 400-700 nm wavelength range, we develop a maximum likelihood (ML) estimation algorithm while taking into account photocurrent noise fluctuations. This algorithmic color sensor is expected to provide wavelength selectivity through integration with the aid of post-processing, which may enable spectral resolutions higher than those available in the raw sensor data.

Moreover, easy-to-use and closed-form exact analytical formulas for the excess noise factor are derived for mixed carrier injection and distributed-carrier injection APDs [9]. The simple formulas reported in this dissertation provide a valuable tool for optimizing the design of APD structures that exhibit even small levels of photon absorption in their multiplication regions. The newly-derived formulas reveal that in contrast to the case of edge electron injection, even with a small level of hole ionization (e.g., small k ~0.0001), the excess noise behavior exhibits a dramatic increase when mixed injection is allowed. It is also shown that the distributed-injection excess noise factor increases relative to the predictions offered by the classical McIntyre's theory, which assumes edge injection, depending on the absorption profile as it ranges from narrow to flat within the multiplication region. Comparisons show that McIntyre's predictions of the excess noise factor either underestimate or overestimate the distributed-injection F, depending on the photon absorption profile and the value of k.

1.2 Fundamental Research

The key challenge is to design and fabricate dual APD using standard CMOS technology with the following properties: (1) Low breakdown voltage ~10V; (2) Avalanche gain of

50 or higher; (3) High responsivity and high quantum efficiency; (4) Wavelength selectivity and light intensity detectivity; (5) Low noise with high speed operation; and (6) Availability of simple analytical formulas to predict mean-gain, excess-noise factor and avalanche breakdown voltage in the case when photons are absorbed in the multiplication region. The key barriers here are to maintain a low operating voltage (below 10V) at high gains (50) while maintaining low dark currents. Our approach for maintaining a low operating voltage is based on the careful design of a multi-junction SAM APD, where the multiplication (depletion) region is thin (~200 nm) and restricted to the depletion region. Another key strategy that we use to lower the voltage is increasing the doping level which causes a further reduction in the multiplication region, and hence a reduction in the breakdown voltage. The technique for enhanced quantum efficiency and responsivity is based on the strong dependence of silicon absorption depth on the incident light wavelength. Longer wavelength light penetrates silicon deeper than the light with shorter wavelength. In order for the wavelength selectivity with accuracy, a spectral sensing algorithm is developed using maximum likelihood estimator while taking into account photocurrent noise fluctuations in the algorithm.

1.3 Outline of Dissertation

Chapter 2 describes details of modeling and numerical results including the calculations of breakdown voltage, mean gain and excess noise factor of CMOS-compatible *p-n* junction Si APDs using recursive dead space multiplication theory (DSMT). The APD device was fabricated at Manufacturing Training and Technology Center (MTTC) cleanroom at the University of New Mexico. Measured dark current, breakdown voltage, spectral response and measured capacitance are also reported. Chapter 3 investigates N-

well/P-sub APD as well as the P+/N-well/P-sub APD device structures fabricated using IBM 0.13-μm CMOS technology. Specifically, we report here the measured dark-currents, capacitances, as well as the calculated and measured spectral responsivity, avalanche breakdown voltage, mean-gain, and excess-noise factor for both of the devices. More importantly, we report wavelength dependent mean-gain and excess-noise factor calculation using non-local DSMT analytical model. In Chapter 4, we derive easy-to-use exact analytical formulas for the mixed carrier injection and distributed carrier injection APDs. The analytical results are in excellent agreement with those calculated using the exact, numerically implemented DSMT method [10]. The results are also in good agreement with experiments [9].

Finally, design and modeling of algorithmic multi-color spectrsal sensor, i.e., dual-junction CMOS compatible avalanche photodiodes are outlined in chapter 5. The findings from *p-n* Si APD (Chapter 2) as well as N-well/P-sub and the P+/N-well/P-sub APDs (Chapter 3) and exact analytical formula for mixed injection APDs (Chapter 4) are used to guide the design of the dual junction CMOS APD.

References

[1] https://lesa.rpi.edu/

[2] M. M. Hossain, "Linear mode CMOS compatible pn junction avalanche photodiode for smart-lighting applications," MS Thesis, The University of New Mexico, USA, Aug. 2015. http://digitalrepository.unm.edu/ose_etds/8/

[3] M. M. Hossain and M. M. Hayat, "High responsivity double-junction CMOS-compatible avalanche photodiode," *Proc. 29th IEEE Photonics Conference*, Waikoloa, Hawaii, USA, pp. 262-263, Oct. 2-6, 2016.

[4] https://www.digikey.com/product-detail/en/ams/AS73210/AS73210DKR-ND/7793929

[5] G. N. Lu, M. B. Chouikha, G. Sou, and M. Sedjil, "Colour detection using a buried double p-n junction structure implemented in the CMOS process," *Electron. Lett.*, vol. 32, pp. 594-596, Mar. 1996.

[6] G. N. Lu, G. Sou, F. Devigny, and G. Guilland, "Design and testing of a CMOS BDJ detector for integrated microanalysis systems," *Microelectron. J.*, vol. 32, no. 3, pp. 227-234, Mar. 2001.

[7] M. M. Hossain, P. Zarkesh-Ha, J. P. R. David, and M. M. Hayat, "Low breakdown voltage CMOS compatible p-n junction avalanche photodiode," *Proc. 27th IEEE Photonics Conference*, La Jolla, San Diego, CA, USA, pp. 170-171, Oct. 12-16, 2014.

[8] M. M. Hossain, S. Ray, J. S. Cheong, L. Qiao, A. N. A. P. Baharuddin, M. M. Hella, J. P. R. David, and M. M. Hayat, "Low-noise speed-optimized large area CMOS avalanche photodetector for visible light communication," *IEEE/OSA J. Lightwave Technol.*, vol. 35, no. 11, pp. 2315-2324, June 2017.

[9] M. M. Hossain, J. P. R. David, and M. M. Hayat, "Exact analytical formula for the excess noise factor for mixed carrier injection avalanche photodiodes," *IEEE Trans. Electron Devices*, submitted, 2018.

[10] M. M. Hayat, B. E. A. Saleh, and M. C. Teich, "Effect of dead space on gain and noise of double-carrier-multiplication avalanche photodiodes," *IEEE Trans. Electron Devices*, vol. 39, no. 3, pp. 546-552, Mar. 1992.

Chapter 2

Low-Voltage p-n Junction CMOS Avalanche Photodiodes for Smart-Lighting Applications

2.1 Abstract

This chapter reports linear-mode p-n junction silicon avalanche photodiodes (APD) fabricated using 1 μm standard CMOS process. Measured mean gain of ~50 is obtained at a sufficiently low operating voltage of 8.7 V. Measured dark current and breakdown voltages are also reported supporting low-voltage operation. In addition, calculated breakdown voltage, mean-gain and excess-noise factor are predicted using the non-local dead space multiplication theory.

2.2 Introduction

There is a need in emerging smart-lighting concepts for an inexpensive and high-speed spectral sensing capability to enable adaptive lighting (smart spaces) and visible light communication. One approach to address this need is to design and manufacture novel CMOS-compatible, cost-effective detector arrays and readout circuits (ROICs) that incorporate waveguide technology on an avalanche photodiode (APD). This chapter focuses on the APD design and fabrication component of the sensing capability required by smart-lighting systems.

As an avalanche material, silicon has drawn attention to the detector community due do its low excess-noise (almost single-carrier multiplication) properties [1]-[2]. It has also been reported that the presence of the dead-space effect in Si materials causes further

reduction in the excess noise factor. More importantly, for 400 nm - 700 nm range of operation, ease of manufacture, mature fabrication technology in conjunction with the aforementioned avalanche properties together make Si APDs the ideal choice for future smart-lighting applications in the visible regime [3-5]. In particular, Si CMOS APDs are expected to provide high-speed and high-sensitivity sensors in terms of simplicity of design, low power consumption and cost-effectiveness for smart-lighting applications. To date, most of the CMOS-based APD devices have been dedicated to the Geiger mode, which aims to count individual photons under ultralow light conditions. However, there are few works reported on linear-mode APDs fabricated in standard CMOS process. One of the challenges in recently reported linear-mode CMOS APDs is that they need to be operated at voltages that are much higher than desired (e.g., 25, 35, 70 V versus 9 V or less) [6-8]. Here, we have reported the calculated mean gain and excess noise factor, using recursive dead-space multiplication theory (DSMT), as well as dark-current measurements to predict avalanche breakdown voltage of CMOS APD devices that we designed and fabricated [4-5]. In additon, we present experimental verification of the calculated mean gain as well as measured dark current, photocurrent and spectral response results supporting low-voltage operation. This type of APD can be integrated with waveguide structures to provide enhanced sensitivity and high-speed detection capability as well as uniformity across colors [9].

2.3 Device Structure

CMOS-compatible *p*-*n* junction Si APD was fabricated on a 1-0-0 oriented *p* type Si wafer (dopant boron) using a diffusion process. The structure consists of a boron-doped (3.5×10^{17} cm^{-3}) *p*+ Si layer, a phosphorus-doped (9.5×10^{18} cm^{-3}) *n*+ Si layer, and a 60

nm thick SiO_2 layer. The active dimensions of the devices are 100 μm × 100 μm, 150 μm × 150 μm, 200 μm × 200 μm and 250 μm × 250 μm, respectively. The junction depth of the APD device is 0.6 μm. The electron within the depletion region ($0 \leq x \leq W$) travels in the negative x direction. The photogenerated electron initiated avalanche multiplication process in the depletion region at $x = W$ is taken into account for the accurate prediction of breakdown characteristics in the recursive DSMT model [10, 11].

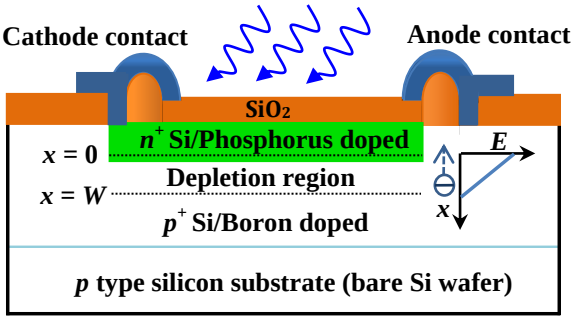

Figure 2.1: Schematic device structure of a CMOS compatible APD [4].

2.4 Calculation Method

The recursive DSMT analytical model was used to predict the dependence of the mean gain on the reverse bias voltage, the excess-noise characteristics and the breakdown voltage of the APD. The width of the multiplication region, W, was estimated by calculating the width of the depletion region, as described in more detail below.

The electric-field dependent ionization coefficients for electrons, α, and for that of holes, β, were calculated using the following equations [12]:

$$\alpha(E) = A_e exp\left[-\left(\frac{B_e}{E}\right)^{m_e}\right] \quad 5(a)$$

$$\beta(E) = A_h exp\left[-\left(\frac{B_h}{E}\right)^{m_h}\right] \quad 5(b)$$

where E is the electric field and the A, B, and m are material-dependent parameters listed

in [Table 2.1].

The dead space effect along with the non-uniform electric field and depletion layer width

Table 2.1: Ionization parameters for Si [3]-[5]

	A [cm^{-1}]	B [V/cm]	M	E_{th} [eV]
Electron	1.286×10^6	1.40×10^6	1.0	1.2
Hole	1.438×10^6	2.02×10^6	1.0	1.5

Table 2.2: Calculated parameters for n^+p CMOS Si APD [4]

APD	N_n (cm^{-3})	N_p (cm^{-3})	Reverse bias voltage (V)	Depletion width (nm)	Electric field (kV/cm)
1	9.5×10^{18}	1.0×10^{17}	0.2 - 14.9	122 – 455	188.5 - 703.1
2	9.5×10^{18}	1.5×10^{17}	0.3 - 12.4	104 – 342	241.1 - 792.7
3	9.5×10^{18}	2.0×10^{17}	0.3 - 11.0	91 – 281	281.2 - 868.4
4	9.5×10^{18}	2.5×10^{17}	0.2 - 10.0	79 – 243	305.2 - 938.7
5	9.5×10^{18}	3.0×10^{17}	0.2 - 10.0	72 – 221	333.8 – 1024
6	9.5×10^{18}	3.5×10^{17}	0.2 - 9.00	67 – 196	362.4 – 1060
7	9.5×10^{18}	4.0×10^{17}	0.2 - 8.63	63 – 180	389.4 – 1112
8	9.5×10^{18}	4.5×10^{17}	0.3 - 8.40	62 – 168	431.1 – 1168
9	9.5×10^{18}	5.0×10^{17}	0.3 - 8.00	59 – 157	455.8 – 1213
10	9.5×10^{18}	5.5×10^{17}	0.2 - 7.70	54 – 147	459.9 – 1249
11	9.5×10^{18}	6.0×10^{17}	0.2 - 7.70	52 – 141	482.1 – 1307
12, p^+n [13]	7.5×10^{16}	7.5×10^{18}	0.2 - 17.71	120 - 570	162.2 - 660.3

were used in the DSMT recursive analytical model to predict the breakdown voltage, mean gain and excess noise factors for the avalanche photodiode.

The non-local ionization coefficients and threshold energies for Si are reproduced for convenience in Table I from [3]-[5]. The electric field and the depletion width considered in the DSMT model are calculated (Table II) by solving Poisson's equation and standard formula mentioned above [10].

2.5 Numerical Results

The calculated position-dependent electric field, parameterized by the depletion region width W (for each applied reverse bias), is shown in Fig. 2.2 (a). The decreasing electric field profile with x indicates a carrier generated deeper in the depletion layer must travel a longer distance before becoming capable of ionizing. Figure 2.1(b) shows the ionization-coefficient profile. The higher electron ionization coefficient (α) than that of the hole (β) results in photoelectron initiated avalanche multiplication process in the depletion region exhibiting low excess noise factors. The value of k (β/α), the key performance parameter of APD, should be as low as possible to minimize the excess noise factor. The field profile within the depletion region, in conjunction with the ionization parameters, shown in Table I, were used in the DSMT analytical model to predict breakdown voltage, mean gain, and the excess noise factor.

Figure 2.3 depicts variation of calculated mean gains with the applied reverse bias voltages for different base doping concentrations N_p and N_n = 9.5 × 10^{18} cm^{-3}. The calculated breakdown voltages vary from 7 to 15 V for the base doping concentration variations from 1 × 10^{17} to 6 × 10^{17} cm^{-3}. Tunneling will dominate the breakdown characteristics for the doping concentrations beyond 6 × 10^{17} cm^{-3}. This is due to the

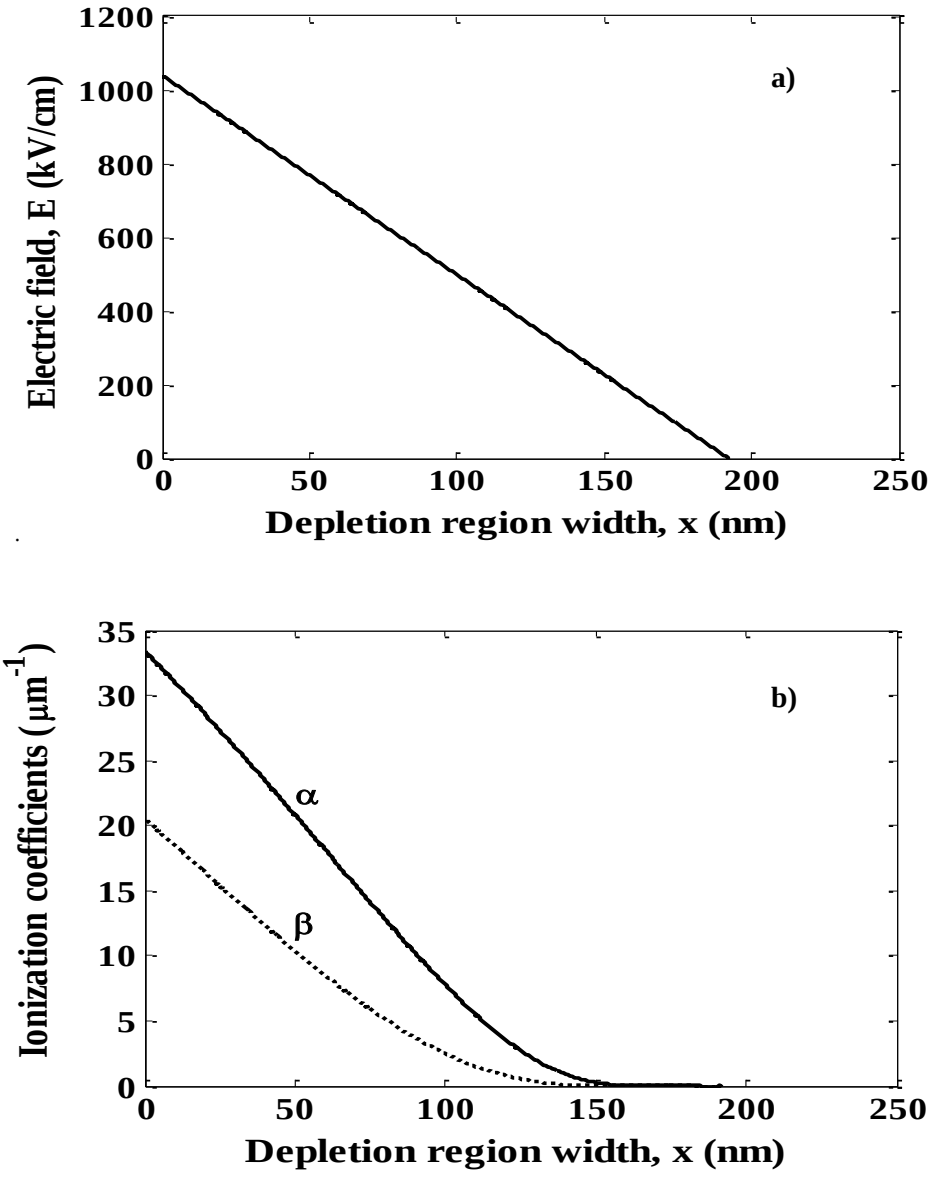

Figure 2.2: (a) Calculated electric-field profile as a function of x in the depletion region of width W = 192.2 nm for Si. V_R = 8.67 V, $N_a = 3.5 \times 10^{17}$ cm^{-3} and $N_d = 9.5 \times 10^{18}$ cm^{-3}. (b) Calculated electron and hole ionization coefficients, α and β, for Si as a function of x in the depletion region of W = 192.2 nm [5].

large electric field by which carriers can tunnel through a sufficiently thin potential barrier [14]. The predicted breakdown voltage using ionization coefficients (Table II) in the DSMT analytical model is in quite good agreement with the predicted and experimentally verified breakdown characteristics using a simple Monte-Carlo (SMC) model in silicon APD [13].

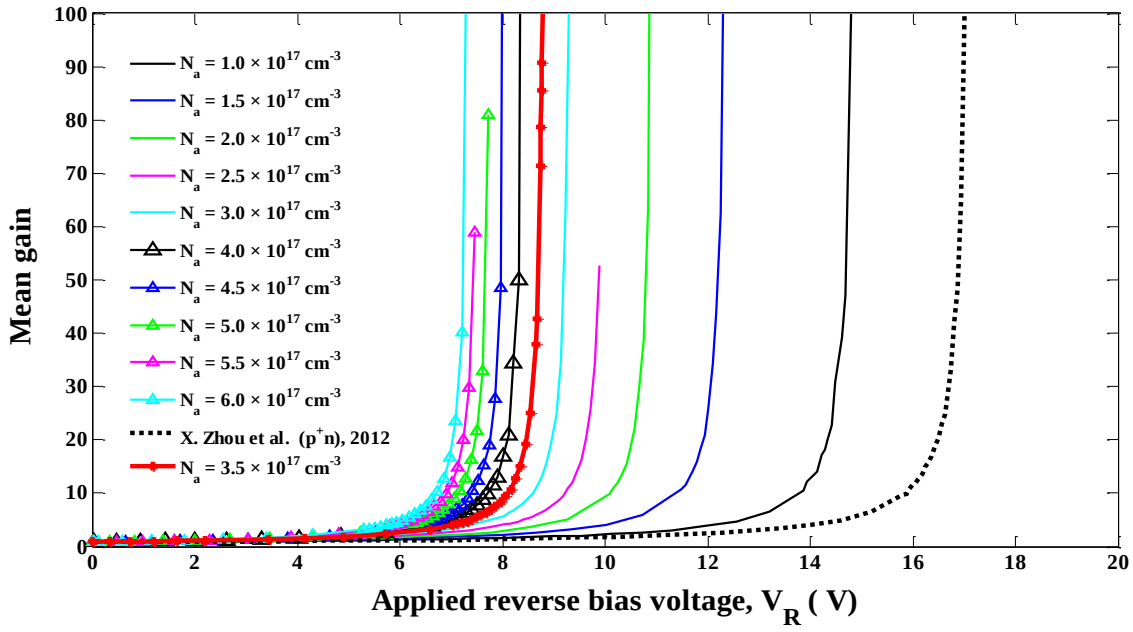

Figure 2.3: Calculated mean gain as a function of the applied reverse bias voltage with different base doping concentrations (N_p). Here, $N_n = 9.5 \times 10^{18}$ cm^{-3} [4].

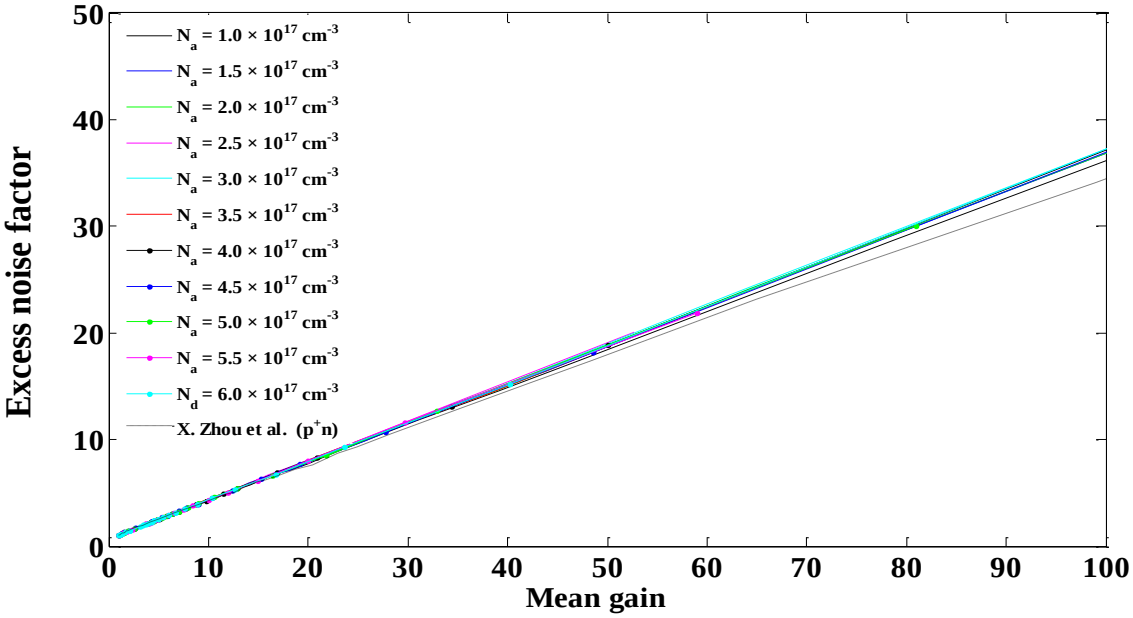

Figure 2.4: Calculated excess noise factor as a function of mean gain with different base doping concentrations (N_p). Here, $N_n = 9.5 \times 10^{18}$ cm^{-3} [4].

The calculated excess noise factor as a function of mean gain with different base doping concentrations is shown in Fig. 2.4. The Si non-local ionization coefficients and threshold

energies (Table 2.2) are taken into account in the DSMT model exhibiting low excess noise factors. This low excess noise factor is due to the presence of dead space effect in the thin depletion regions (See Table I) and the initiation of avalanche process by the photogenerated electron in the depletion region of Si APD. Figure 2.4 also shows that excess noise factor does not change much with substrate doping concentrations.

2.6 Device Fabrication

The *p-n* junction Si APD was fabricated using 1 μm standard CMOS processing technology at MTTC cleanroom at the University of New Mexico.

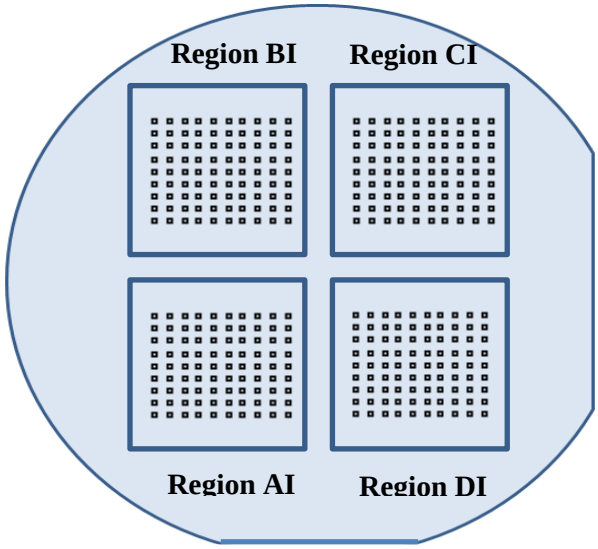

Figure 2.5: 1-0-0 orientated *P* type Si wafer (dopant boron).

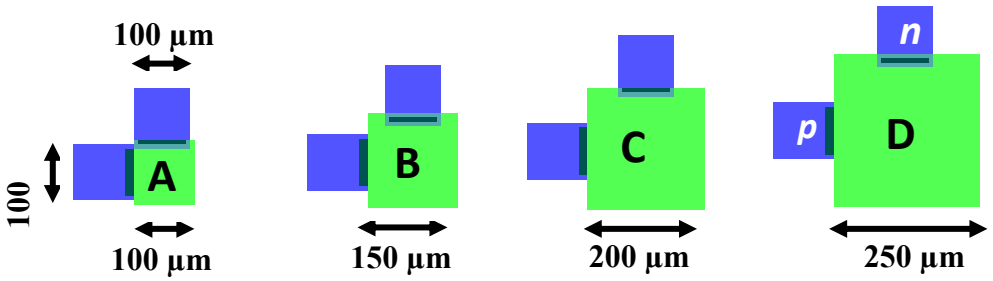

Figure 2.6: Active dimensions of CMOS APDs

A 1-0-0 orientated *p*- type four inch boron doped Si wafer was used to initiate the fabrication. The *p*+ (3.5×10^{17} $cm^{-3)}$ and *n*+ (9.5×10^{18} cm^{-3}) layers were created depositing phosphorus and boron, respectively on the Si wafer using diffusion process at the MTTC facility. Diffusion is defined as the movement of impurity atoms in a semiconductor material at high temperatures where the driving force of diffusion is the concentration gradient. In the APD fabrication process, four masks were used for the n+ diffusion, contact, SiO_2 deposition and metal patterning. The active dimensions of the APD devices were 100 μm × 100 μm, 150 μm × 150 μm, 200 μm × 200 μm and 250 μm × 250 μm, respectively. The schematic of CMOS APD wafer is shown in Fig. 2.5 with four different regions. Each region has active devices with dimensions 100 μm × 100 μm, 150 μm × 150 μm, 200 μm × 200 μm and 250 μm× 250 μm, respectively as shown in Fig. 2.6.

2.7 Current-Voltage Characteristics and Quantum Efficiency

This section describes experimental results of the fabricated planar *p*-*n* junction CMOS compatible APD including dark- and photo-current measurement, mean gain, capacitance and spectral response measurements.

Measured dark-current and photo-current characteristics for the fabricated CMOS APDs are shown in Fig. 2.8. Current-voltage characteristics were recorded with a 236 Keithley SourceMeter®, a source measure unit instrument. Photo-current measurements were performed using a 635 nm laser light source with optical power density of ~3.33 mW/cm^2. A PM100D (Thorlabs) optical power and energy meter was used to measure the output optical power of laser. The 200 μm × 200 μm active area device exhibit avalanche breakdown voltage at ~8.67 V. This confirms the prediction of avalanche

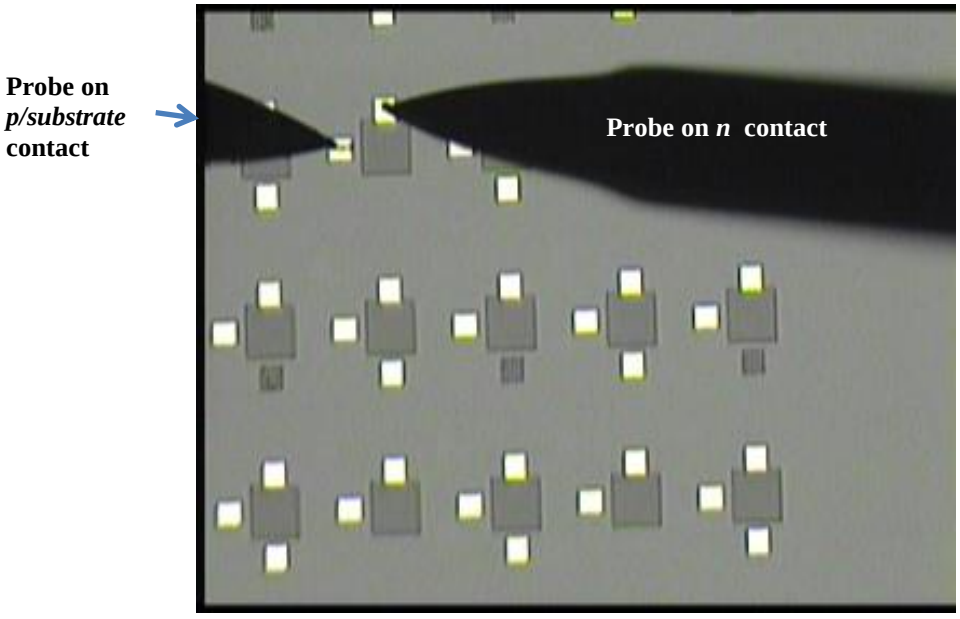

Figure 2.7: Fabricated CMOS APDs and probing for measurements.

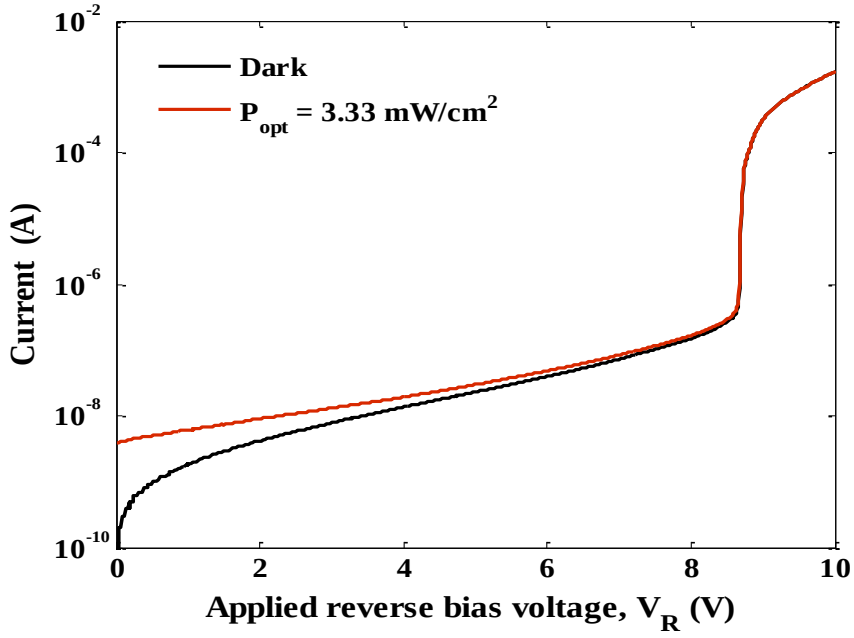

Figure 2.8: Experimental dark- and photo-current characteristics of 200 μm × 200 μm CMOS APD. Measurements were performed shining 635 nm laser output onto APD device with optical power density of ~3.33 mW/cm^2 [17].

breakdown with accuracy as evidenced by the simulations shown in Fig. 2.3 (N_a = 3.5 × 10^{17} cm^{-3}). A dark current of ~ 0.1 μA near avalanche breakdown is also shown in Fig.

2.8. This dark current is high due to the nonuniformities in the electric field (i.e., undesirable high fields) in the planar *p-n* junction APD device. The dark current can be minimized using a guard-ring, which will also serve to prevent premature breakdown at the APD periphery [15], [16].Photocurrent increases with the increasing of reverse bias voltage until it reaches the maximum value at avalanche for the 3.33 mW/cm^2 output optical power shining onto the APD surface area. At high laser power output, APD goes into saturation which is not desirable for APD operation. Saturation is a condition in which there is no further increase in detector response as the input light is increased. On the other hand, APD shows good response which is linear with low incident intensity up to the avalanche breakdown region of the device at ~8.74 V.

The quantum efficiency of the APD can be calculated using the standard formula as given by

$$QE = \frac{S \times 1240}{\lambda} \times 100[\%] \quad (12)$$

where, S is the photosensitivity (A/W) and λ is the wavelength of incident optical light. The cut-off wavelength for Si (E_g = 1.12 eV) is 1100 nm at room temperature. The unmultiplied photosensitivity and quantum efficiency (QE) were measured to be 2.928 mA/W and 0.57% respectively, at the applied unity-gain reverse bias voltage of 0.2 V and at 635 nm given wavelength of light. The calculated quantum efficiency for 200 μm × 200 μm CMOS APD was found to be 0.5%. This depicts that the measured QE is quite good agreement with the calculated QE.

2.8 Mean Main

The mean gain depends on applied reverse bias voltage as well as the incident optical power onto the active area of the APD. The gain was calculated from the measured dark-

and photo-currents using the standard formula [18],

$$M = \frac{I_{ph}(V) - I_{dark}(V)}{I_{ph}(V_{M=1}) - I_{dark}(V_{M=1})} \tag{13}$$

where I_{ph} and I_{dark} are the photocurrent and dark current respectively, V is the actual reverse bias voltage and $V_{M=1}$ is the unity gain reference voltage.

The unity-gain condition is normally identified as a plateau of photocurrent immediately after punch through where the collection of primary photo-carriers is at maximum but before the impact ionization process turned on in the APD device [19]. In our gain calculation from dark and photo-currents, $V_{M=1}$ = 0.2 V was used and the results are shown in Fig. 2.9. The APD achieves a gain of 50 at a reverse bias voltage of 8.67 V showing excellent agreement with simulation result as calculated from the nonlocal impact ionization model based on recursive DSMT.

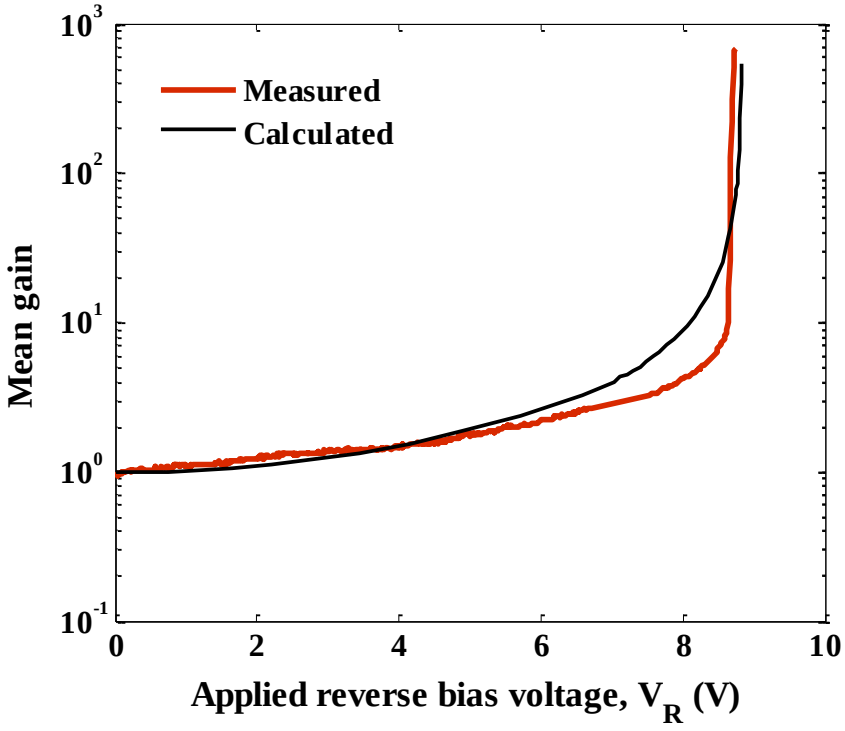

Figure 2.9: Mean gain as a function of applied reverse bias voltage. Measurement was performed shining 635 nm laser output onto APD device with optical power density of ~3.33 mW/cm^2 [17].

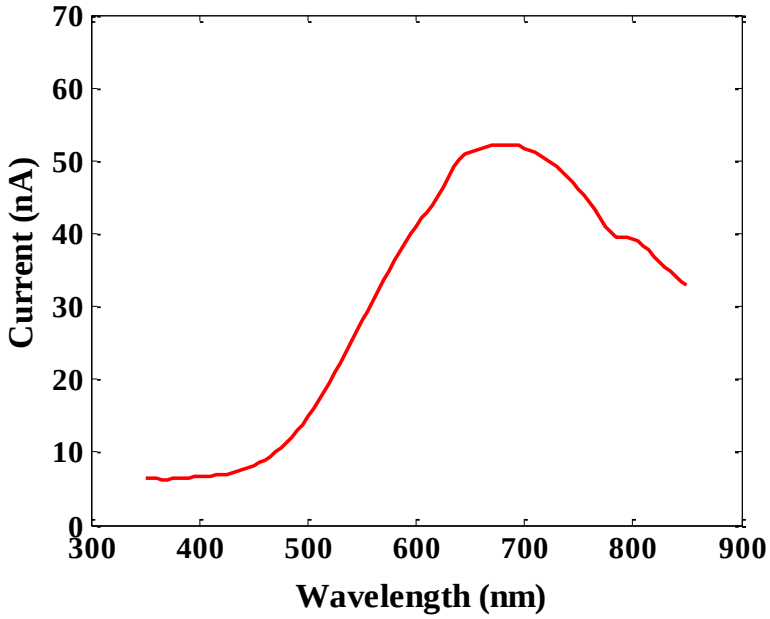

Figure 2.10: Measured spectral response of CMOS APD for the applied reverse bias voltage of -5.0 V [17].

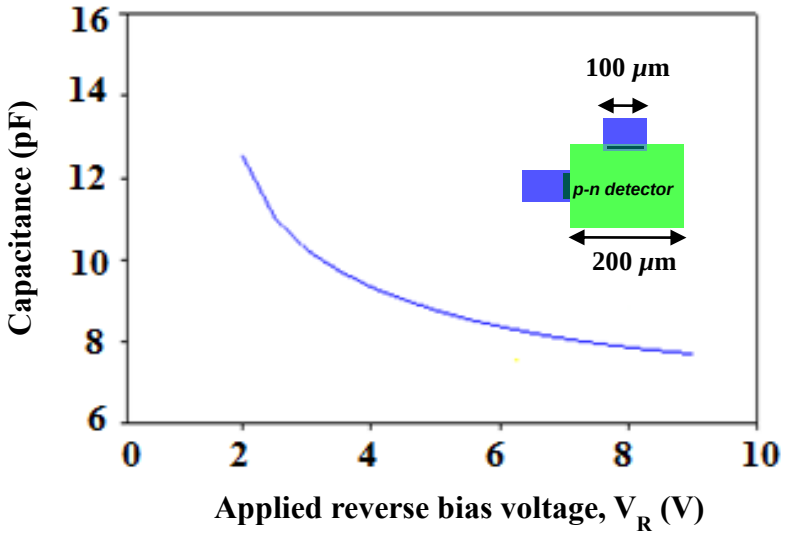

Figure 2.11: Capacitance-voltage measurements for the 200 μm × 200 μm CMOS APD.

2.9 Spectral Response

The spectral response measurement of CMOS APD for the applied reverse bias voltage of -5.0 V is shown in Fig. 2.10. Spectral measurements were performed using an HORIBA MicroHR 140 mm spectrometer with a 250 W tungsten-halogen light source (LSH-T250) and solid-state detector interface (1427C). The spectrometer has spectral

resolution of 0.3 nm with standard combination of 600 grooves/mm and 500 nm blaze grating. The peak is found to be at ~650 nm indicating that the APD can the applicable to visible light communication. The Si APD can detect light sufficiently in the visible region since it has large absorption coefficient in this region.

2.10 Capacitance

Measured capacitance as a function of applied reverse bias voltage is shown in Fig. 2.11 for the 200 μm × 200 μm planar *p-n* CMOS APD. The depletion region width increases with increasing applied reverse which in turn reduces APD capacitance. The decreasing value of capacitance near breakdown represents high speed operation of APD device. The higher *n*+ doping concentration leads to thinner depletion width and higher capacitance. The measured capacitance is found to be ~7.9 pF near around reverse bias breakdown of 8.67 V.

2.11 Integration of CMOS APD with Waveguide Structure

The *p-n* junction silicon APD was integrated with waveguide structure to create a silicon-

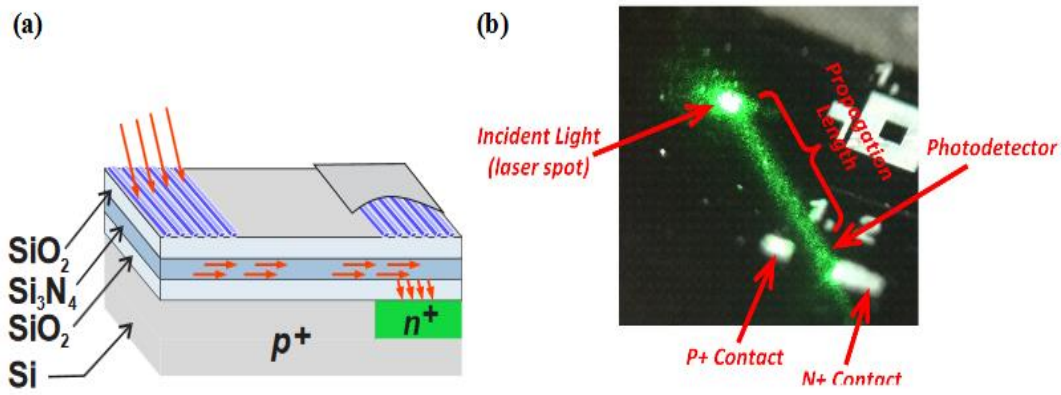

Figure 2.12: (a) Plenoptic detector with angle-of-incidence and wavelength integration; (b) Demonstration of waveguide coupling and propagation for a green laser source. Figure 2.12 is reproduced from [19].

integrated-circuit-compatible visible, plenoptic (angle and wavelength) detector required by smart-lighting applications [19]. The plenoptic detector reorted an angular resolution of less than 1° and a wavelength resolution of less than 5 nm.

2.12 Conclusion

Modeling, design and fabrication of CMOS-compatible *p-n* junction thin Si APDs were presented. The avalanche breakdown, mean gain and excess noise factor were calculated with substrate doping concentration variations using the recursive DSMT analytical model. The dark- and photo-current measurements, photosensitivity, quantum efficiency, mean gain, spectral response, and capacitance measurement results were reported for the 200 μm × 200 μm CMOS APD. The reported device benefits from design simplicity, potential for high-volume manufacturability, low power consumption and cost. The linear mode CMOS Si APD device is a promising device for high-speed sensing capability required for smart-lighting potential applications, including adaptive lighting (smart spaces) and visible-light communication systems.

References

[1] X. Zhou, J. S. Ng, and C. H. Tan, "A simple Monte Carlo model for prediction of avalanche multiplication process in Silicon," *J. Instrum.*, vol. 7, no. 8, p. P08006, Aug. 2012.

[2] C. H. Tan, "Measurements of excess avalanche noise in sub-micron Si and Al0.6Ga0.4As avalanche photodiodes," Ph.D. dissertation, Dept. of Electronic & Electrical Engg., U of Sheffield, 2001.

[3] S. Ray, M. M. Hella, M. M. Hossain**,** P. Zarkesh-Ha, and M. M. Hayat, "Speed optimized large area avalanche photodetector in standard CMOS technology for visible light communication," *Proc. 13th IEEE Sensors*, Valencia, Spain, pp. 2147-2150, Nov. 3-5, 2014.

[4] M. M. Hossain, P. Zarkesh-Ha, J. P. R. David, and M. M. Hayat, "Low voltage CMOS compatible p-n junction avalanche photodiode," *Proc. 27th IEEE Photonics Conference*, CA, pp. 170-171, Oct. 12-16, 2014.

[5] M. M. Hossain, J. Ghasemi, P. Zarkesh-Ha, and M. M. Hayat, "Design, modeling and fabrication of a CMOS compatible p-n junction avalanche photodiode," *Proc. 26th IEEE Photonics Conference*, Bellevue, WA, USA, pp. 584-585, Sept. 08-12, 2013.

[6] B. Steindl, R. Enne, S. Schidl, and H. Zimmermann, "Linear mode avalanche photodiode with high responsivity integrated in high-voltage CMOS," *IEEE Electron Device Lett*, vol. 35, no. 9, pp. 897–899, Sep. 2014.

[7] B. Steindl, W. Gaberl, R. Enne, S. Schidl, K. Schneider-Hornstein, and H. Zimmermann, "Linear mode avalanche photodiode with 1-GHz bandwidth fabricated in 0.35-µm CMOS," *IEEE Electron Device Lett*, vol. 26, no. 15, pp. 1511–1514, Aug. 2014.

[8] F. Villa, D. Bronzi, Y. Zou, C. Scarcella, G. Boso, S. Tisa, A. Tosi, F. Zappa, D. Durini, S. Weyers, U. Paschen, and W. Brockherde, "CMOS SPADs with up to 500 µm diameter and 55 detection efficiency at 420 nm", *J. Modern Opt.*, vol. 61, no. 2, pp.102 -115, 2014.

[9] A. Neumann, J. Ghasemi, S. Nezhadbadeh, X. Nie, P. Zarkesh-Ha, and S. R. J. Brueck, "CMOS-compatible plenoptic detector for LED lighting applications," *Opt. Express*, vol. 23, no. 18, pp. 23208-23216, Aug. 2015.

[10] M. M. Hayat, W. L. Sargeant, and B. E. A. Saleh, "Effect of dead space on gain and noise in Si and GaAs avalanche photodiodes," IEEE J. Quantum Electron., vol. 28, no. 5, pp. 1360-1365, May 1992.

[11] M. M. Hayat, B. E. A. Saleh, and M. C. Teich, "Effect of dead space on gain and noise of double-carrier multiplication avalanche photodiodes," IEEE Trans. Electron Devices, vol. 39, no. 3, pp. 546-552, March 1992.

[12] M. A. Saleh, M. M. Hayat, B. E. A. Saleh, and M. C. Teich, "Dead-space-based theory correctly predicts excess noise factor for thin GaAs and AlGaAs avalanche photodiodes," *IEEE Trans. Electron Devices*, vol. 47, no. 3, pp. 625-633, Mar. 2000.

[13] X. Zhou, J. S. Ng, and C. H. Tan, "A simple Monte Carlo model for prediction of avalanche multiplication process in Silicon," *J. Instrum.*, vol. 7, no. 8, p. P08006, Aug. 2012.

[14] S. M. Sze and and K. K. Ng, *Physics of semiconductor devices*, 3rd Ed., John Wiley & Sons, Inc., 2007.

[15] H.-S. Kang, M.-J. Lee, and W.-Y. Choi, "Si avalanche photodetectors fabricated in standard complementary metal–oxide-semiconductor process," *Appl. Phys. Lett.*, vol. 90, no. 15, pp. 151118.1-151118.3, Apr. 2007.

[16] M.-J. Lee and W.-Y. Choi, “Area-dependent photodetection frequency response characterization of silicon avalanche photodetectors fabricated with standard CMOS technology,” *IEEE Trans. Electron Devices*, vol. 60, no. 3, pp. 998–1004, Mar. 2013.

[17] M. M. Hossain**,** P. Zarkesh-Ha, and M. M. Hayat, "Linear mode CMOS compatible p-n junction avalanche photodiode with operating voltage below 9V," *Proc. 28th IEEE Photonics Conference (formerly IEEE LEOS)*, Reston, Virginia, USA, pp. 436-437, Oct. 4-8, 2015.

[18] B. Steindl, R. Enne, S. Schidl, and H. Zimmermann, “Linear mode avalanche photodiode with high responsivity integrated in high-voltage CMOS,” *IEEE Electron Device Lett*, vol. 35, no. 9, pp. 897–899, Sep. 2014.

[19] A. S. Huntington, M. A. Compton, and G. M. Williams, “Linear-mode single-photon APD detectors,” *Proceedings of SPIE*, vol. 6771, 67710Q (2007).

Chapter 3

Low-Noise Speed-Optimized Large Area CMOS Avalanche Photodetector for Visible Light Communication

3.1 Abstract

Mean-gain and excess-noise measurements are presented for a 350 × 350 μm^2 P+/N-well/P-sub and a 270 × 270 μm^2 N-well/P-sub avalanche photodetectors fabricated using 0.13-μm CMOS technology. The active area of the P+/N-well/P-sub device was divided into multiple subsections to decrease transit time and increase speed. For the P+/N-well structure, remarkably low excess-noise factors of 4.1 and 4 were measured at a mean gain of 16 corresponding to a k value of ~0.1, using a 542 (633) nm laser. For a variant N-well/P-sub structure, excess-noise factors of 6.5 and 6.2 were measured at a mean-gain of 16 corresponding to a *k* value of ~0.3. The proposed CMOS APDs with high gain, low noise, low avalanche breakdown voltage (below ~12 V) and low dark-currents (~nA) would be attractive for low-cost optical receivers in visible-light communication systems.

3.2 Introduction

Silicon photonics is a promising technology for the realization of low-cost, low-noise, high-speed and high-sensitivity photodetectors in visible-light communication (VLC) systems. The VLC system is gaining momentum as a solution to provide gigabit-class (up to 3 Gbps) connectivity of electronic devices in home and office environments [1-3]. Silicon avalanche photodiodes (APDs), with their inherent internal amplification mechanism and the resulting high-sensitivity, can offer an excellent photodetector choice

for high path-loss VLC systems [3]. In addition, Si APDs with their low-noise characteristics can provide improved signal-to-noise ratio (SNR) in the VLC receiver. Specifically, Si is a very attractive material for APDs due to its low k value (< 0.1), which results in a low excess-noise factor, F [4]-[18]. Additionally, careful device design and fabrication process can further improve the noise properties of Si APDs by reducing the thickness of the avalanche region [19]-[22].

More specifically, since VLC systems are an integral part of emerging smart-lighting concepts, there is a need for cost-effective and compact optical devices that enable VLC in such scenarios. The rapid advances in solid-state lighting and high-speed (~5 GHz for 30 meters of distance) plastic optical fiber (POF) technology have been paving the way toward a low-cost and high-speed implementation of VLC optical transmitters [1]. Si APDs implemented on standard complementary-metal–oxide–semiconductor (CMOS) process can offer a low-cost, compact, and high-yield fabrication solution to VLC receivers for smart-lighting systems [23-26]. Additionally, a large-area CMOS APD can substantially ease the coupling of light from the wide-diameter step-index POF (typically with a core diameter of 1 mm), which normally requires bulky concentrators and optical alignment setups [2].

Although linear-mode speed-optimized CMOS APDs have been developed in the recent years, one of the main challenges in them is that they require high operating voltages (e.g., 35.25, 68.25, 83.5, 119.25 V) [2, 27]. While high-voltage (HV) CMOS process can also be utilized to implement integrated receivers including HV-APDs, the technology choice for high-speed receiver implementation is moving toward smaller gate length with low-voltage (LV) CMOS nodes that offer optimized performance to analog/digital

circuitry. A possible solution to retain the advantages of both technologies is to fabricate the APD in high-voltage process while the receiver circuits in LV-CMOS nodes. However, interfacing such high-voltage systems with low-voltage optical receiver circuitry increases implementation complexity.

Therefore, it is beneficial to fabricate APDs in similar CMOS technology, as the receiver itself, to reduce implementation complexity of the entire system. Modern sub-micron CMOS processes employ increasingly higher doping concentration to achieve constant field scaling and thinner oxide layers in smaller device features for better performance. As a result, the highest voltage that can be applied without running into reliability issues in such technology also scales down. Since the allowed voltage levels in such CMOS-technology are low (e.g., ~11 V in 0.13-μm CMOS), special biasing circuitry must be utilized to operate such aforementioned high voltage APDs. In addition, low breakdown voltage APD benefits from low power operation and simple electrical bias circuitry. Therefore, it would be desirable to have a low-bias CMOS APD in a range compatible with the voltages allowed by CMOS circuitry. In this regard, a low operating-voltage (<11 V) P+/N-well APD was designed and fabricated using a 0.35-μm CMOS process [10]. However, the design yielded a high k value of 0.47, which resulted in a high excess-noise factor (e.g., F = 5.2 at 480/560/650 nm, and F = 3.9 at 380 nm at M 16). The APD also suffered from high dark currents (~1 μA at the breakdown voltage of 10.8 V).

Recently, we have reported a speed-optimized, large-area P+/N-well/P-sub APD fabricated in 0.13-μm CMOS technology for the VLC applications [3]. This device was based on an earlier design, reported in [3], which helped overcome the speed limitation associated with a large active area [26]. The total area (350 × 350 μm^2) of the device

reported in [3] was sub-sectioned into 20 × 20 μm^2 identical P+ regions inside an N-well. The outputs of the subsections were connected in parallel in order to achieve large bandwidth (6 GHz). The detection speed was increased as a result of the reduced transit time of diffusive carriers in the large-area CMOS APD. Measured dark-current, photo-current, simulated frequency response as well as the calculated mean-gain and excess-noise factor were reported for the P+/N-well/P-sub APD device [3].

In this work, we further investigate N-well/P-sub APD as well as the P+/N-well/P-sub APD device structures of the type reported in [3]. Specifically, we report here the measured dark-currents, capacitances, as well as the calculated and measured spectral responsivity, avalanche breakdown voltage, mean-gain, and excess-noise factor for both of the devices. The reported APDs exhibit low dark currents (in the range of nA) for a linear-mode avalanche breakdown voltage below 11 V. The investigated P+/N-well APD devices offer very low excess noise factors (4.1 and 4.0 using a 542 laser and a 633 nm laser, respectively, both at a mean gain of 16) with a low *k* value of 0.1. The reported excess-noise measurements are the lowest as compared to those for other reported CMOS APDs in the visible regime of the electromagnetic spectrum [7], [9]-[10], [12], [14]-[16].

3.3 Device Structure

The P+/N-well/P-sub and N-well/P-sub APD device structures considered here have been fabricated using IBM 0.13-μm standard CMOS technology. Figure 1(a) shows the die micrograph of the photodiode and the zoomed-in layout view is shown in Fig. 3.1(b). Figure 3.1(c) shows the large-area P+/N-well/P-sub APD. Note that this structure features sub-sectioned regions of P+ diffusion interlaid in a meshed configuration [3]. The advantage of such structure is the reduced diffusion distances of minority carriers that

results in a smaller transit time and higher optical bandwidth [3], [26].

Due to the large number of substrate and cathode contacts interlaced in such meshed structure, the substrate resistance for the photo-carriers also decreases. However, as described in [3], the overall junction capacitance of the sub-divided structure remains almost the same as its conventional counterpart due to the equivalency of total active area. The P+/N-well/P-sub structure consists of a p-substrate (5×10^{15} cm^{-3}) layer, a 1.5-μm thick N-well (5×10^{17} cm^{-3}) layer, a 0.3-μm thick P+ (5×10^{19} cm^{-3}) layer and a 0.3-μm thick N+ (5×10^{19} cm^{-3}) layer. It is also assumed that the impurity concentrations follow a Gaussian profile at the edges of the specified regions, both in horizontal and vertical directions. The total area of the device is 350×350 μm^2, which is sub-sectioned into 20×20 μm^2 identical P+ regions inside an N-well. The active area is divided into a meshed array of P+ islands and the cathode electrode is inserted in-between for uniform distribution of bias voltage. A different type of N- well/P-sub APD structure is shown in Fig. 3.1(d), which is comprised of N-well stripes inside P-substrate in an area of ~270×270 μm^2. The purpose of the striped structure is to pass metal density rules in this sub-micron technology and to reduce contact resistance of both the N-well and P-sub contacts. However, the opaque metal contacts resulting from the plurality of the N-well stripes cause partial shading of light. The structure consists of a p-substrate (5×10^{15} cm^{-3}) layer, a 1.5-μm thick N-well (5×10^{17} cm^{-3}) layer, a 0.3-μm thick P+ (5×10^{19} cm^{-3}) layer and a 0.3-μm thick N+ (5×10^{19} cm^{-3}) layer. An N-well width of ~15 μm is chosen as a compromise between terminal resistance, parasitic capacitance and fill-factor. The shallow-trench-isolation (STI) is used around the P+ and N+ regions for both of the APD devices to prevent premature edge breakdown.

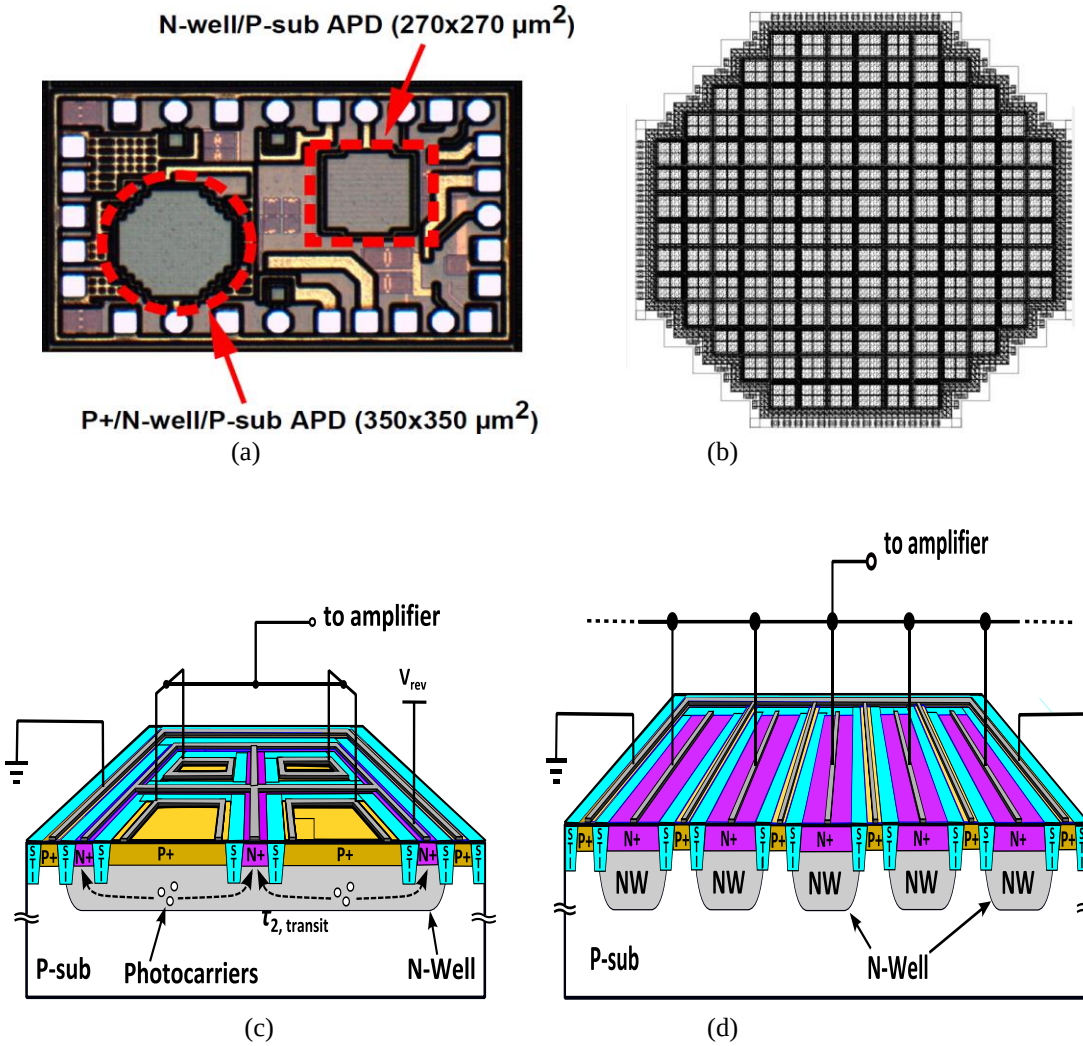

Figure 3.1: Investigated silicon APDs fabricated in 0.13-μm CMOS technology: (a) die micrograph, (b) layout view showing 20 × 20 μm^2 sub-sections, (c) P+/N-well/P-sub structure (350 × 350 μm^2) with reduced transit time and (d) N-well/P-sub structure (270 × 270 μm^2). (a)-(c) are reproduced from [3], [38].

3.4 Modeling and Simulation Results

The dead-space multiplication theory (DSMT) [4, 5] was used to calculate the avalanche breakdown voltage, mean-gain and excess-noise factor for the APD devices. In the DSMT analytical model, the depletion region of the APD is assumed to be extended from x = 0 to x = *W*, where *W* is the depletion-region width. It is further assumed that the avalanche multiplication process is initiated by the photogenerated electron at the high field, P+/N-well junction (*x* = 0) for the P+/N-well/P-sub device structure (Fig. 3.2(a)).

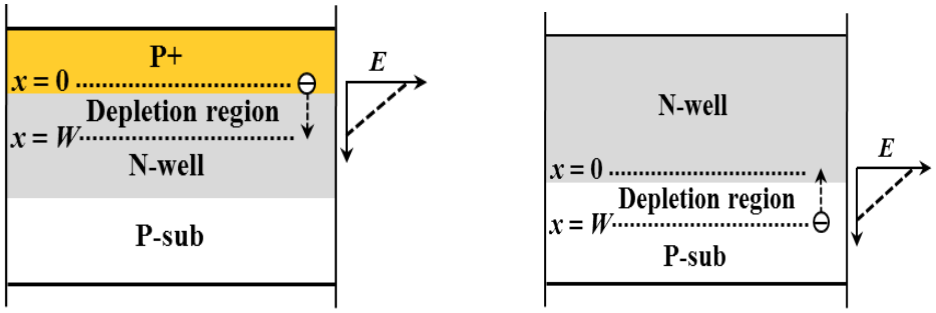

Figure 3.2: P+/N-well/P-sub APD structure showing direction of electron injection (a) and N-well/P-sub structure showing the direction of electron injection (b) [38].

Electrons travel in the positive x-direction within the depletion region. For the N-well/P-sub device structure, avalanche multiplication is initiated by the photogenerated electron at the low field, N-well/P-sub junction ($x = W$). Electrons travel in the negative x-direction within the depletion region.

In addition to the electron-initiated avalanche multiplication process, hole injection and mixed-carrier injection were taken into account in the recursive DSMT model while taking into account the absorption profile of each device. Consider an electron and a hole are located at position x within the multiplication region. Assume that $Z(x)$ is the random sum of electrons and holes produced by the electron including the initiating electron itself. Similarly, $Y(x)$ is the random number of all electrons and holes produced by the hole and its offsprings, including the hole itself. Note that $Z(W) = 1$ and $Y(0) = 1$. Consider, $z(x) = \langle Z(x) \rangle$ and $y(x) = \langle Y(x) \rangle$ are the means of $Z(x)$ and $Y(x)$, respectively. Similarly, $z_2(x) = \langle Z^2(x) \rangle$ and $y_2(x) = \langle Y^2(x) \rangle$ are the second moments of $Z(x)$ and $Y(x)$, respectively. Here, bracket denotes ensemble average. The electron and hole probability densities (h_e and h_h), the first moments ($z(x)$ and $y(x)$) and the second moments ($z_2(x)$ and $y_2(x)$) are calculated using the equations expressed in [5]. The gains for an electron-initiated avalanche G', a hole-initiated avalanche G'', and a mixed-carrier initiated

avalanche G''' are calculated from the quantities $z(x)$ and $y(x)$ as follows. In particular, the mean of G', G'' and G''' are

$$< G' > = \frac{1}{2}(1 + z(0)), \tag{1}$$

$$< G'' > = \frac{1}{2}(1 + y(w)) \tag{2}$$

and

$$< G''' > = C \int_0^w \frac{1}{2}[z(x) + y(x)]\, e^{-rx} dx. \tag{3}$$

And the total mixed-injection mean-gain is calculated using

$$< G > = \ p_e < G' > + p_h < G'' > + < G''' >, \tag{4}$$

where p_e and p_h are the probability of photon absorption above and below the depletion region, respectively, r is the absorption coefficient in Si, and C is a constant chosen so that $C \int_0^w e^{-rx}\, dx = p_m$ is the probability that an incident photon is absorbed in the depletion region.

Next, the second moment of the gain in the cases of an electron-initiated, a hole-initiated and a mixed-carrier initiated avalanches are given by

$$< G'^2 > = 0.25(1 + 2\, z(0) + z_2(0)), \tag{5}$$

$$< G''^2 > = 0.25(1 + 2\, y(w) + y_2(w)), \tag{6}$$

and

$$< G'''^2 > = C \int_0^w \frac{1}{4}[z_2(x) + 2\, z(x)y(x) + y_2(x)]\, e^{-rx} dx. \tag{7}$$

The second moment of the mixed-injection gain is therefore

$$< G^2 > = \ p_e < G'^2 > + p_h < G''^2 > + < G'''^2 >. \tag{8}$$

Finally, the mixed-injection excess-noise factor F is

$$F = \frac{<G^2>}{<G>^2}. \tag{9}$$

The electric field and depletion width were calculated using Technology Computer Aided Design (TCAD) Sentaurus™ software tool. Note that Sentaurus Device takes into account physics models like Poisson's equation and carrier continuity in calculating electric fields. The electric-field profiles in the multiplication region were extracted from TCAD simulation as shown in Fig. 3.3(a). The electric-field dependent ionization coefficients for electrons (α) and holes (β) are calculated using Chynoweth's formula [29]

$$\alpha(E) = A_e exp\left[-\left(\frac{B_e}{E}\right)^{m_e}\right] \tag{10a}$$

and

$$\beta(E) = A_h exp\left[-\left(\frac{B_h}{E}\right)^{m_h}\right], \tag{10b}$$

where E is the electric field and the A, B, and m are material- dependent parameters (listed in Table 3.1) chosen from experimental [28] and fitted [8] data.

The electric field within the depletion region, electron and hole dead spaces, d_e and d_h in conjunction with the ionization coefficients, α and β, as shown in Figs. 3.3(a), (b), and (c), were used in the DSMT analytical model to predict the avalanche breakdown voltage, mean-gain, and the excess-noise factor. The enabled ionization parameters $\alpha^*(\beta^*)$ are calculated from the experimentally determined values $\alpha(\beta)$ by equating the mean ionizing lengths from the DSMT and local model by using the formula [30]

$$\alpha = \frac{1}{\frac{1}{\alpha^*}+2d_e}, \tag{11}$$

where d_e (d_h) is the dead space for electron (hole). In addition, McIntyre's classical noise model formula [31], as shown below

$$F(M) = kM + \left(2 - \frac{1}{M}\right)(1-k), \tag{12}$$

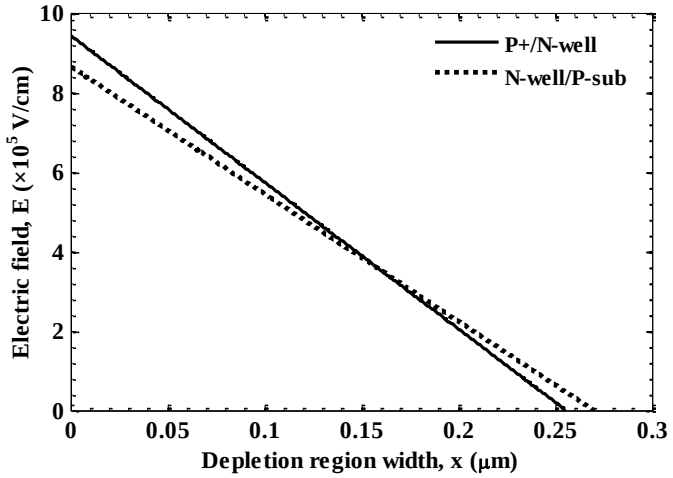

(a)

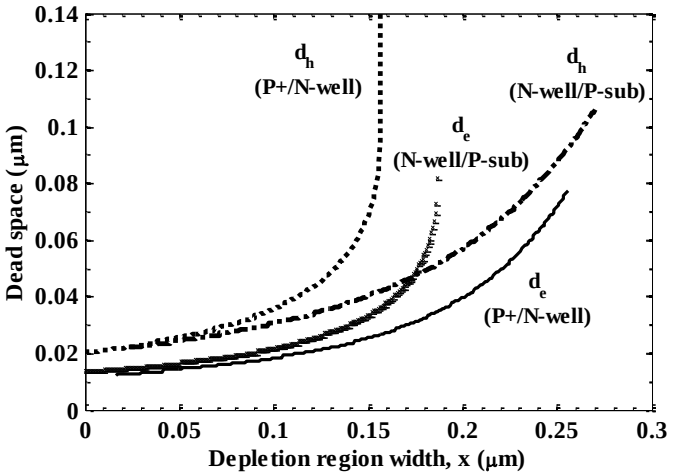

(b)

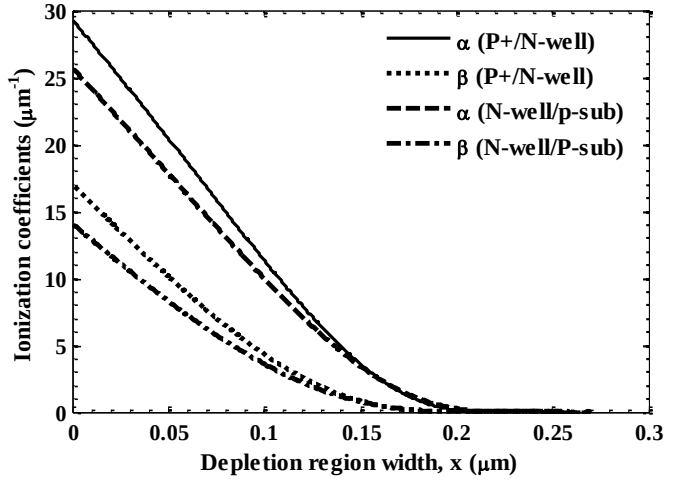

(c)

Figure 3.3: Calculated electric-field profile as a function of x in the depletion region (a), calculated dead spaces for electron (d_e) and hole (d_h) (b), and calculated electron and hole ionization coefficients, α and β (c) [38].

Table 3.1: Ionization parameters for Si [28]

	A [cm^{-1}]	B [V/cm]	M	E_{th} [eV] [8]
Electron	1.286×10^6	1.40×10^6	1.0	1.1
Hole	1.438×10^6	2.02×10^6	1.0	1.8

is used to evaluate the equivalent hole-to-electron ionization ratio, *k*. A small value of *k* represents a low excess-noise factor for an electron-initiated multiplication process.

The absorbed photon density as a function of device depth is shown in Fig. 3.4 for the front-side illuminated P+/N-well and N-well/P-sub APDs. Simulations were performed using TCAD software tool with 460 nm, 542 nm, and 633 nm excitations having a constant illumination of 1.46 mW/cm^2. The absorbed photon density is at its maximum value at the top of the APD and it decreases with the device depth. For the P+/N-well/P-sub APD, approximately 65%, 26% and 11% of the incident light are absorbed in the P+ region for 460 nm, 542 nm, 633 nm excitations, respectively. However, higher percentage of light absorption in P+ layer yields low values of excess noise factor (Fig. 3.10) for the dominant electron initiated multiplication process in the avalanche region. Note that approximately 21%, 17% and 8% of the light are absorbed in the multiplication region for 460 nm, 542 nm, and 633 nm wavelengths, respectively, giving rise to mixed-injection multiplication process. In addition, reduced excess-noise factor is observed in going from 460 nm to 633 nm excitations. This is due to the reduced amount of mixed-injections in the multiplication region for long wavelengths.

For a variant N-well/P-sub structure, approximately 0.5%, 22% and 57% of the light are absorbed in the P-sub region. This results in relatively higher excess noise factors due to the injection of holes in the multiplication region. Additionally, increased excess-noise

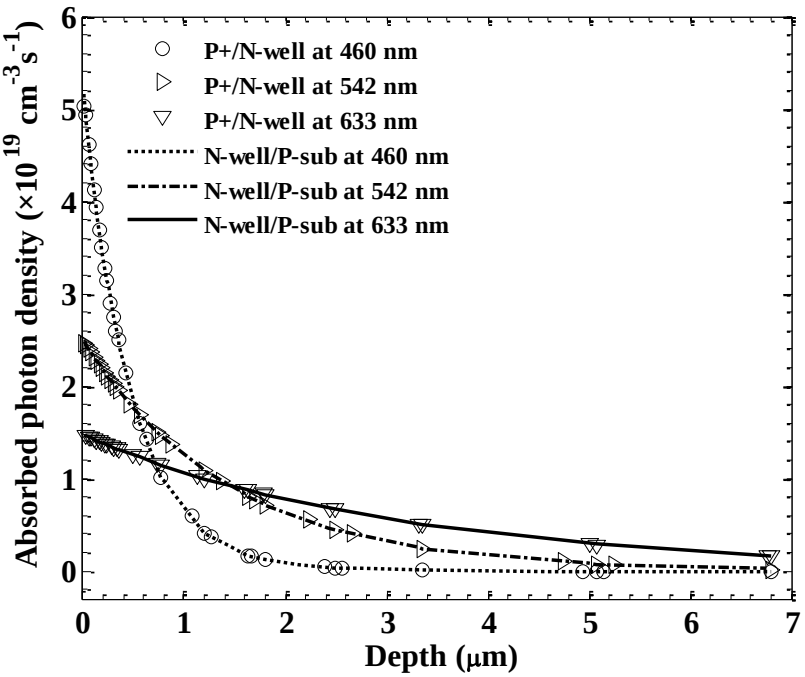

Figure 3.4: Simulated absorbed photon density as a function of device depth for the P+/N-well/P-sub and the N-well/P-sub APD devices. Simulations were performed using Sentaurus TCAD software tool [38].

factor is observed in going from 633 nm to 460 nm excitations (Fig. 3.10). This is due to the increased amount of hole injections in the multiplication region for short wavelengths. Note that approximately 0.3%, 5% and 6% of light are absorbed in the multiplication region for 460 nm, 542 nm, and 633 nm wavelengths, respectively, giving rise to mixed-injection multiplication process.

The wavelength dependent mean-gain and excess-noise factors (Figs. 3.9 and 3.10) are calculated using non-local DSMT analytical model taking into account 460 nm, 542 nm, and 633 nm excitations. Note that equations (4) and (8) represent first and second moments of the mixed-injection mean avalanche gain used in the DSMT model. These equations, in turn, require knowledge of the probability of photon absorption at each

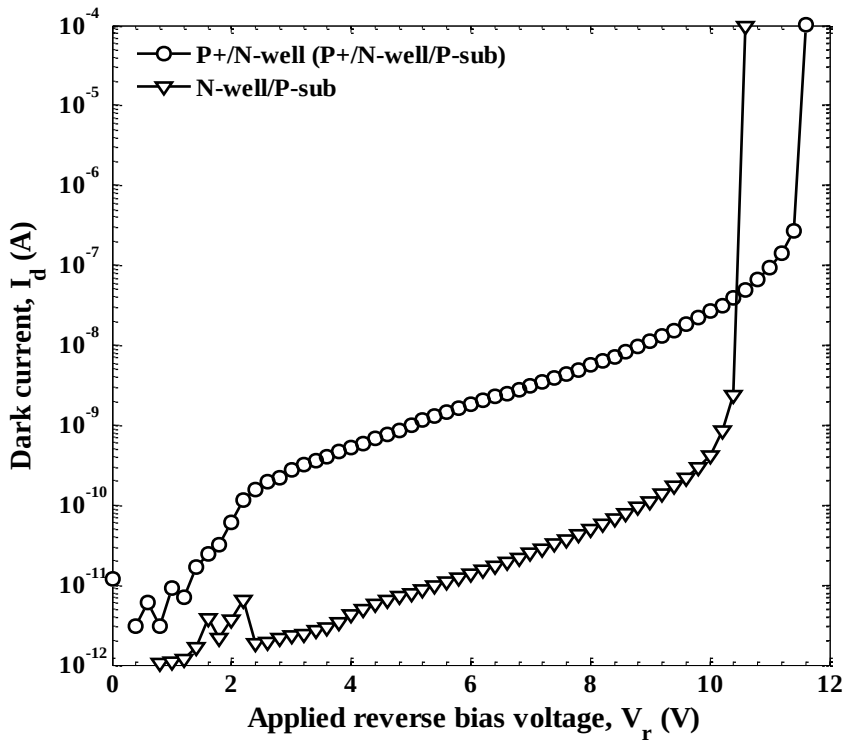

Figure 3.5: Measured dark current versus applied reverse bias voltage for the P+/N-well (P+/N-well/P-sub) and the N-well/P-sub APD devices [38].

location along the device depth. For example, see the exponential terms in equations (3) and (7), which are used in equations (4) and (8). Now the probability of photon absorption at each location is calculated from Fig. 4, as calculated by the Sentaurus TCAD software tool.

3.5 Measurement Results

Measured dark-current characteristics for the fabricated CMOS APDs are shown in Fig. 3.5. The current voltage characteristics were recorded with a Keithley 237 source- meter. In the linear avalanche regime, the P+/N-well (P+/N-well/p-sub) and the N-well/P-sub APD devices exhibit low dark currents of ~93 nA and ~0.86 nA at the breakdown voltages of ~11 V and ~10.5 V, respectively. However, the N-well/P-sub APD (270 × 270 μm^2) exhibits low dark currents as compared to the P+/N-well (350 × 350 μm^2)

APD. The large difference in dark currents may be due to the difference in peak electric field in each of the APD device structures. This may not be related to the area of the device where the dark current increases linearly with the device active area [34]. We believe that the high field required for the avalanche multiplication process gives rise to strong band-to-band-tunneling, resulting in a high dark current (~nA) for both of the APDs. The comparably low breakdown voltage of the N-well/P-sub APD is due to the proximity of P+ substrate contacts in between the plurality of N-well fingers. The shallow-trench-isolation guard-ring (STI GR) around the P+ and N+ regions prevents premature edge breakdown at the APD periphery. The dark currents are comparable to the reported values in [9, 16] and are low as compared to the high dark currents of 1 μA at 10.8 V as in [10], and 3 μA at 8.41 V as in [14]. The reported CMOS APDs in [16] exhibit low dark currents in the range of ~pA before avalanche breakdown occurs. The amplified dark current (due to the tunneling effect at the edges of p+ regions in n-well and n+ regions in p-well) was significantly reduced by using lightly doped p-sub or STI around the p+ and n+ regions.

Measured spectral-responsivity characteristics for the P+/N- well and N-well/P-sub APD devices are shown in Figs. 3.6a and 3.6b, respectively. Spectral measurements were performed using a single grating monochromator with a 100 W tungsten light source. A supervisory-control-and-data-acquisition (SCADA) system was also used in a desktop computer for automatic measurement. In order to modulate the optical signal, the monochromatic light from the exit slit of the monochromator was chopped at a frequency of 180 Hz. The optical beam was subsequently focused on the optical window of the device-under-test (DUT) by using a microscope objective. A Keithley 236 SMU was

used for bias voltage requirements across the device and the resultant photocurrent was measured using a SR830 lock-in amplifier (LIA).

Measured responsivity curves in Figs. 3.6(a) and 3.6(b) show peaks due to the optical interference in the dielectric stack atop the silicon surface. Note that IBM 0.13-μm CMOS technology considered here to fabricate P+/N-well/P-sub and N-well/P-sub APDs consists of 8 metal layers and 8 dielectric layers. There is also a final passivation layer on top of the last metal layer, which adds up to the total stack. As a result, there are multiple reflections and refractions as well as attenuation through the stack of materials. This, in turn, exhibits very irregular transmission characteristics [32]-[33] and spectral response [14] as a function of the wavelength. In addition, there is a ±20% process variation in thickness of dielectric layers. This process variation causes deviation in transmission coefficient through the dielectric stack [32]-[33], which has significant impact on the APD responsivity.

For the P+/N-well APD, the unity-gain responsivities are 0.014 A/W, 0.022 A/W and 0.024 A/W for 460 nm, 542 nm, and 633 nm excitations, respectively. For a variant N-well/P-sub APD, unity-gain responsivities are 0.007 A/W, 0.011 A/W, and 0.014 A/W. Both of the APDs exhibit very low values of responsivity which result from the aforementioned optical interferences in the dielectric stack and un-optimized CMOS process for APD devices. However, responsivity can be improved by using optimized CMOS process which can replace dielectric stack with an antireflection coating [14]. The spectral responsivity can also be improved with increased reverse bias voltage which results widening of the depletion region. In addition, avalanche multiplication occurs for higher bias voltage which in turn increases responsivity.

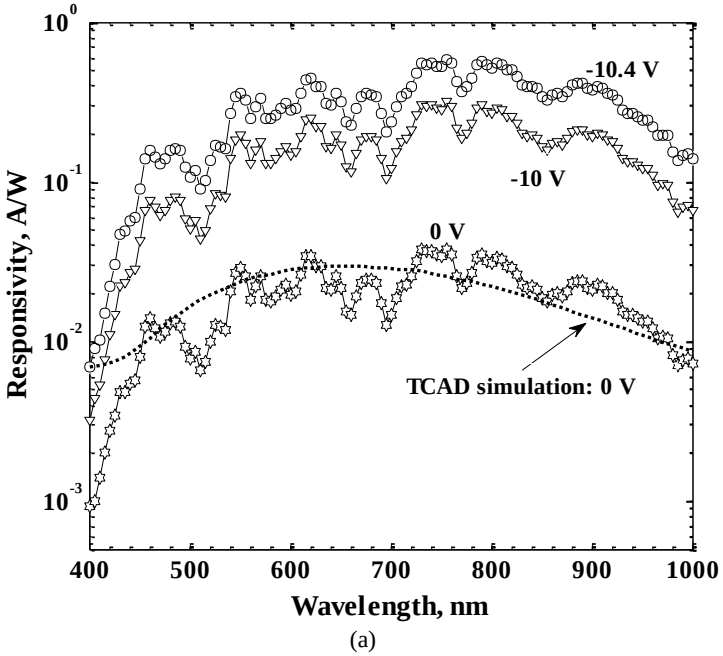

(a)

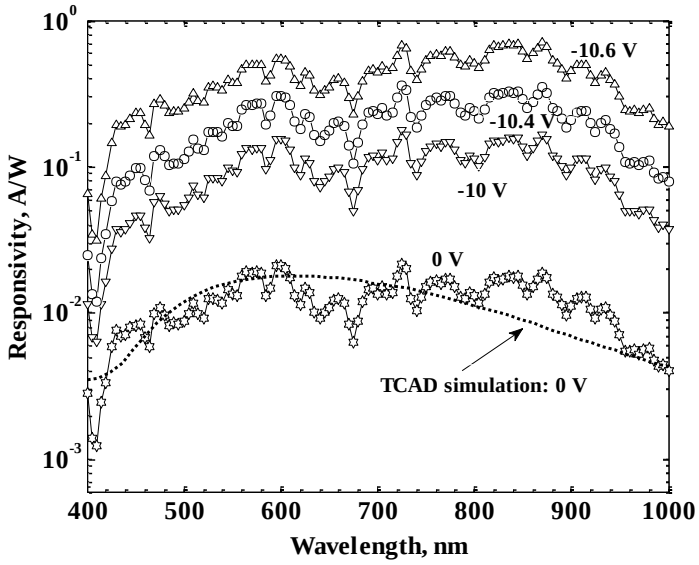

(b)

Figure 3.6: Measured spectral responsivity as a function of wavelength for the P+/N-well (a) and the N-well/P-sub (b) APD devices [38].

The zero-bias spectral responsivities were calculated using transmission matrix method (TMM) optical solvers in conjunction with the complex-refractive-index model embedded in Sentaurus TCAD. The calculated responsivity curves are slightly off from the measured responsivity for both of the APDs. This may be due to the presence of

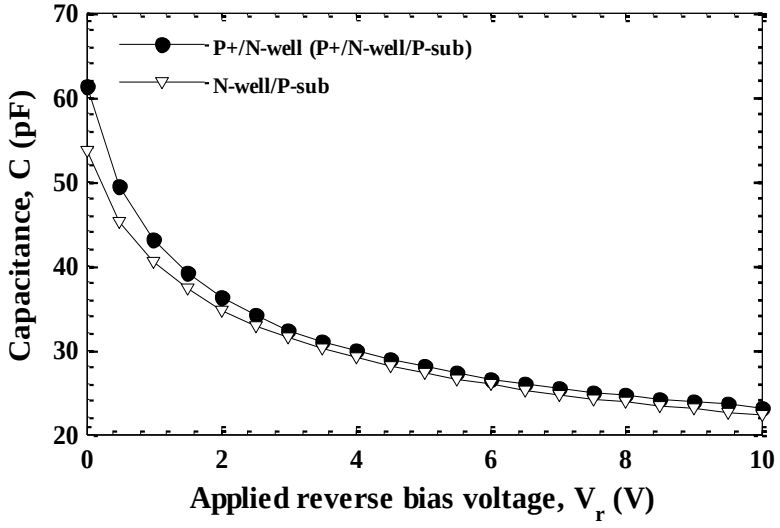

Figure 3.7: Measured capacitance versus applied reverse bias voltage for the P+/N-well (P+/N-well/P-sub) and the N-well/P-sub APD devices [38].

dielectric stack atop the Si surface.

Figure 3.7 shows the measured capacitance as a function of applied reverse bias voltage for the APD devices. The C-V measurements were carried out using an HP 4275A LCR meter, and the testing frequency was 1 MHz with an AC amplitude of 0.05 V. The measured capacitances for the P+/N-well (P+/N-well/P-sub) and the N-well/P-sub APD devices are below 25 pF under operating bias voltages. The transimpedance-amplifier (TIA) based measurement system, as reported in [35], can measure the excess-noise factor reliably on a wide variety of materials and APD devices, with a capacitance value up to ~50 pF. Therefore, the mean-gain and excess-noise measurements have been performed for both of the P+/N-well (P+/N-well/P-sub) and N-well/P-sub APDs.

The mean-gain and excess-noise measurement system is shown in a block diagram in Fig. 3.8. A Thorlabs 460 nm LED (LED470L), a Uniphase 542 nm He-Ne laser, and a Lambda Photometrics 633 nm He-Ne laser were used to illuminate the device with a mechanical chopper having chopping frequency at around 180 Hz. In addition, a TIA

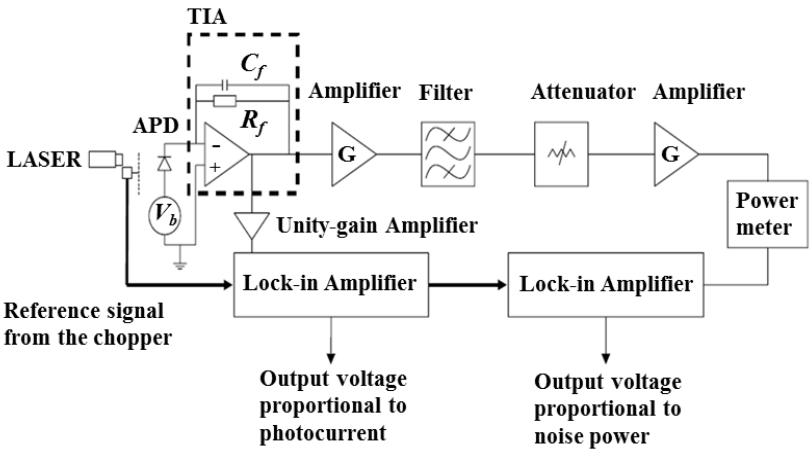

Figure 3.8: Block diagram of the mean-gain and excess-noise measurement system. The TIA consists of an op-amp with a feedback resistor R_f and capacitor C_f. This block diagram is reproduced from [35], [38].

(an AD9631 high speed operational amplifier with feedback capacitance and resistance) was used to convert photodiode current into a proportional voltage. This output voltage consists of a noisy, square waveform at the chopper frequency. The peak-to-peak value of a noise-free version of this waveform (difference between the photocurrent and dark current) is proportional to the mean photocurrent. The output voltage representing the photocurrent was buffered through a unity gain voltage follower to smooth the signal and was fed to a Stanford Research SR830 LIA. The LIA output voltage was converted to a value of stimulated photocurrent by using the known TIA gain of 1100 V/A. The mean-gain was calculated using the definition for multiplication given by

$$M = \frac{i_{ph}}{i_{pr}}, \tag{13}$$

where i_{ph} and i_{pr} are the measured output photocurrent and the unmultiplied primary photocurrent, respectively.

The output of the TIA, photocurrent and its multiplied noise, was amplified by a low-noise amplifier (Mini-Circuits ZFL-500LN+). In order to extract noise information from the TIA output, the photocurrent signal must be removed. This can be done by passing

the signal through a bandpass filter (Mini-Circuits SBP-10.7+). The photocurrent signal associated with the 180 Hz fundamental and its harmonics were attenuated by passing only the noise pass-band frequency, ranging from 9.5 to 11.5 MHz with a center frequency of 10.7 MHz. The output of the bandpass filter contains only the information of the noise signal (associated with the avalanche gain process which multiplies the photocurrent), which resembles an amplitude modulated noise waveform. The noise signal was then amplified by a low-noise cascaded amplifier (an HP355D attenuator with three Mini-circuits amplifiers: 500LN, 1000LN and AD9618) giving a total gain of around 78 dB. The attenuator was used in the cascade to cope with the wide range of noise amplitudes and to avoid the risk of saturating the output stages for large noise signals. The output noise voltage of the cascaded amplifier was fed into a power meter (a squaring-and-averaging circuit) to obtain the noise-power output. The noise-power was then measured using a second SR830 lock-in amplifier. The excess-noise factor is obtained using the expression [35], [36]

$$F(M) = \frac{N_{DUT}}{aMI} \times \frac{B_{eff}(C_{Si})}{B_{eff}(C_{DUT})}, \tag{14}$$

where N_{DUT} is the measured noise power of the device under test, a is a correction factor, I is the multiplied photocurrent, B_{eff} (C_{Si}) is the effective noise bandwidth at the calibrating Si photodiode's capacitance (C_{Si}) and B_{eff} (C_{DUT}) is the effective noise bandwidth at the device under test's capacitance. The excess-noise measurement system was calibrated against a commercial Si photodiode at unity gain. The effect of the shot noise measurement in the investigated P+/N-well/P-sub and N-well/P-sub CMOS APDs was assumed to be contributed from the multiplied excess-noise. In addition, calibration tests were performed with devices with known excess noise to ensure the absolute F

measured in CMOS APDs under test are within the acceptable range.

The mean-gain and excess-noise factor depend on the applied reverse bias voltage as well as the incident wavelength onto the active area of the APD. The electron-hole pair generation (from photon absorption) depends on the penetration depth: long wavelength light penetrates silicon deeper than the light with short wavelength. For low-noise operation, it is expected to have electron initiated avalanche multiplication process since electrons have higher ionization coefficients than holes.

The measured mean-gain, as a function of the applied reverse bias voltage, is shown in Fig. 3.9. In the linear avalanche regime, the P+/N-well APD exhibits a mean-gain of ~16, at a reverse bias voltage of 10.53 V, resulting from the use of a 460 nm LED, and 542 nm and 633 nm lasers, respectively. For the N-well/P-sub device structure, the linear-mode mean-gain of ~16 was measured at a reverse bias voltage of 10.4 V using 460 nm LED, and 542 and 633 nm lasers, respectively. The wavelength dependent mean-gains were calculated using non-local DSMT analytical model with 460 nm, 542 nm and 633 nm excitations. The measured breakdown voltages and mean- gain show excellent agreement with the calculated results using the DSMT, as evidenced by Figs. 3.5 and 3.9.

The measured excess-noise factor, as a function of the mean gain, is shown in Fig. 2.10 for 542 nm and 633 nm excitations, respectively. At a mean-gain near and below 2, however, the photocurrent was quite low (~1 μA). In addition to the inherently low excess-noise in the P+/N-well devices, the noise-power was too weak to be measured accurately, being below the noise of our measurement setup. This results in error when calculating the excess noise near unity. Our measurement error is around ± 5% in the excess-noise factor, *F*, values of unity. Nevertheless, the measurement error decreases

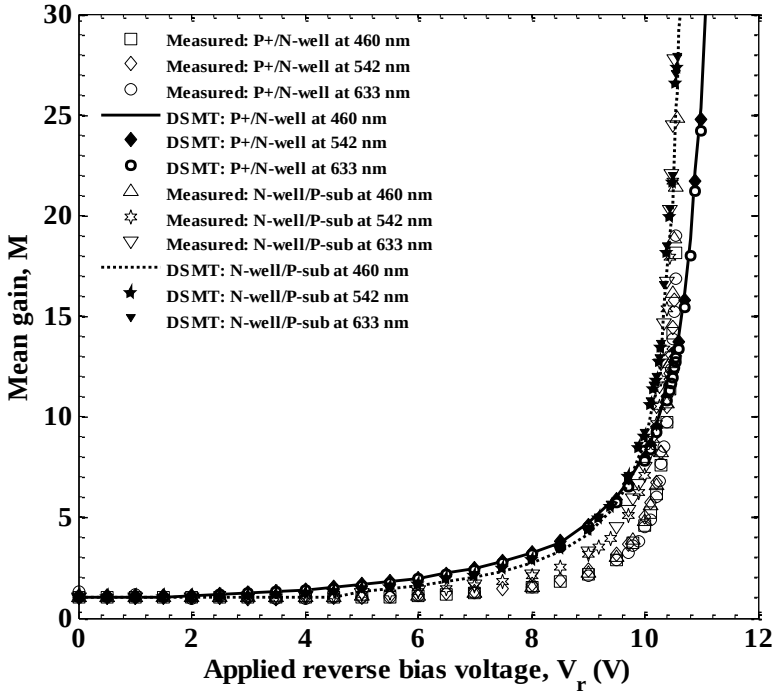

Figure 3.9: Measured mean-gain versus reverse bias voltage for the P+/N-well (P+/N-well/P-sub) and the N-well/P-sub APD devices, respectively, using a 460 nm LED, and 542 nm and 633 nm lasers. Wavelength dependent mean-gains are calculated using non-local DSMT analytical model [38].

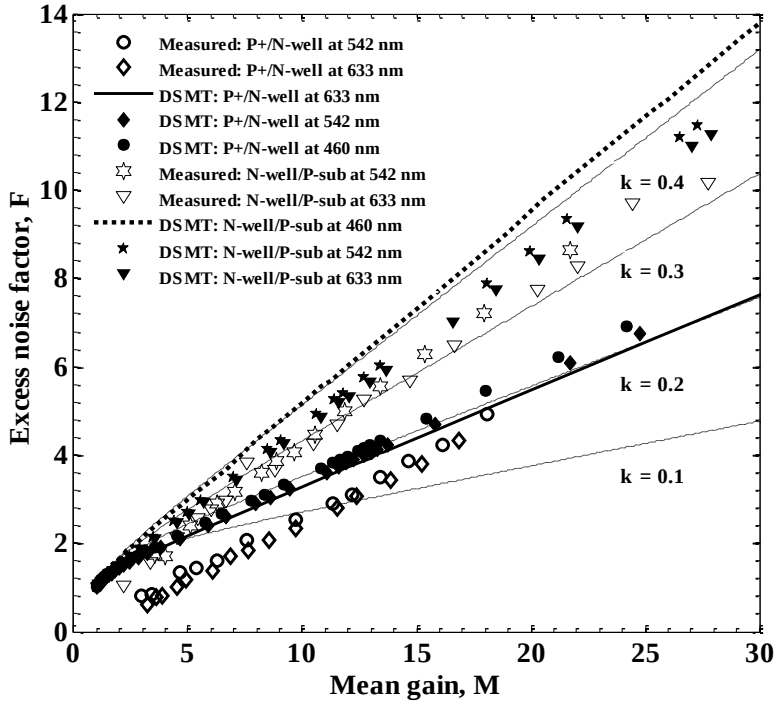

Figure 3.10: Measured excess-noise factor versus mean-gain for the P+/N-well (P+/N/well/P-sub) and the N-well/P-sub APD device, respectively, using 542 nm and 633 nm lasers. Wavelength dependent excess noise-factors are calculated using non-local DSMT analytical model. McIntyre's curves are denoted with *k* = 0.1, 0.2, 0.3, and 0.4 [38].

with higher multiplication values ($M > 2$). Note that we could not measure excess-noise factor at the 460 nm excitation due to the low amount of photocurrents.

The P+/N-well APD exhibits very low excess-noise factors of 4.1 and 4 at a mean gain of 16 using 542 nm and 633 nm lasers, respectively, as compared to the measured excess-noise factors in the visible regime of wavelength, as summarized in Table 2.2. The low excess noise factor is due to the presence of dead space in the thin depletion region and the initiation of avalanche multiplication process by the dominant photogenerated electron in the depletion region [4, 5]. The measured excess-noise factor falls close to the $k = 0.1$ curve, as calculated from McIntyre's noise model.

For the N-well/P-sub device structure, excess-noise factors of 6.5 and 6.2 were measured at a mean-gain of 16 using 542 and 633 nm lasers, respectively. The high excess noise appears as a result of the injection of holes in the multiplication region. The measured excess-noise factor falls close to the calculated DSMT curve as well as the McIntyre's noise curve at $k = 0.3$. The measured excess-noise with 542 nm was slightly higher than that with 633 nm for both of the P+/N-well and N-well/P- sub APD devices. The wavelength dependent excess-noise factors are also calculated using DSMT model with 460 nm, 542 nm and 633 nm excitations. The calculated excess-noise factors using recursive DSMT analytical model were slightly higher than measured values for both of the APDs. This could be due to the presence of non-uniform electric fields in the multiplication region.

3.6 Conclusion

Modeling and measurements for the speed-optimized, large- area CMOS compatible P+/N-well/P-sub and N-well/P-sub APDs were presented. Remarkably low excess-noise

TABLE 3.2
PERFORMANCE COMPARISON WITH DIFFERENT SILICON APDS

References	Technology node	Breakdown voltage, V_{br} (V)	Dark current I_d	Wavelength (nm)	Excess noise factor, F (M = 16)	Ionization ratio, $k = \beta/\alpha$
A. R. Pauchard *et al.*, 2000 [7]	custom	15	n.d.	600 380	6.2 3	0.47
A. Rochas *et al.*, 2002 [9]	0.8-μm CMOS	19.5	0.2 nA	400	5.8	n.d.
L. Pancheri *et al.*, 2008 [10]	0.35-μm CMOS	10.8	1 μA	380 480/560/650	3.9 5.2	0.47
G.-F. D. Betta *et al.*, 2011 [12]	0.35-μm CMOS 0.7-μm HVT CMOS	n.d. 20.8	n.d. n.d.	560 650	5.1 70	0.2
M. Atef *et al.*, 2013 [14]	40-nm CMOS	8.41	3 μA	520	12 (M = 27)	n.d.
L. Pancheri *et al.*, 2014 [15]	0.15-μm CMOS	23.1	n.d.	415 850	3.5 5	n.d.
M.-J. Lee *et al.*, 2014 [16]	0.25-μm CMOS	12.4	0.1 nA	850	13	0.47
This work	0.13-μm CMOS	11	93 nA	542 633	4.1 4	0.1

factor values were reported for the P+/N-well APD in the visible wavelength regime. The reported devices benefit from high-speed operation, low-voltage biasing and low cost. The large-area CMOS Si APDs with subsections are potential devices for the realization of low-noise, multi-gigabit visible-light communication systems.

References

[1] Y. Dong and K.W. Martin, "A high-speed fully-integrated POF receiver with large-area photo detectors in 65 nm CMOS," *IEEE J. Solid-State Circuits*, vol. 47, no. 9, pp. 2080-2091, 2012.

[2] B. Steindl, W. Gaberl, R. Enne, S. Schidl, K. Schneider-Hornstein, and H. Zimmermann, "Linear mode avalanche photodiode with 1-GHz bandwidth fabricated

in 0.35-μm CMOS," *IEEE Photon. Technol. Lett.*, vol. 26, no.15, pp. 1511-1514, Aug. 2014.

[3] S. Ray, M. M. Hella, M. M. Hossain, P. Zarkesh-Ha, and M. M. Hayat, "Speed optimized large area avalanche photodetector in standard CMOS technology for visible light communication," *Proc. 13th IEEE Sensors* Valencia, Spain, pp. 2147-2150, Nov. 3-5, 2014.

[4] M. M. Hayat, W. L. Sargeant, and B. E. A. Saleh, "Effect of dead space on gain and noise in Si and GaAs avalanche photodiodes," *IEEE J. Quantum Electron.*, vol. 28, no. 5, pp. 1360-1365, May, 1992.

[5] M. M. Hayat, B. E. A. Saleh, and M. C. Teich, "Effect of dead space on gain and noise of double-carrier-multiplication avalanche photodiodes," *IEEE Trans. Electron Devices*, vol. 39, no. 3, pp. 546–552, Mar. 1992.

[6] C. H. Tan, J. C. Clark, J. P. R. David, G. J. Rees, S. A. Plimmer, R. C. Tozer, D. C. Herbert, D. J. Robbins, W. Y. Leong, and J. Newey, " Avalanche noise measurement in thin Si p^+-i-n^+ diodes," *Appl. Phys. Lett.*, vol. 76, no. 26, pp. 3926-3928, June 2000.

[7] A. Pauchard, P. Besse, and R. Popovic, "Dead space effect on the wavelength dependence of gain and noise in avalanche photodiodes," *IEEE Trans. Electron Devices*, vol. 47, no. 9, pp. 1685–1693, Sep. 2000.

[8] C. H. Tan, J. P. R. David, G. J. Rees, R. C. Tozer, and D. C. Herbert, "Treatment of soft threshold in impact ionization," *J. Appl. Phys.*, vol. 90, pp. 2538–2543, Sep. 2001.

[9] A. Rochas, A. R. Pauchard, P. A. Besse, D. Pantic, Z. Prijic, and R. S. Popovic, "Low-noise silicon avalanche photodiodes fabricated in conventional CMOS technologies," *IEEE Trans. Electron Devices*, vol. 49, no. 3, pp. 387-394, Mar. 2002.

[10] L. Pancheri, M. Scandiuzzo, D. Stoppa, and G.-F. Dalla Betta, "Low noise avalanche photodiode in standard 0.35-μm CMOS technology," *IEEE Trans. Electron Devices*, vol. 55, no. 1, pp. 457–461, Jan. 2008.

[11] Y. Kang, H.-D. Liu, M. Morse, M. J. Paniccia, M. Zadka, S. Litski, G. Sarid, A. Pauchard, Y.-H. Kuo, H.-W. Chen, W. Sfar Zaoui, J. E. Bowers, A. Beling, D. C. McIntosh, X. Zheng, and J. C. Campbell, "Monolithic germanium/silicon avalanche photodiodes with 340 GHz gain-bandwidth product, " *Nature Photon.*, vol. 3, pp. 59-63, Jan. 2009.

[12] G.-F. D. Betta, L. Pancheri, D. Stoppa, R. Henderson and J. Richardson, "Avalanche photodiodes in submicron CMOS technologies for high-sensitivity imaging," in *Advances in Photodiodes*, pp. 226-248, 2011.

[13] X. Zhou, J. S. Ng, and C. H. Tan, "A simple Monte Carlo model for prediction of avalanche multiplication process in Silicon," *J. Instrum.*, vol.7, no. 8. p. P08006, Aug. 2012.

[14] M. Atef, A. Polzer, and H. Zimmermann, "Avalanche double photodiode in 40-nm standard CMOS technology," *IEEE J. Quantum Electron.*,vol. 49, no. 3, pp. 350–356, Mar. 2013.

[15] L. Pancheri, G.-F. Dalla Betta, and D. Stoppa, "Low-noise avalanche photodiode with graded junction in 0.15-μm CMOS technology," *IEEE Electron Device Lett.*, vol. 35, no. 5, pp. 566–568, May 2014.

[16] M.-J. Lee, H. Rücker, and W.-Y. Choi, "Optical-power dependence of gain, noise, and bandwidth characteristics for 850-nm CMOS silicon avalanche photodetectors," *IEEE J. Sel. Topics Quantum Electron.*, vol. 20, no. 6, Nov./Dec. 2014.

[17] J. S. Cheong, M. M. Hayat, X. Zhou, and J. P. R. David, "Relating the experimental ionization coefficients in semiconductors to the nonlocal ionization coefficients," *IEEE Trans. Electron Devices*, vol. 62, no. 6, pp. 1946-1952, June 2015.

[18] R. Enne, B. Steindl, and H. Zimmermann, "Speed optimized linear-mode high-voltage CMOS avalanche photodiodes with high responsivity," *Optics Letters*, vol. 40, no. 19, pp. 4400-4403, Oct. 2015.

[19] M. M. Hossain, J. Ghasemi, P. Zarkesh-Ha, and M. M. Hayat, "Design, Modeling and Fabrication of a CMOS Compatible p-n Junction Avalanche Photodiode," *Proc. 26th IEEE Photonics Conference*, Bellevue, WA, USA, pp. 584-585, Sept. 08-12, 2013.

[20] M. M. Hossain, P. Zarkesh-Ha, J. P. R. David, and M. M. Hayat, "Low breakdown voltage CMOS compatible p-n junction avalanche photodiode," *Proc. 27th IEEE Photonics Conference*, La Jolla, San Diego, CA, USA, pp. 170-171, Oct. 12-16, 2014.

[21] M. M. Hossain, P. Zarkesh-Ha, and M. M. Hayat, "Linear mode CMOS compatible p-n junction avalanche photodiode with operating voltage below 9V," *Proc. 28th IEEE Photonics Conference*, Reston, Virginia, USA, pp. 436-437, Oct. 4-8, 2015.

[22] M. M. Hossain and M. M. Hayat, "High responsivity double-junction CMOS-compatible avalanche photodiode," *Proc. 29th IEEE Photonics Conference*, Waikoloa, Hawaii, USA, pp. 262-263, Oct. 2-6, 2016.

[23] N. Izhaky, M. T. Morse, S. Koehl, O. Cohen, D. Rubin, A. Barkai, G. Sarid, R. Cohen, and M. J. Paniccia, "Development of CMOS-compatible integrated silicon photonics devices," *IEEE J. Sel. Topics Quantum Electron.*, vol. 12, no. 6, pp. 1688–1698, Nov./Dec. 2006.

[24] H.-S. Kang, M.-J. Lee, and W.-Y. Choi, "Si avalanche photodetectors fabricated in standard complementary metal–oxide-semiconductor process," *Appl. Phys. Lett.*, vol. 90, no. 15, pp. 151118 (1-3), Apr. 2007.

[25] N. Faramarzpour, M. J. Deen, S. Shirani, and Q. Fang, "Fully integrated single photon avalanche diode detector in standard CMOS 0.18-µm technology," *IEEE Trans. Electron Devices*, vol. 55, no. 3, pp. 760–767, Mar. 2008.

[26] M.-J. Lee and W.-Y. Choi, "Area-dependent photodetection frequency response characterization of silicon avalanche photodetectors fabricated with standard CMOS technology," *IEEE Trans. Electron Devices*, vol. 60, no. 3, pp. 998–1004, Mar. 2013.

[27] R. Enne, B. Steindl, and H. Zimmermann, "Speed optimized linear-mode high-voltage CMOS avalanche photodiodes with high responsivity," *Optics Letters*, vol. 40, no. 19, pp. 4400-4403, Oct. 2015.

[28] T. Rang, "The impact-ionization coefficients of carriers and their temperature dependence in silicon," *Radioelectron. Commun. Syst.*, vol. 28, no.5, pp. 83-85, 1985.

[29] M. A. Saleh, M. M. Hayat, B. E. A. Saleh, and M. C. Teich, "Dead-space-based theory correctly predicts excess noise factor for thin GaAs and AlGaAs avalanche photodiodes," *IEEE Trans. Electron Devices*, vol. 47, no. 3, pp. 625-633, Mar. 2000.

[30] J. S. Cheong, M. M. Hayat, X. Zhou, and J. P. R. David, "Relating the experimental ionization coefficients in semiconductors to the nonlocal ionization coefficients," *IEEE Trans. Electron Devices*, vol. 62, no. 6, pp. 1946-1952, June 2015.

[31] R.J. McIntyre, "Multiplication noise in uniform avalanche photodiodes," *IEEE Trans. Electron Devices*, vol. ED-13, pp. 164–168, 1966.

[32] F. Tavernier and M. S. J. Steyaert, "High-speed optical receivers with integrated photodiode in 130 nm CMOS," *IEEE J. Solid-State Circuits*, vol. 44, no. 10, pp. 2856-2867, Oct. 2009.

[33] B. Nakhkoob, S. Ray, and M. M. Hella, "High speed photodiodes in standard nanometer scale CMOS technology: a comparative study," *Opt. Exp.*, vol. 20, no. 10, pp. 11256-11270, May 2012.

[34] Y. Kang, M. Morse, M. J. Paniccia, M. Zadka, Y. Saad, G. Sarid, A. Pauchard, W. S. Zaoui, H.-W. Chen, D. Dai, J. E. Bowers, H.-D. Liu, D. C. Mcintosh, X. Zheng, and J. C. Campbell, "Monolithic Ge/Si avalanche photodiodes," *Proc. 6th IEEE Int. Conf. Group IV Photonics*, San Francisco, CA, USA, pp. 25–27, Sept. 9-11, 2009.

[35] K. S. Lau, C. H. Tan, B. K. Ng, K. F. Li, R. C. Tozer, J. P. R. David, and G. J. Rees, "Excess noise measurement in avalanche photodiodes using a transimpedance amplifier front-end," *Meas. Sci. Technol.*, vol. 17, no.7, pp. 1941–1946, June 2006.

[36] L. Qiao, J. S. Cheong, J. S. L. Ong, J. S. Ng, A. B. Krysa, J. E. Green, and J. P. R. David, "Avalanche noise in $Al_{0.52}In_{0.48}P$ diodes," *IEEE Photon. Technol. Lett.*, vol. 28, no.4, pp. 481-484, Feb. 2016.

[37] G. N. Lu, M. B. Chouikha, G. Sou, and M. Sedjil, "Colour detection using a buried double p-n junction structure implemented in the CMOS process," *Electron. Lett.*, vol. 32, pp. 594-596, Mar. 1996.

[38] M. M. Hossain, S. Ray, J. S. Cheong, L. Qiao, A. N. A. P. Baharuddin, M. M. Hella, J. P. R. David, and M. M. Hayat, "Low-noise speed-optimized large area CMOS avalanche photodetector for visible light communication," *IEEE/OSA J. Lightwave Technol.*, vol. 35, no. 11, pp. 2315-2324, June 2017.

Chapter 4

Exact Analytical Formula for the Excess Noise Factor for Mixed Carrier Injection Avalanche Photodiodes

4.1 Abstract

The well-known analytical formula for the excess noise factor associated with avalanche photodiodes (APDs), developed by R. J. McIntyre in 1966, assumes the injection of either an electron or a hole at the edge of the APD's avalanche region. This formula, however, is not applicable in cases when photons are absorbed inside the avalanche region, and its use may severely underestimate or overestimate the actual excess noise factor depending on the absorption profile and the hole-to-electron ionization coefficient ratio, *k*. Here, an easy-to-use exact analytical formula is derived for the excess noise factor of APDs while taking into account a mixed-carrier initiated avalanche multiplication process, which is triggered by a parent electron-hole pair at an arbitrarily specified location within the multiplication region. The derivation relies on analytically solving a special case of a previously reported recursive integral equations [Hayat *et al.*, IEEE Trans. Electron Devices, vol. 39, no. 3, pp. 546-552, 1992]. In addition, an expression for the excess noise factor is presented in the case when the location of the parent electron-hole pair within the multiplication region obeys an arbitrary exponential distribution. The results show that in contrast to the case of edge parent-electron injection, when mixed injection is allowed even a small level of hole ionization (e.g., small k~0.0001) causes the excess noise factor to increase dramatic, depending on the absorption profile as it ranges from narrow to flat within the multiplication region. The theoretical results are validated against experimental results for Si APDs.

4.2. Introduction

Avalanche photodiodes (APDs), with their high internal gain, are widely used in optical communication systems due to the improvement they offer to the receiver's signal-to-noise ratio (SNR). The receiver performance is strongly dependent on the APDs mean gain (M) and the excess noise factor (F), which represents the random fluctuations in the gain. Thus, availability of analytical expressions for M and F is important for calculating the SNR as well as the bit-error probability in optical receivers [1]. The quantities M and F are commonly related to the hole-to-electron ionization coefficient ratio, k, as expressed in McIntyre's original theory [2] dating back to 1966. The F value is at a minimum for materials with a small value of k and electron edge injection (or very large k for hole edge injection), namely when a parent electron (hole) is injected into the appropriate edge of the multiplication region, resulting in a chain of impact ionizations. In reality, however, mixed-carrier injection can occur in the multiplication region (MR), whereas photons are absorbed inside the MR [2]. Such scenario results in a parent electron-hole pair inside the MR initiating the avalanche multiplication process, where each parent carrier independently and individually creates its own chain of impact ionizations.

It turns out that mixed injection plays an important role in the behavior of F as a function of M, as originally pointed out by Webb *et al.* in [3]. For example, we will show in this paper even when k is very low (~0.0001), F begins to increase dramatically beyond a certain threshold value of M if mixed injection is allowed. Moreover, the mean gain threshold at which F becomes large is determined as a function of the location of mixed injection and k. The main contribution of this paper is to develop an exact analytical

formula for F in the case of mixed-injection avalanche multiplication process. Consequently, depending on the photon absorption profile within the MR, photogenerated carriers within the MR contribute collectively to the mixed-injection multiplication in a distributed fashion. Thus, for a given APD structure, M and F may actually depend indirectly on the wavelength of light. Note that the small values of k of 0.01 or lower are important from a practical standpoint as there are several bulk materials that exhibit this type of mixed-injection behavior including Si [4]-[5], InAs [6], and AlAsSb [7]. In addition, high values of k (>0.1) are also important for submicron multiplication regions (e.g., Si *pn*-junction APDs), where the very high electric fields (>255 kV/cm) cause an increase in the k value [8], [9].

Although McIntyre developed a closed-form formula for the mean gain in the case of mixed injection, he did not offer a formulation of the excess noise factor in such a case [2]. In 1992, Hayat *et al.* formulated an analytical model [10] for avalanche multiplication that allowed the determination of the excess noise factor in the case of mixed injection. The power of the formulation in [10] was that it captured the effect of dead space, which is the minimum distance a carrier must travel after an impact ionization before it may effect another ionization. However, only numerical solutions were produced and a simple formula remained elusive [10]. In 2017, Hossain *et al.* used the numerical approach to further calculate the excess noise factor for Si APDs in the case of distributed mixed injection [9], where the photon absorption profile within the MR was taken into account. Experiments have also shown the wavelength dependence of the excess-noise factor; moreover, good agreement between numerical solutions of the analytical model and experiments on the role of mixed injection has been shown [5], [8]-

[12]. The experiments and the numerically calculated *F* under mixed injection were also compared with that calculated using the McIntyre's formula [2], which assumes edge injection. For example, the comparison showed that McIntyre's *F* significantly overestimated the measured *F* for CMOS APDs [8].

To the best of our knowledge, there is no analytical formula for the excess noise factor in the case of mixed injection. The most relevant work relevant to a closed-form formula for the excess noise factor in the case of mixed injection is the work of Hayat *et al.* [13]. The article shows exact analytical expressions for *M* and *F* under edge injection by finding an exact analytical solution to the recursive integral equations [10] that characterize the first and second moments of the populations of electrons and holes under mixed injection. This approach is termed the characteristic method (CM). Although the expression for *M* is simple, the expression for *F* involves the inversion of a 9 by 9 matrix. The article in [13] also did not provide explicit formulas for *F* under mixed injection.

In this work, we revisit the CM approach to derive an exact analytical formula of the excess noise factor for mixed carrier injection with zero dead space. The analytically calculated *F* is compared with that calculated numerically using dead-space multiplication theory (DSMT) [10], and good agreement is shown. In addition, expressions for the analytical mean gain and excess noise factor are presented while taking into account different absorption profiles using an exponential decay function. Moreover, previously reported *F* for the P+/N-well CMOS APD [9] are compared with that analytically calculated under mixed injection case and good agreement is shown.

4.3 Analytical Model

Consider the multiplication region of an APD extended from $x = 0$ to $x = W$, where W is

the avalanche multiplication-region width. It is further assumed that the avalanche multiplication process is initiated by a photogenerated electron-hole pair within the MR. Now consider a parent electron and a parent hole that are located at position x within the multiplication region. Electrons are assumed to travel in the positive x-direction at their saturation velocity under the influence of electric field and they are capable of impact ionizing with an ionization coefficient, α. Similarly, holes travel in the negative x-direction and are capable of impact ionizing with an ionization coefficient, β. This avalanche process produces a net stochastic gain, $G(x)$, when all the carriers have exited the MR; this quantity is the total number of electron-hole pairs generated as a result of a single parent electron-hole pair, located at x, initiating the multiplication process. Next, we analyze the statistics of $G(x)$.

Following Hayat *et al*. [10], assume that $Z(x)$ is the random sum of electrons and holes produced by an electron, including the initiating parent electron. Similarly, let $Y(x)$ be the random number of all electrons and holes produced by the hole and its offsprings, including the initiating parent hole. Note that $Z(W) = 1$ and $Y(0) = 1$. Moreover, $G(x) = \frac{1}{2}[Z(x) + Y(x)]$. Now consider $z(x) = \langle Z(x) \rangle$ and $y(x) = \langle Y(x) \rangle$, which are the means of $Z(x)$ and $Y(x)$, respectively; similarly, $z_2(x) = \langle Z^2(x) \rangle$ and $y_2(x) = \langle Y^2(x) \rangle$ are the second moments of $Z(x)$ and $Y(x)$, respectively. Here, the bracket denotes ensemble average. The mean of $G(x)$ is obtained from the quantities of $z(x)$ and $y(x)$:

$$M(x) = \langle G(x) \rangle = \frac{1}{2}[z(x) + y(x)]. \quad (1)$$

On the other hand, the second moment of the gain in the case of a mixed-carrier initiated avalanche is given by

$$\langle G^2(x) \rangle = \frac{1}{4}[z_2(x) + 2\, z(x)y(x) + y_2(x)]. \quad (2)$$

Finally, in this paper, we define the mixed-injection excess-noise factor, $F(x)$, as follows:

$$F(x) = \frac{<G^2(x)>}{<G(x)>^2}. \tag{3}$$

The above equations require knowledge of the ionization coefficients for electrons (α) and holes (β), respectively. The electric-field dependent ionization coefficients are often modeled using Chynoweth's formula [14]:

$$\alpha(E) = A_e exp\left[-\left(\frac{B_e}{E}\right)^{m_e}\right] \tag{4a}$$

and

$$\beta(E) = A_h exp\left[-\left(\frac{B_h}{E}\right)^{m_h}\right], \tag{4b}$$

where E is the electric field and the A, B, and m are material-dependent parameters, and they are chosen from experimental and fitted data [9]. The electric field within the MR in conjunction with the ionization coefficients, α and β, are used in (3) to predict the injection-position dependent excess-noise factor under mixed injection case.

A. Formula for Mixed-Injection Mean Gain

In order to obtain an exact analytical formula for $M(x)$, we solve the recursive integral equations from the DSMT model [10] with zero dead space to obtain the first moments of electrons and holes, $z(x)$ and y(x), respectively, under mixed injection. The recursive integral equations for the means of $Z(x)$ and $Y(x)$ are equations (14) and (15) in [10]:

For $0 \le x \le w$

$$z(x) = \left[1 - (1 - e^{-\alpha(W-x)})u(W-x)\right] + \int_x^W [2z(\xi) + y(\xi)]\alpha e^{-\alpha(\xi-x)}u(\xi-x)d\xi, \tag{5a}$$

and

$$y(x) = \left[1 - (1 - e^{-\beta x})u(x)\right] + \int_0^x [2y(\xi) + z(\xi)]\beta e^{-\beta(x-\xi)}u(x-\xi)d\xi \tag{5b}$$

where $u(x) = 1$ for $x \ge 0$, and 0 otherwise.

Upon differentiation with respect to *x* and simple back substitution, the differential forms of the above integral equations are

$$z'(x) + \alpha[z(x) + y(x)] = 0, \tag{6a}$$

and

$$y'(x) - \beta[z(x) + y(x)] = 0 \tag{6b}$$

with the boundary conditions, $z(w) = 1$ and $y(0) = 1$. The approach we undertake to solve for $z(x)$ and $y(x)$ exactly is based on proposing exponential-form solutions, as done in [10]. The desired exponents are then found by substituting these assumed exponential forms in (6a) and (6b), and obtaining an algebraic *characteristics equation* characterizing the exponents that result in self consistency in (6a) and (6b). More precisely, the general structure of the solution is a superposition of terms of the form

$$z(x) = c_1 e^{rx}, \tag{7a}$$

and

$$y(x) = c_2 e^{rx} \tag{7b}$$

where c_1 and c_2 are the unknown coefficients and *r* is a solution to the characteristic equation.

After we substitute these general solutions from 7(a) and 7(b) into 6(a) and 6(b), respectively, we obtain the matrix equation

$$\begin{bmatrix} (r+\alpha) & \alpha \\ -\beta & (r-\beta) \end{bmatrix} \begin{bmatrix} c_1 \\ c_2 \end{bmatrix} = \begin{bmatrix} 0 \\ 0 \end{bmatrix}. \tag{8}$$

For a nontrivial (i.e., nonzero) solution to c_1 and c_2 in (8), we require that matrix above to be singular (its determinant must be zero), which results in the characteristic equation characterizing *r*:

$$(r + \alpha)(r - \beta) + \alpha\beta = 0. \tag{9}$$

We begin by considering the case when electron and hole ionizations are unequal, in which case (9) has two roots: $r_1 = 0$ and $r_1 \equiv r = \beta - \alpha \neq 0$. The general solution in this case becomes

$$z(x) = c_1 + c_1' e^{rx} \tag{10a}$$

and

$$y(x) = c_2 + c_2' e^{rx}. \tag{10b}$$

Upon substituting the general solutions from (10a) and (10b) into (6a) and applying the boundary conditions $z(w) = y(0) = 1$, we obtain a system of four linear equations with four unknown coefficients c_1, c_1', c_2, and c_2' with *r*. After some algebra, the unknown coefficients are determined and the first moments of $z(x)$ and $y(x)$ are obtained as follows (details of solutions are provided in the Appendix):

$$z(x) = \frac{(r+\alpha+\alpha e^{rw})-2\alpha e^{rx}}{(r+\alpha-\alpha e^{rw})} \tag{11a}$$

and

$$y(x) = \frac{-(r+\alpha+\alpha e^{rw})+2(r+\alpha)\, e^{rx}}{(r+\alpha-\alpha e^{rw})}\,. \tag{11b}$$

Next, the analytical expression for the mean-gain for a mixed-carrier initiated avalanche, *M*(*x*), is obtained from the quantities of z(*x*) and *y*(*x*). Specifically, we maintain that

$$M(x) = \frac{re^{rx}}{r+\alpha-\alpha e^{rw}} = \frac{(\beta-\alpha)e^{(\beta-\alpha)x}}{\beta-\alpha e^{(\beta-\alpha)w}}; \tag{12a}$$

or equivalently,

$$M(x) = \frac{(1-k)e^{-\alpha(1-k)x}}{e^{-\alpha(1-k)w}-k}, \tag{12b}$$

where $k = \frac{\beta}{\alpha}$. This expression was previously derived by McIntyre (equation (5) in [2]) using a different method.

In addition, the expression for ionization parameter, αw, in terms of *k*, *M*(*x*) and the

mixed-injection location (x/w) within the MR is derived as

$$\alpha w = \ln\left(\frac{e^{(1-k)}}{k} - \frac{(1-k)e^{(1-k)(\frac{x}{w})}}{kM(x)}\right). \tag{13a}$$

Recall that for an APD device, avalanche breakdown occurs for a value of ionization parameter for which the mean gain $M(x)$ is infinite. In this case, (13) becomes

$$(\alpha w)_b = \ln \frac{e^{(1-k)}}{k} \quad . \tag{13b}$$

Hence, the breakdown condition is independent of the location of the parent injection, x.

For the case of electron injection ($\beta < \alpha$, hence $k < 1$, and $x = 0$), (12) collapses to the well-known McIntyre's classical mean-gain formula in the case of edge electron-injection [2]:

$$M_e = M(0) = \frac{\beta - \alpha}{\beta - \alpha e^{(\beta - \alpha)w}} = \frac{1-k}{e^{-\alpha(1-k)w} - k} \tag{14a}$$

Similarly, for hole injection ($\beta > \alpha$, equivalently $k > 1$ and $x = w$), (12) becomes

$$M_h = M(w) = \frac{\beta - \alpha}{\beta e^{-(\beta - \alpha)w} - \alpha} = \frac{1-\frac{1}{k}}{e^{-\beta\left(1-\frac{1}{k}\right)w} - \frac{1}{k}}. \tag{14b}$$

Next, consider the case $k = 0$ in (14a) or $k = \infty$ in (14b), and obtain

$$M_e = e^{\alpha w} \tag{15a}$$

and

$$M_h = e^{\beta w}. \tag{15b}$$

Similarly, to consider the case when $k = 1$ in (12), and (14), we take the limit as $k \rightarrow 0$ (or $k \rightarrow \infty$) and obtain the familiar position-independent formula

$$M(x) = \frac{1}{1-\alpha w}. \tag{16}$$

The special-case expressions in (15) and (16) are the well-known McIntyre formulas (equations (21) and (24) in [15]).

We note that the approach followed in this paper to obtain the mixed-injection mean gain is intrinsically different from that followed by McIntyre. Unlike McIntyre's approach, the approach here lends itself to a solution of the mixed-injection excess noise factor, as described next.

B. Formula for Mixed-Injection Excess-Noise Factor

In order to obtain an exact analytical formula for $F(x)$, we solve the recursive integral equations from the DSMT model [10] with zero dead space and $k \neq 1$ to obtain the second moments of electrons and holes, $z_2(x)$ and $y_2(x)$, respectively, under mixed injection. The recursive integral equations for the second moments of $Z(x)$ and $Y(x)$ are equations (22) and (23) in [10] and they are expressed below:

For $0 \leq x \leq w$,

$$z_2(x) = \left[1 - (1 - e^{-\alpha(W-x)})u(W-x)\right] + \int_x^W [2z_2(\xi) + y_2(\xi) + 4z(\xi)y(\xi) + 2z^2(\xi)]\alpha e^{-\alpha(\xi-x)}u(\xi-x)d\xi \tag{17a}$$

and

$$y_2(x) = \left[1 - (1 - e^{-\beta x})u(x)\right] + \int_0^x [2y_2(\xi) + z_2(\xi) + 4z(\xi)y(\xi) + 2y^2(\xi)]\beta e^{-\beta(x-\xi)}u(x-\xi)d\xi \tag{17b}$$

where, $u(x) = 1$ for $x \geq 0$, and 0 otherwise.

The differential forms of the above recurrence equations are

$$z_2'(x) + \alpha[z_2(x) + y_2(x)] = -2\alpha z(x)\big(2y(x) + z(x)\big), \tag{18a}$$

and

$$y_2'(x) - \beta[z_2(x) + y_2(x)] = 2\beta y(x)(2z(x) + y(x)), \tag{18b}$$

with the boundary conditions, $z_2(w) = 1$ and $y_2(0) = 1$.

Note that right-hand side of (18a) and (18b) is explicitly determined by substituting the previously derived expressions given by (11a) and (11b). To solve the above inhomogeneous differential equations exactly, we assume a general solution (combination of complementary and particular solution) to the unknown functions $z_2(x)$ and $y_2(x)$ in the form

$$z_2(x) = p_1 e^{rx} + p_2 e^{2rx} + p_3 x e^{rx} + p_4 x + p_5, \tag{19a}$$

and

$$y_2(x) = q_1 e^{rx} + q_2 e^{2rx} + q_3 x e^{rx} + q_4 x + q_5. \tag{19b}$$

The exponent *r* turns out to satisfy the same characteristic equation as in (9). Upon substituting the proposed forms from (19a) and (19b) into (18a) and (18b) and applying boundary conditions $z_2(w) = y_2(0) = 1$, we obtain a system of twelve linear equations with ten unknown coefficients p_1, p_2, p_3, p_4, p_5 , q_1, q_2, q_3, q_4, and q_5. After some algebra, the unknown coefficients are determined and second moments of $z_2(x)$ and $y_2(x)$ are obtained. Details of solutions are provided in the Appendix.

Finally, the analytical expression for the excess noise factor for a mixed-carrier initiated avalanche, $F(x)$ is obtained from the quantities of $z(x)$, $y(x)$, $z_2(x)$ and $y_2(x)$ as follows:

$$F(x) = \frac{<G^2(x)>}{<G(x)>^2} = \frac{\frac{1}{4}[z_2(x) + 2\,z(x)y(x) + y_2(x)]}{\left(\frac{1}{2}[z(x) + y(x)]\right)^2}. \tag{20a}$$

Hence, upon simplification we obtain

$$F(x) = 2 - \left\{\frac{(\beta - \alpha e^{2rw})}{(\beta - \alpha e^{rw})}\right\} e^{-rx} = 2 - \left\{\frac{e^{-2\alpha(1-k)w} - k}{e^{-\alpha(1-k)w} - k}\right\} e^{\alpha(1-k)x}, \quad (20b)$$

where $k = \frac{\beta}{\alpha}$ and $r = \beta - \alpha \neq 0$.

The excess-noise factor, $F(x)$, can also be represented in terms of mean-gain, $M(x)$, and k:

$$F(x) = k\, M(x) e^{2\alpha(1-k)x} + 2\left(1 - k e^{\alpha(1-k)x}\right) - \frac{1}{M(x)}(1-k) \quad (21)$$

The formula in (20) (or (21)) is the generalization of McIntyre's formula for the excess noise factor to mixed injection and it constitutes the first major contribution of this paper. For the case of electron injection ($\beta < \alpha$, hence $k < 1$, and $x = 0$), (21) collapses to the well-known McIntyre's [2] formula:

$$F_e = F(0) = k\, M_e + \left(2 - \frac{1}{M_e}\right)(1-k) \quad (22a)$$

Similarly, for hole injection ($\beta > \alpha$, equivalently $k > 1$ and $x = w$), (21) becomes

$$F_h = F(w) = \frac{M_h}{k} + \left(2 - \frac{1}{M_h}\right)\left(1 - \frac{1}{k}\right) \quad (22b)$$

Next, consider the case when $k = 0$ in (22a) or $k = \infty$ in (22b). In these cases, we obtain

$$F_e = 2 - \frac{1}{M_e} \quad (23a)$$

and

$$F_h = 2 - \frac{1}{M_h} \quad (23b)$$

To address the case when $k = 1$, we take the limit as $k \rightarrow 1$ in (21) and obtain the familiar formula

$$F(x) = M(x) = \frac{1}{1 - \alpha w}, \quad (24)$$

The special-case expressions in (23) and (24) are those as given by (19) and (22) in [15].

C. Analytical Expressions for Distributed Mixed-Injection M and F with an Exponential Decay Function

Ideally, pure electron (e.g., for Si with low *k*) or pure hole (e.g., for InP with high *k*) edge injection yields the lowest value of *F*. This can be seen from the expression for $F(x)$ in (21). However, depending on the photon absorption profile inside the MR, photogenerated carriers within the MR also contribute collectively to the mixed-injection multiplication in a distributed fashion. Thus, for a given APD structure, *F* and *M* actually depend indirectly on the wavelength (or more generally on the spectrum) of light. In this regard, we present analytical expressions for *M* and *F* while taking into account different absorption profiles within the MR.

Consider an incident photon that is absorbed in the multiplication region ($0 \le x \le w$) with probability p_m. The generation rate for mixed carrier injection is proportional to $e^{-\alpha' x}$, where α' is the material absorption coefficient. When the absorption profile is normalized by $p_m / \int_0^w e^{-\alpha' x} dx$, we obtain the probability density function (pdf) of the location of absorption within the multiplication region, namely $g(x) = \frac{\alpha' e^{-\alpha' x}}{1 - e^{-\alpha' w}}$.

The mean gain for the mixed-carrier initiated avalanche, $M_a(x) = < G_a(x) >$, is obtained from the quantities $z(x)$ and $y(x)$ while taking into account the absorption profile within the MR. More precisely,

$$M_a(x) = = \int_0^w \frac{1}{2} [z(x) + y(x)]\, g(x) dx. \tag{25}$$

By inserting the values of $z(x)$, $y(x)$ into (25), we obtain the following analytical expression for the distributed-injection mean gain:

$$M_a(x) = \frac{\alpha'(1-k)(e^{(-(1-k)\alpha - \alpha')w} - 1)}{(e^{-\alpha(1-k)w} - k)(1 - e^{-\alpha' w})(-\alpha(1-k) - \alpha')}. \tag{26}$$

Similarly, the second moment of mean avalanche gain for the mixed-carrier initiated avalanche,$< G_a^2(x) >$, is obtained from the quantities $z(x)$, $y(x)$, $z_2(x)$, and $y_2(x)$ while taking into account the absorption profile within the MR. The expression for $< G_a^2(x) >$ is

$$< G_a^2(x) > = \int_0^w \frac{1}{4} [z_2(x) + 2\, z(x)y(x) + y_2(x)]\, g(x)dx. \tag{27}$$

Moreover, the distributed-injection excess noise factor $F_a(x)$ with absorption profile is expressed as

$$F_a(x) = \frac{<G_a^2(x)>}{M_a(x)^2}, \tag{28}$$

which reduces to

$$F_a(x) = \frac{\frac{\alpha'}{1-e^{-\alpha' w}}\left[\left\{\frac{2(e^{(-2\alpha(1-k)-\alpha')w}-1)}{-2\alpha(1-k)-\alpha'}\right\}-\left\{\frac{e^{-2\alpha(1-k)w}-k}{e^{-\alpha(1-k)w}-k}\right\}\left\{\frac{(1-e^{(-\alpha(1-k)-\alpha')w})}{\alpha(1-k)+\alpha'}\right\}\right]}{\left\{\frac{\alpha'}{1-e^{-\alpha' w}}\frac{(e^{(-\alpha(1-k)-\alpha')w}-1)}{-\alpha(1-k)-\alpha'}\right\}^2}. \tag{29}$$

The formula in (29) is the generalization of McIntyre's formula for the excess noise factor to distributed injection and it constitutes the second major contribution of this paper.

4.3 Results

The mean gain, $M(x)$, as a function of the electron ionization parameter, αw, is shown in Fig. 4.1, resulting from the expression as in (12). Six cases of the hole-to-electron ionization coefficient ratio (k) and three cases of relative mixed-injection parameter (x/w) are considered. The k values are 0.0001, 0.001, 0.01, 0.1, 0.5, and 0.9 and x/w values are 0, 0.5 and 1. The mean-gain curves show dependence on the k values but not on the injection location x. This is also evident form (13b). As k approaches unity, the mean gain curves are almost overlapping for different locations of mixed injection within MR. This

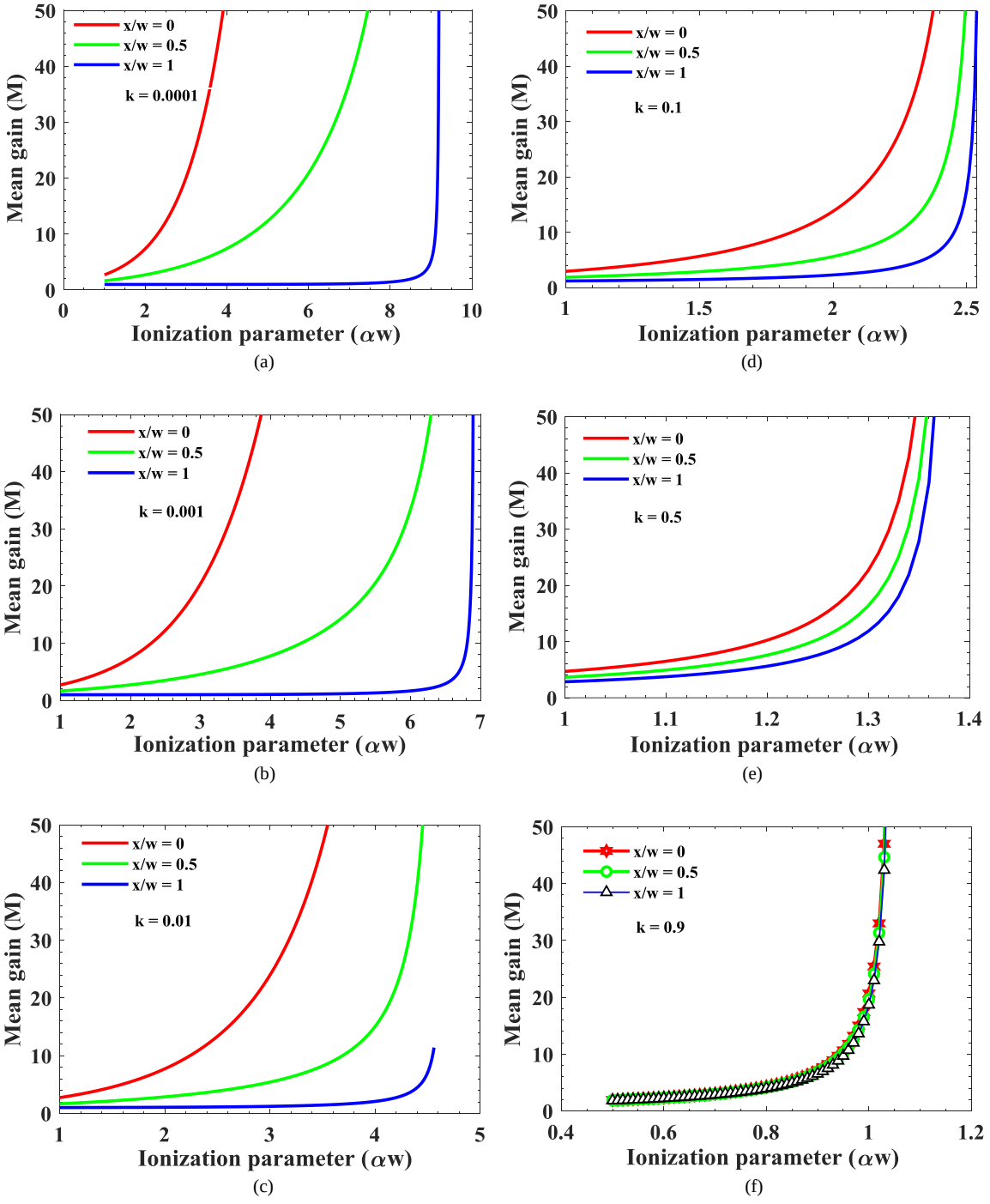

Figure 4.1: Mean-gain, $M(x)$, as a function of the electron ionization parameter, αw. Six cases of hole-to-electron ionization coefficient ratio (k) and three cases of relative mixed-injection parameter (x/w) are considered with k values of 0.0001, 0.001, 0.01, 0.1, 0.5, and 0.9 and x/w values of 0, 0.5 and 1 [24].

is clear from the behavior in the case of $k = 1$, as expressed in (16).The behavior of $F(x)$ as a function of $M(x)$ is shown in Fig. 4.2, which results from the exact analytical formula

shown in (21). Six cases of k and three cases of relative mixed-injection parameter (x/w) are considered. The k values are 0.0001, 0.001, 0.01, 0.1, 0.5, and 0.9, and the x/w values are 0, 0.5 and 1. As expected, the excess noise factor shows strong dependence on mixed-injection location for different values of k. In general, the excess noise factor is at a minimum for materials with a small value of k and edge electron-injection (or very large k for edge hole-injection), namely when the parent electron (hole) is injected at the appropriate edge of the multiplication region. However, in contrast to the case of edge parent-electron injection, even when k is very low, i.e., k = 0.0001, the excess-noise factor behavior shows dramatic increase with the mixed injection location (x/w ranging from 0 to 1) within the MR, as seen from Fig. 4.2. It turns out that mixed injection plays an important role in the behavior of $F(x)$ as a function of $M(x)$ as well as injection location and k values.

For validation purposes, the excess noise factor calculated using the formula in (21) is also compared with that calculated using exact numerical method (ENM) [10] for k values of 0.1, 0.5 and 0.9, respectively (see Fig. 4.2); the good agreement between the two approaches is evident. In summary, the excess noise factor increases dramatically with the mean gain when mixed injection is allowed within the MR. More precisely, $F(x)$ increases with the location of the mixed injection and k. For example, F increases by a factor of 1.4 at M = 20 for k = 0.0001 when edge injection is replaced by mixed-injection at x/w = 0.5. In addition, even when k is very low (~0.0001), F begins to increase dramatically beyond a certain threshold value of M = 10 when mixed injection is allowed. Moreover, the mean gain threshold at which F becomes large is determined as a function of the location of mixed injection and k. The results show that relying on the k value

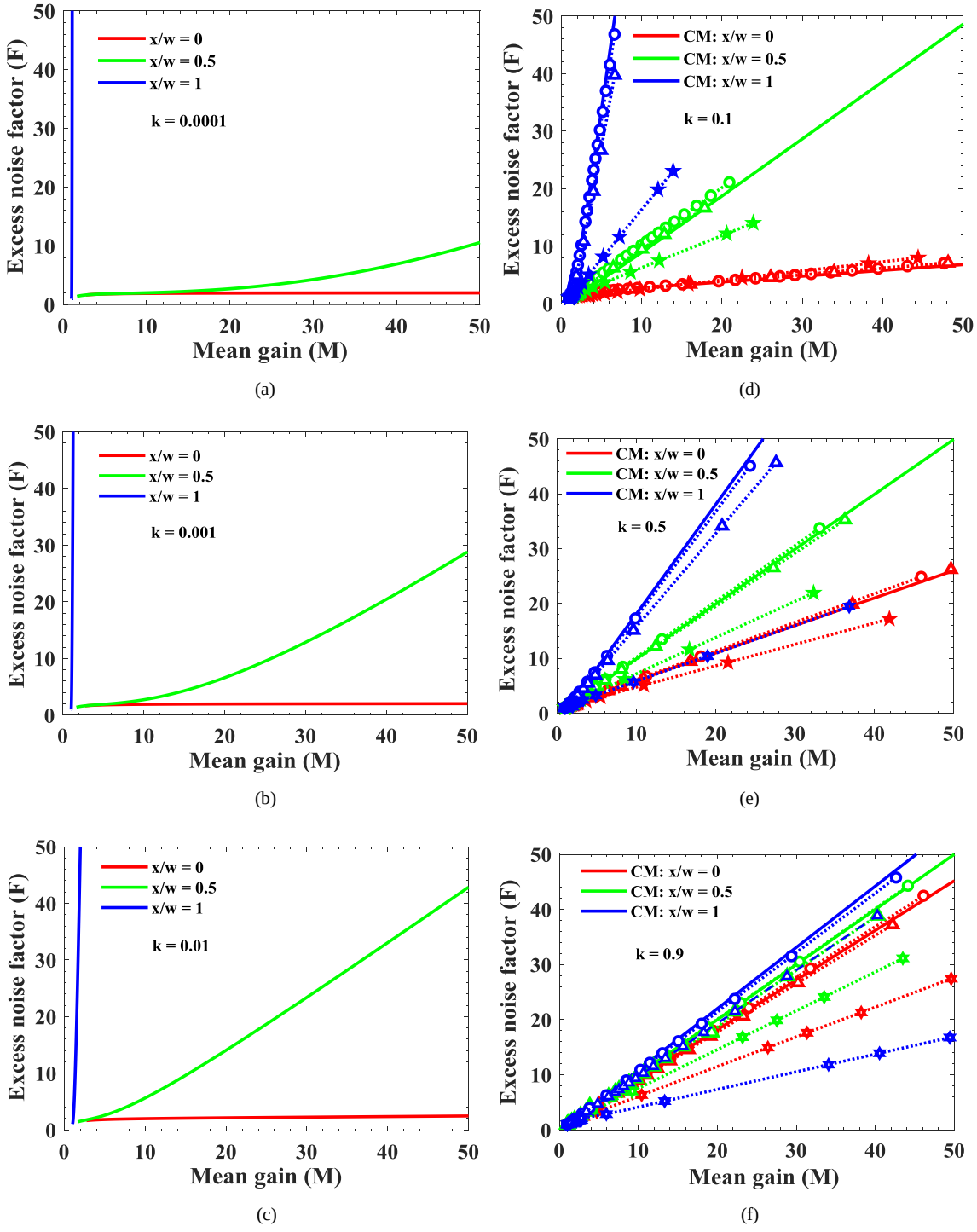

Figure 4.2: Excess-noise factor, $F(x)$, as a function of mean gain, $M(x)$. Six cases of hole-to-electron ionization coefficient ratio (k) and three cases of relative mixed injection parameter (x/w) are considered. The k values are 0.0001, 0.001, 0.01, 0.1, 0.5, and 0.9 and x/w values are 0, 0.5 and 1. Excess noise factor calculated using CM approach is compared with that calculated using ENM for k = 0.1, k = 0.5 and k = 0.9, respectively. For ENM, the values of normalized dead space (d/w) are chosen to be 0, 0.01, and 0.1 and are represented by ··○··, ··Δ··, and ··★··, respectively. In addition, red, green, and blue lines represent relative mixed injection parameter (x/w) with the values of 0, 0.5 and 1, respectively [24].

alone, as we were taught by McIntyre's theory, can be very misleading when mixed injection is a factor.

The pdf, $g(x)$, of the photon absorption location as a function of absorption depth (x) is shown in Fig. 4.3. The exponential absorption profiles are arbitrarily chosen from narrow to flat, based on the α' values from 10 to 0.01.

The behavior of the excess noise factor as a function of mean gain for different absorption profiles is shown in Fig. 4.4, which results from the exact analytical formulas shown in (26) and (29). Six cases of k and four cases of absorption profiles are considered. In addition, McIntyre's k lines (i.e., $x/w = 0$) are shown using the dotted lines with k assuming the values of 0.0001, 0.001, 0.01, and 0.1 to 1 with an increment of 0.1. Figure 4.4 shows that excess noise factor increases with the narrow to flat absorption profile. For example, F increases by a factor of 2.35 at $M = 20$ for $k = 0.0001$ when a very narrow absorption profile ($\alpha' = 10$) is replaced by a nearly flat profile ($\alpha' = 0.01$). In addition, even when k is very low (~0.0001), F begins to increase dramatically beyond

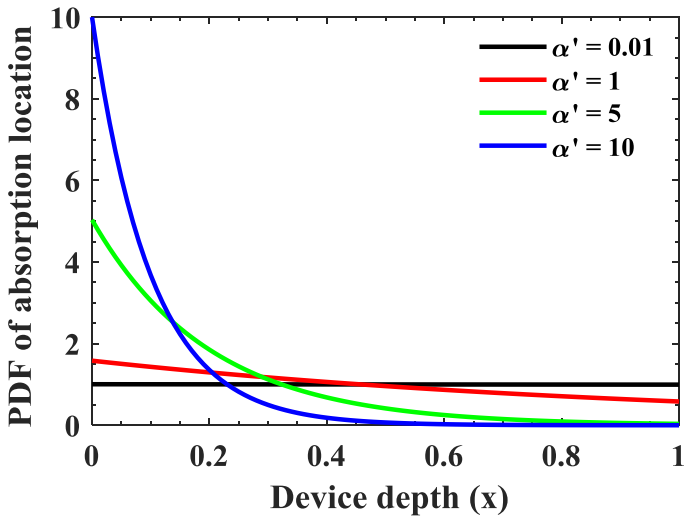

Figure 4.3: Probability density function (PDF) of the photon absorption location as a function of the absorption location (x) for different absorption coefficient (α') from flat to narrow with an exponential decay function [24].

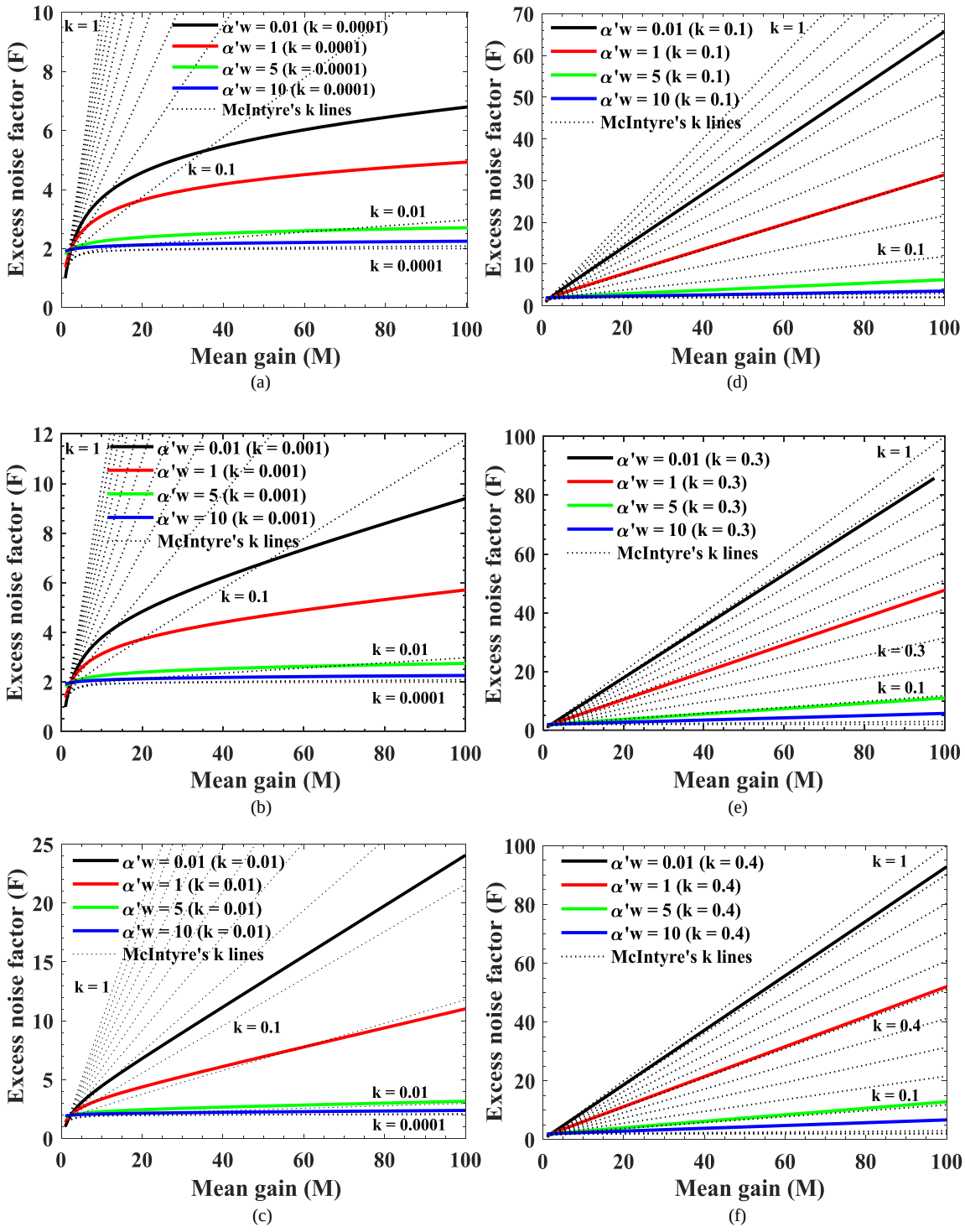

Figure 4.4: Excess-noise factor (F) as a function of mean gain (M) for different absorption profiles with an exponential decay function. Six cases of hole-to-electron ionization coefficient ratio (k) are considered. The k values are 0.0001, 0.001, 0.01, 0.1, 0.3 and 0.4. In addition, McIntyre's k (β/α) lines (i.e., x/w = 0) are shown using the dotted lines: 0.0001, 0.001, 0.01 and 0.1 to 1 with an increment of 0.1 [24].

a certain threshold value of M = 2.5 if mixed injection is allowed—a behavior that is very

different from that seen in the case of edge injection. Moreover, the mean gain threshold at which *F* becomes large is governed by the absorption profile and *k*.

Additionally, for a particular *k* value, the shape of the distributed *F* versus the distributed *M* is now very different from what McIntyre formula predicts, as shown in Fig. 4.4. Overall, McIntyre's *F* either underestimates or overestimates the distributed *F*, depending on the photon-absorption profile and value of *k*. For example, as shown in Fig. 4.4(a), McIntyre's *F* at *M* = 20 with low value of *k* (~0.0001), underestimates the distributed *F* by the factors of 0.92, 0.81, 0.53, and 0.42 for narrow to nearly flat absorption profiles with α' values of 10, 5, 1, and 0.01, respectively. However, for high value of *k* (*k* = 0.1 in Fig. 4.4(d)), McIntyre's *F* at *M* = 20 overestimates the distributed *F* by the factors of 1.29 and 1.61 for the narrow absorption profiles with α'values of 5 and 10, respectively. At the same time, for broader absorption profiles associated with the same *k* value of 0.1, McIntyre's *F* at *M* = 20 underestimates the distributed *F* by the factors of 0.5 and 0.26 for α' values of 1 and 0.01, respectively. Note that the small values of *k* of 0.01 or lower are important from a practical standpoint as there are several bulk materials that exhibit this type of behavior, including Si [4], [5] InAs [6], and AlAsSb [7]. In addition, high values of *k* (>0.1) are also important for submicron multiplication regions (e.g., Si *pn*-junction APDs), where the very high electric fields (>255 kV/cm) cause an increase in the *k* value [8], [9]. For example, the value of *k* for a *p*-*n* junction Si APD for typical operation is in the range of 0.1 – 0.56 for the high field values in the range of 255 – 900 kV/cm [9]. As seen from Fig. 4.4(f), for high values of *k* (~0.4), *F* exhibits a dramatic increase (by a factor of 6.6 at *M* = 20) from a narrow absorption profile (α' = 10) to a nearly flat profile (α' = 0.01). Such increase is very dramatic for a *k* value of 0.4, as compared to an increase

by a factor of 2.35 for a low k value of 0.0001 with similar absorption profiles.

In summary, our analytical results indicate that McIntyre's formula for F may either underestimate or overestimate the distributed-injection F, depending on the photon-absorption profile and the value of k. Hence, usage of both k and the photon-absorption distribution profile in the distributed-injection formula for F can be critical in the reliable prediction of F in many real devices that involve mixed injection.

4.4 Experimental Validation of the Theory

McIntyre's edge-injection formula for F can be inaccurate when applied to APDs with submicron multiplication region widths (e.g., <500 nm) and high values of k (e.g., >0.12) [4] [Si], [8]-[9][Si], [11][GaAs], [12][Si]. One of the main reasons for such inaccuracy is the presence of mixed injection. For example, McIntyre's formula for F overestimated the measured F (at 830 nm excitation with k = 0.12) for a n^+-p-π-p^+ reach-through Si APD [4]. Other examples are low-noise CMOS APDs with a 470 nm multiplication region

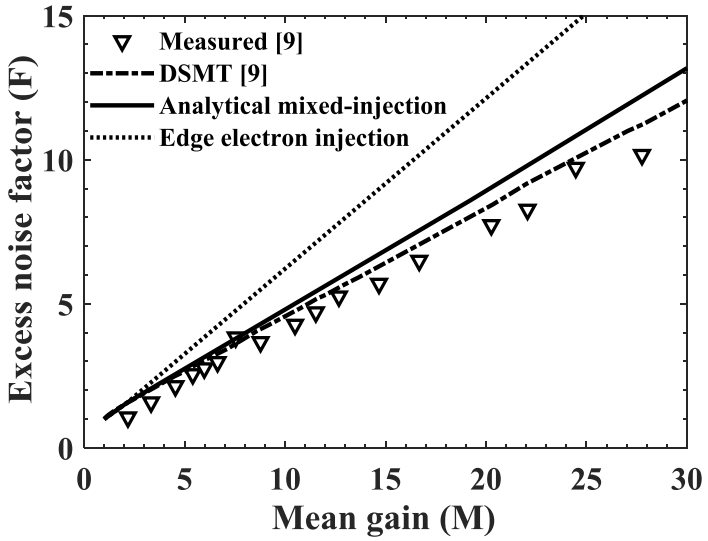

Figure 4.5: Excess-noise factor (F) as a function of mean gain (M) for the N-well/P-sub CMOS APD. The triangles are the measured values reproduced from [9] using a 633 nm He-Ne laser. The solid and dotted lines indicate calculated results using exact analytical formulas under total mixed-injection and edge-electron injection respectively [24].

width [8] designed for the 380 nm and 600 nm excitations. For these devices, it was shown that McIntyre's *F* significantly overestimated the measured *F* for a high value of *k* (~1). In this case, the prediction error was attributed to a combination of the distributed carrier injection and the dead-space effect in the thin multiplication region [8].

Recently, the authors have reported calculated and measured excess noise factors for a speed-optimized, large area N-well/P-sub APD, which was fabricated in 0.13-μm CMOS process [9]. Here, too, *F* deviated from that provided by McIntyre's classical excess-noise formula. To obtain an accurate prediction of *F*, the authors resorted to calculating *F* using wavelength-dependent DSMT model under mixed-injection with an extensive numerical method [9]. Specifically, in addition to accounting for the electron-initiated avalanche multiplication process, hole injection and mixed-carrier injection were also taken into account in the recursive DSMT model to calculate *M* and *F* numerically while taking into account the absorption profile of N-well/P-sub CMOS APD [9]. The excess noise factor for this device was calculated using non-local Si ionization coefficients, and the results are shown in Fig. 4.5 (reproduced from [9]) with a dash-dot line.

Here we use our derived exact analytical formula for *F* under mixed injection with zero dead space to determine *F* for the N-well/P-sub APD and compare to the measured *F*, as shown in Fig. 4.5. The triangles are the measured values of *F* reproduced from [9] using a 633 nm He-Ne laser. The excess noise factor is calculated using the exact analytical formula under total mixed-injection (electron, hole and distributed injection) while taking into account local ionization coefficients of Si [16]; the results are shown in the figure by the solid line. The calculation is based on using equations (4) and (8) in [9], except that we use our analytical expressions developed in this paper with zero dead space. The *k*

value was calculated to be approximately 0.4. Note that the value of *k* for silicon is much larger at very high electric fields present in very thin multiplication regions (e.g., <400 nm [17]-[22] than that for bulk silicon) as shown in Fig. 1 in [23]. Figure 5 shows that the calculated excess-noise factors are in good agreement with the measured values for the N-well/P-sub CMOS APD.

The calculated *F* using McIntyre's formula is shown in Fig. 4.5 by the dotted line. The comparison between the excess-noise factors corresponding to McIntyre's formula (edge electron injection) and our analytical mixed-injection formula shows that McIntyre's prediction of *F* overestimates both the measured and the calculated mixed-injection *F*. This is also evident from Fig. 4.4(f), where McIntyre's *F* (for a *k* value of 0.4) overestimates the distributed *F* for narrow absorption profiles (e.g., $\alpha' = 5$ and 10). Note that the calculated *F* for both the analytical and numerical cases are slightly higher than the measured values. This could be due to the presence of non-uniform electric fields in the multiplication region of N-well/P-sub APD [9]. Additionally, dead space, which is ignored in the mixed/distributed injection formulas in this paper, also plays an important role to calculate *F* numerically with accuracy for a thin multiplication region of 270 nm for the N-well/P-sub APD as shown in [9]. This is why the DSMT is showing better agreement with measurements than that produced by the closed-form distributed-injection formula; nonetheless, the latter offers a drastic computational simplification compared to the DSMT method.

4.5 Conclusion

Easy-to-use and closed-form exact analytical formulas for the excess noise factor are derived for mixed carrier injection and distributed-carrier injection APDs as shown in

(21) and (29), respectively. The analytical results are in excellent agreement with those calculated using the exact, numerically implemented DSMT method [10]. The results are also in good agreement with experiments [9]. The newly-derived formulas reveal that in contrast to the case of edge electron injection, even with a small level of hole ionization (e.g., small k ~0.0001), the excess noise behavior exhibits a dramatic increase when mixed injection is allowed. It is also shown that the distributed-injection excess noise factor increases relative to the predictions offered by the classical McIntyre's theory, which assumes edge injection, depending on the absorption profile as it ranges from narrow to flat within the multiplication region. Comparisons show that McIntyre's predictions of the excess noise factor either underestimate or overestimate the distributed-injection F, depending on the photon absorption profile and the value of k. Hence, relying on the k value alone in predicting the excess noise factor can be very misleading in cases when mixed injection is occurring. Therefore, the simple formulas reported in this paper provide a valuable tool for optimizing the design of APD structures that exhibit even small levels of photon absorption in their multiplication regions.

Appendix

A. Exact Expressions for $z(x)$ and $y(x)$

We begin by inserting the solutions from (10a) and (10b) into (6a) and comparing coefficients, we obtain

$$c_1 + c_2 = 0 \tag{30a}$$

and

$$(r + \alpha)c_1' + \alpha c_2' = 0. \tag{30b}$$

By applying the boundary conditions, $z(w) = 1$ and $y(0) = 1$ into (10a) and (10b), we obtain

$$c_1 + c_1' e^{rw} = 1 \tag{31a}$$

and

$$c_2 + c_2' = 1. \tag{31b}$$

By solving for the unknown coefficients from (30) and (31), we can solve for $z(x)$ and $y(x)$. The solutions for unknown coefficients are deduced as follows:

$c_1 = \frac{(r+\alpha+\alpha e^{rw})}{(r+\alpha-\alpha e^{rw})}$ and $c_1' = \frac{-2\alpha}{(r+\alpha-\alpha e^{rw})}$

and

$c_2 = \frac{-(r+\alpha+\alpha e^{rw})}{(r+\alpha-\alpha e^{rw})}$ and $c_2' = \frac{2(r+\alpha)}{(r+\alpha-\alpha e^{rw})}$.

Next, we insert these values of c_1, c_1', c_2, and c_2' into (10a) and (10b), we have the following expressions for $z(x)$ and $y(x)$:

$$z(x) = \frac{(r+\alpha+\alpha e^{rw})-2\alpha e^{rx}}{(r+\alpha-\alpha e^{rw})} \tag{32a}$$

and

$$y(x) = \frac{-(r+\alpha+\alpha e^{rw})+2(r+\alpha)\, e^{rx}}{(r+\alpha-\alpha e^{rw})} \tag{32b}$$

Finally, by using the quantities of z(x) and $y(x)$, we obtain the analytical expression for the mean gain, $M(x)$ under mixed-injection given in (12).

B. Exact Expressions for $z_2(x)$ and $y_2(x)$

We begin by inserting the values of $z(x)$ and $y(x)$ into (18a) and (18b) and obtain

$$z_2'(x) + \alpha[z_2(x) + y_2(x)] = \left\{\frac{2\alpha(r+\alpha+\alpha e^{rw})^2}{(r+\alpha-\alpha e^{rw})^2}\right\} + \left\{\frac{-8\alpha\,(r+\alpha)\,(r+\alpha+\alpha e^{rw})}{(r+\alpha-\alpha e^{rw})^2}\right\} e^{rx} + \left\{\frac{8\alpha^2(2r+\alpha)}{(r+\alpha-\alpha e^{rw})^2}\right\} e^{2rx} \tag{33a}$$

and

$$z_2'(x) - \beta[z_2(x) + y_2(x)] =$$

$$\left\{\frac{-2\beta(r+\alpha+\alpha e^{rw})^2}{(r+\alpha-\alpha e^{rw})^2}\right\} + \left\{\frac{8\alpha\beta(r+\alpha+\alpha e^{rw})}{(r+\alpha-\alpha e^{rw})^2}\right\} e^{rx} + \left\{\frac{8\beta(r^2-\alpha^2)}{(r+\alpha-\alpha e^{rw})^2}\right\} e^{2rx} \quad (33b)$$

Now substitute the general solution from (19a) and (19b) into (33a) and (33b), respectively, we obtain the following equations involving p_1, p_2, p_3, p_4, p_5, q_1, q_2, q_3, q_4, q_5 with r

$$(p_4 + \alpha p_5 + \alpha q_5) + (\alpha p_4 + \alpha q_4)x + \{(r+\alpha)p_1 + p_3 + \alpha q_1\}e^{rx} + \{(2r+\alpha)p_2 + \alpha q_2\}e^{2rx} + \{(r+\alpha)p_3 + \alpha q_3\}xe^{rx} = \left\{\frac{2\alpha(r+\alpha+\alpha e^{rw})^2}{(r+\alpha-\alpha e^{rw})^2}\right\} + \left\{\frac{-8\alpha\,(r+\alpha)\,(r+\alpha+\alpha e^{rw})}{(r+\alpha-\alpha e^{rw})^2}\right\} e^{rx} + \left\{\frac{8\alpha^2(2r+\alpha)}{(r+\alpha-\alpha e^{rw})^2}\right\} e^{2rx} \quad (34a)$$

and

$$(-\beta p_5 + q_4 - \beta q_5) + (-\beta p_4 - \beta q_4)x + \{-\beta p_1 + (r-\beta)q_1 + q_3\}e^{rx} + \{-\beta p_2 + (2r-\beta)q_2\}e^{2rx} + \{-\beta p_3 + (r-\beta)q_3\}xe^{rx} = \left\{\frac{-2\beta(r+\alpha+\alpha e^{rw})^2}{(r+\alpha-\alpha e^{rw})^2}\right\} + \left\{\frac{8\alpha\beta(r+\alpha+\alpha e^{rw})}{(r+\alpha-\alpha e^{rw})^2}\right\} e^{rx} + \left\{\frac{8\beta(r^2-\alpha^2)}{(r+\alpha-\alpha e^{rw})^2}\right\} e^{2rx}. \quad (34b)$$

By comparing coefficients from (34a), we obtain

$$(p_4 + \alpha p_5 + \alpha q_5) = \frac{2\alpha(r+\alpha+\alpha e^{rw})^2}{(r+\alpha-\alpha e^{rw})^2},$$

$$(p_4 + q_4) = 0,$$

$$\left((r+\alpha)p_1 + p_3 + \alpha q_1\right) = \frac{-8\alpha(r+\alpha)(r+\alpha+\alpha e^{rw})}{(r+\alpha-\alpha e^{rw})^2},$$

$$\left((2r+\alpha)p_2+\alpha q_2\right)=\frac{8\alpha^2(2r+\alpha)}{(r+\alpha-\alpha e^{rw})^2}$$

and

$$\left((r+\alpha)p_3+\alpha q_3\right)=0.$$

Similarly, by comparing coefficients from (34b), we obtain

$$(-\beta p_5+q_4-\beta q_5)=\frac{-2\beta(r+\alpha+\alpha e^{rw})^2}{(r+\alpha-\alpha e^{rw})^2},$$

$$(p_4+q_4)=0,$$

$$(-\beta p_1+(r-\beta)q_1+q_3)=\frac{8\alpha\beta(r+\alpha+\alpha e^{rw})}{(r+\alpha-\alpha e^{rw})^2},$$

$$(-\beta p_2+(2r-\beta)q_2)=\frac{8\beta(r^2-\alpha^2)}{(r+\alpha-\alpha e^{rw})^2}$$

and

$$(-\beta p_3+(r-\beta)q_3)=0$$

Now, by applying boundary conditions, $z_2(w)=y_2(0)=1$ into (19a) and (19b), we obtain

$$p_1e^{rw}+p_2e^{2rw}+p_3we^{rw}+p_4w+p_5=1,$$

and

$$q_1+q_2+q_5=1.$$

By solving for the ten unknown coefficients from the above twelve equations, we can solve for $z_2(x)$ and $y_2(x)$. The solutions for unknown coefficients are deduced as follows

$$p_1=\frac{-8r^2\alpha(2r+\alpha-\beta)+4\alpha(2r+\alpha-\alpha e^{2rw})(r\beta-2\alpha(2r+\alpha-\beta))}{(2r+\alpha-\beta)(r+\alpha-\alpha e^{rw})^3},$$

$$p_2 = \frac{8\alpha^2(2r+\alpha-\beta)-4r\alpha\beta}{(r+\alpha-\alpha e^{rw})^2\,(2r+\alpha-\beta)},$$

$$p_3 = 0,$$

$$p_4 = 0,$$

$$p_5 = \frac{2(r+\alpha-\alpha e^{rw})^2}{(r+\alpha-\alpha e^{rw})^2} - q_5,$$

$$q_1 = \frac{-8(r+\alpha)(r+\alpha-\alpha e^{rw})}{(r+\alpha-\alpha e^{rw})^2} - \frac{-8r^2(r+\alpha)(2r+\alpha-\beta)+4(r+\alpha)(2r+\alpha-\alpha e^{2rw})(r\beta-2\alpha(2r+\alpha-\beta))}{(2r+\alpha-\beta)(r+\alpha-\alpha e^{rw})^3},$$

$$q_2 = \frac{4\beta r(2r+\alpha)}{(r+\alpha-\alpha e^{rw})^2\,(2r+\alpha-\beta)},$$

$$q_3 = 0,$$

$$q_4 = 0,$$

and

$$q_5 = 1 - (q_1 + q_2).$$

Next, we insert these values of p_1, p_2, p_3, p_4, p_5 and q_1, q_2, q_3, q_4, q_5 into (19a) and (19b), we have the following expression in the form of summation for $z_2(x)$ and $y_2(x)$:

$$z_2(x) + y_2(x) = (p_1 + q_1)e^{rx} + (p_2+q_2)e^{2rx} + (p_5 + q_5),$$

$$z_2(x) + y_2(x) =$$

$$\left\{\frac{8r^3(2r+\alpha-\beta)-4r\left(2r+\alpha-\alpha e^{2rw}\right)(\beta r-2\alpha(r+\alpha+\alpha e^{rw}))}{(2r+\alpha-\beta)(r+\alpha-\alpha e^{rw})^3} - \frac{8(r+\alpha)(r+\alpha+\alpha e^{rw})}{(r+\alpha-\alpha e^{rw})^2}\right\} e^{rx} +$$

$$\left\{\frac{8(\alpha^2(2r+\alpha-\beta)+\beta r^2)}{(r+\alpha-\alpha e^{rw})^2(2r+\alpha-\beta)}\right\} e^{2rx} + \left\{\frac{2(r+\alpha+\alpha e^{rw})^2}{(r+\alpha-\alpha e^{rw})^2}\right\},$$

In addition, we have the following expression for $z(x)$ and $y(x)$:

$$2z(x)y(x) = -\left\{\frac{2(r+\alpha+\alpha e^{rw})^2}{(r+\alpha-\alpha e^{rw})^2}\right\} + \left\{\frac{4(r+2\alpha)(r+\alpha+\alpha e^{rw})}{(r+\alpha-\alpha e^{rw})^2}\right\} e^{rx} - \left\{\frac{8\alpha(r+\alpha)}{(r+\alpha-\alpha e^{rw})^2}\right\} e^{2rx},$$

Finally, by using the quantities of z(*x*), *y*(*x*), $z_2(x)$ and $y_2(x)$, we obtain the exact analytical expression for the excess noise factor under mixed-injection given in (21).

References

[1] G. P. Agrawal, Fiber-optic communication systems, John Wiley & Sons, 2012.

[2] R. J. McIntyre, "Multiplication noise in uniform avalanche diodes," *IEEE Trans. Electron Devices*, vol. ED-13, no. 1, pp. 164-168, Jan. 1966.

[3] P. P. Webb, R. J. McIntyre, and J. Conradi, "Properties of avalanche photodiodes," *RCA Rev.*, vol. 35, pp. 234-278, June 1974.

[4] T. Kaneda, H. Matsumoto, T. Sakurai, and T. Yamaoka, "Excess noise in silicon avalanche photodiodes," *J. Appl. Physics*, vol. 47, no. 4, pp. 1605–1607, Apr.1976.

[5] C. H. Tan, J. P. R. David, G. J. Rees, R. C. Tozer, and D. C. Herbert, "Treatment of soft threshold in impact ionization," *J. Appl. Phys.*, vol. 90, pp. 2538-2543, 2001.

[6] G. Satyanadh, R. P. Joshi, N. Abedin, and U. Singh, "Monte Carlo calculation of electron drift characteristics and avalanche noise in bulk InAs," *J. Appl. Phys.*, vol. 91, no. 3, pp. 1331–1338, Feb. 2002.

[7] X. Yi, S. Xie, B. Liang, L. W. Lim, X. Zhou, M. C. Debnath, D. L. Huffaker, C. H. Tan and J. P. R. David, "Demonstration of large ionization coefficient ratio in $AlAs_{0.56}Sb_{0.44}$ lattice matched to InP," *Sci. Rep.*, vol. 8, Art. no. 17580, June 2018.

[8] A. Pauchard, P. Besse, and R. Popovic, "Dead space effect on the wavelength dependence of gain and noise in avalanche photodiodes," *IEEE Trans. Electron Devices*, vol. 47, no. 9, pp. 1685-1693, Sep. 2000.

[9] M. M. Hossain, S. Ray, J. S. Cheong, L. Qiao, A. N. A. P. Baharuddin, M. M. Hella, J. P. R. David, and M. M. Hayat, "Low-noise speed-optimized large area CMOS avalanche photodetector for visible light communication," *IEEE/OSA J. Lightwave Technol.*, vol. 35, no. 11, pp. 2315-2324, June 2017.

[10] M. M. Hayat, B. E. A. Saleh, and M. C. Teich, "Effect of dead space on gain and noise of double-carrier-multiplication avalanche photodiodes," *IEEE Trans. Electron Devices*, vol. 39, no. 3, pp. 546-552, Mar. 1992.

[11] K. F. Li, D. S. Ong, J. P. R. David, R. C. Tozer, G. J. Rees, S. A. Plimmer, K.Y. Chang, and J. S. Roberts, "Avalanche noise characteristics of thin GaAs structures with distributed carrier generation [APDs]," *IEEE Trans. Electron Devices*, vol. 47, no. 5, pp. 910-914, May 2000.

[12] C. H. Tan, J. C. Clark, J. P. R. David, G. J. Rees, S. A. Plimmer, R. C. Tozer, D. C. Herbert, D. J. Robbins, W. Y. Leong, and J. Newey, "Avalanche noise measurement in thin Si p^+- i-n^+ diodes," *Appl. Phys. Lett.*, vol. 76, no. 26, pp. 3926-3928, June 2000.

[13] M. M. Hayat, Z. Chen, and M. A. Karim, "An analytical approximation for the excess noise factor of avalanche photodiodes with dead space," *IEEE Elect. Dev. Lett*, vol. 20, no. 7, pp. 344-347, July 1999.

[14] A. G. Chynoweth, "Ionization rates for electrons and holes in silicon," *Phys. Rev.*, vol. 109, no. 5, pp. 1537-1540, Mar. 1958.

[15] M. C. Teich, K. Matsuo, and B. E. A. Saleh, "Excess noise factors for conventional and superlattice avalanche photodiodes and photomultiplier tubes," *IEEE J. Quantum Electron.*, vol. QE-22, no. 8, pp. 1184–1193, Aug. 1986.

[16] R. Van Overstraeten and H. D. Man, "Measurement of the ionization rates in diffused silicon p-n junctions," *Solid-State Electron.*, vol. 13, no. 5, pp. 583-608, May 1970.

[17] M. M. Hossain, J. Ghasemi, P. Zarkesh-Ha, and M. M. Hayat, "Design, modeling and fabrication of a CMOS compatible p-n junction avalanche photodiode," *Proc. 26th IEEE Photonics Conference*, Bellevue, WA, USA, pp. 584-585, Sept. 08-12, 2013.

[18] S. Ray, M. M. Hella, M. M. Hossain, P. Zarkesh-Ha, and M. M. Hayat, "Speed optimized large area avalanche photodetector in standard CMOS technology for visible light communication," *Proc. 13th IEEE Sensors Valencia*, Spain, pp. 2147-2150, Nov. 3-5, 2014.

[19] M. M. Hossain, P. Zarkesh-Ha, J. P. R. David, and M. M. Hayat, "Low breakdown voltage CMOS compatible p-n junction avalanche photodiode," *Proc. 27th IEEE Photonics Conference*, San Diego, CA, USA, pp. 170-171, Oct. 12-16, 2014.

[20] M. M. Hossain, P. Zarkesh-Ha, and M. M. Hayat, "Linear mode CMOS compatible p-n junction avalanche photodiode with operating voltage below 9V," *Proc. 28th IEEE Photonics Conference*, Reston, Virginia, USA, pp. 436-437, Oct. 4-8, 2015.

[21] M. M. Hossain, "Linear mode CMOS compatible pn junction avalanche photodiode for smart-lighting applications," MS Thesis, The University of New Mexico, USA, Aug. 2015. http://digitalrepository.unm.edu/ose_etds/8/

[22] M. M. Hossain and M. M. Hayat, "High responsivity double-junction CMOS-compatible avalanche photodiode," *Proc. 29th IEEE Photonics Conference*, Waikoloa, Hawaii, USA, pp. 262-263, Oct. 2-6, 2016.

[23] E. Jamil, J. S. Cheong, J. P. R. David, and M. M. Hayat, "On the analytical formulation of excess noise in avalanche photodiodes with dead space," *Opt. Exp.*, vol. 24, no. 19, pp. 21597–21608, Sept. 2016.

[24] M. M. Hossain, J. P. R. David, and M. M. Hayat, "Exact analytical formula for the excess noise factor for mixed carrier injection avalanche photodiodes," *IEEE Trans. Electron Devices*, submitted, 2018.

Chapter 5

Algorithmic Multi-color CMOS Avalanche Photodiodes for Smart-lighting Applications

5.1 Abstract

A spectral sensing algorithm is developed while taking into account photocurrent noise fluctuations from an expensive (CMOS compatible) dual-junction silicon avalanche photodiode (APD) that outputs the intensity and spectrum of the sensed illumination. This addresses the needs of smart lighting without the use of any spectral filters. The proposed dual APD device outputs two photocurrents simultaneously, one for each junction, and each junction is controlled independently via a bias voltage so that each photocurrent can exhibit its own avalanche amplification factors and sensitivity. The idea is to produce a series of photocurrent pairs, at judiciously prescribed pairs of biases for each acquisition, which would contain sufficient spectral information about the light as well as its intensity, which can be extracted from the data via the spectral sensing algorithm. Modeling shows that we can ideally use a pair of biases to detect the color and intensity within 10 nm spectral resolution in the 440-650 nm wavelength range using a maximum likelihood (ML) algorithm.

5.2 Introduction

There is a need in emerging smart-lighting concepts for a high-speed sensing capability to enable adaptive-lighting (smart spaces) and visible-light communication. One approach to address this need is to design and manufacture a low-cost, high-sensitivity

color sensor to be used in lighting enabled systems and applications. The novel sensor network will process light with right color and intensity. The color sensor will enable automatic adjust of right lighting for us at any given time, optimized for human health and productivity [1]. This chapter focuses on the advanced dual-junction CMOS avalanche photodiode (APD) to enable spectral selection as well as light intensity detection. In addition, this type of APD can offer wavelength dependent photocurrent amplification to provide better noise performance over ordinary photodiodes where thermal noise is a limiting factor.

Recent development of color sensors based on vertically-stacked multi-junction CMOS process has led to double [2], triple [3], and quad [4] junction RGB sensors. Although, the reported vertically-stacked multi-junction sensors can detect light intensity with wavelength selectivity, they cannot provide high speed and high responsivity as required for short distance visible-light communication, high-speed integrated optical receivers, optical storage systems, and high speed integrated cameras and imagers. Further enhancement of device characteristics is expected for high-speed, high-sensitivity and cost-effective color sensors. To this end, the avalanche effect in silicon can be exploited to increase their responsivity while using dual/multiple junctions to offer wavelength selectivity. The CMOS double photodiode (DPD) approach was first introduced in [5], in order to achieve faster integrated photodiodes by extending the width of the depletion region. The avalanche effect was later introduced in the double photodiode [6], which was named as the avalanche double photodiode (ADPD), and it was fabricated in 40-nm standard CMOS technology. The unity-gain responsivities were reported to be 0.15 A/W (0.038 A/W) and 0.22 A/W (0.068 A/W) for 660 nm and 520 nm, respectively, for the

PW/DNW/P-sub (P+/NW/P-sub) ADPD device structure. Most of the common design approaches, n+/p-well and p+/n-well based APD structures, fabricated in standard CMOS technology, suffered from thin absorption and multiplication regions, which led to limited responsivity.

To further increase the responsivity of CMOS APDs, the thickness of the absorption region should be as large as possible to maximize quantum efficiency while still having a CMOS-compatible design. A fast and efficient silicon *p-i-n* photodetector, fabricated in BiCMOS process, was reported in [7] with responsivities of 0.08A/W at 410 nm and 0.36 A/W at 660 nm, respectively. The responsivities were measured at a very high reverse bias voltage of 17 V, which is beyond the CMOS-circuit voltage levels. In a recent CMOS SAM APD, a high unmultiplied responsivity of 0.41 A/W was reported with 5-nW optical power using a 670-nm laser source under a reverse bias voltage of $V_0 = 0.4$ V [8]. The reported linear-mode APD was fabricated using 0.35-μm standard high-voltage CMOS process with an epitaxial wafer. One of the challenges in existing linear-mode CMOS APDs is that they need to be operated at voltages (e.g., 25, 35, 68 V) that are much higher than those allowed by the CMOS-circuit voltage levels (e.g., 9 V or less) [8-10]. In addition, low breakdown voltage APD benefits from low power operation and simple electrical bias circuitry.

More specifically, color detection methods have been reported [11], [12] for the buried double-junction (BDJ) CMOS detector, without the need for any optical filters. The first method [11] took into account the ratio of the two photo-currents (from two photodiodes) at a very low reverse bias voltage which yields monotonically increasing function of the wavelength, resulting in wavelength determination. This method of color detection

suffers from wavelength resolution. In this regard, the photo-current noise fluctuations were taken into account to determine minimum distinguishable wavelength difference, i.e., wavelength resolution [12]. However, this wavelength resolution degrades with the decrease of incident signal level. Note that both of the methods took into account unity gain photo-current ratios for color determination. Additionally, aforementioned BDJ sensors cannot provide high-speed and high-responsivity detection as required for visible-light communication. Therefore, a sophisticated spectral and light intensity detection method is required which takes into account APD gains at different bias voltages as well as photo-current noise fluctuations. The avalanche effect in silicon can be exploited to increase their responsivity while using dual-junctions to offer wavelength selectivity. This method can offer better wavelength resolution even at the presence of low level of incident signal.

In this chapter, we design and model a simple, inexpensive and high responsivity CMOS-compatible dual-junction SAM APD [13] to be operated in the linear avalanche mode with an avalanche breakdown voltage below 10 V. This device is based on an earlier single-junction design that operated at a low reverse-bias voltage of 8.5 V [14]-[16] as reported in Chapter 2 in this report. The double-junction device can offer wavelength selectivity as well as wavelength-dependent photocurrent amplification to amplify any losses due to any filter-based selectivity as reported in [17]. Specifically, we propose here a simple color detection method using maximum likelihood estimation for the high-responsivity [13] dual-junction CMOS APD. This type of APD is expected to provide wavelength selectivity through integration with the aid of post-processing, which may enable spectral resolutions higher than those available in the raw sensor data.

5.3 Spectral Sensing Algorithm Using Maximum Likelihood Estimator

The maximum likelihood estimator (MLE) is used to estimate the wavelength and intensity parameters from the dual-junction avalanche photodiodes. An spectral sensing algorithm is proposed to estimate the parameters by maximizing the log-likelihood function. Consider the noise model for the given values of photocurrent signals

$$I_1^{(1)} = I_{v_1}^{(1)} + N_{v_1}^{(1)} \tag{1}$$

and

$$I_2^{(2)} = I_{v_2}^{(2)} + N_{v_2}^{(2)} \tag{2}$$

where $I_{v_1}^{(1)}$ and $I_{v_2}^{(2)}$ are the known photocurrent signals, $N_{v_1}^{(1)}$ and $N_{v_2}^{(2)}$are the additive noise signal (i.i.d., i.e., independent and identically distributed random variables) to the photocurrent signals. The photocurrent signals are expressed as follows

$$I_{v_1} = P_0 G_{v_1}^{(1)} R_{v_1}^{(1)}(\lambda_0) \tag{3}$$

and

$$I_{v_2} = P_0 G_{v_2}^{(2)} R_{v_2}^{(2)}(\lambda_0) \tag{4}$$

where $G_{v_1}^{(1)}$ and $G_{v_2}^{(2)}$ are the mean-gains and from top and bottom photodiodes corresponding to the applied reverse bias voltages V_1 and V_2 respectively, $R_{v_1}^{(1)}$ and $R_{v_2}^{(2)}$ are the spectral responsivities. The noise signals are assumed to be i.i.d. normally distributed with photocurrent (gain noise) and thermal noise variances and are represented as follows

$$\sigma_{N_{v_1}^{(1)}}^2 = \sigma_{i_1}^2 + \sigma_{th}^2 \tag{5}$$

and

$$\sigma_{N_{v_2}^{(2)}}^2 = \sigma_{i_2}^2 + \sigma_{th}^2 \, . \tag{6}$$

The photocurrent variance $\sigma_{i_1}^2$ ($\sigma_{i_2}^2$) for an APD device for fixed (deterministic) gain $G_{v_1}^{(1)}$ ($G_{v_2}^{(2)}$) is expressed as follows

$$\sigma_{i_1}^2 = 2eG_{v_1}^{(1)}\overline{\iota_1}BF_{v_1}^{(1)} \tag{7}$$

and

$$\sigma_{i_2}^2 = 2eG_{v_2}^{(2)}\overline{\iota_2}BF_{v_2}^{(2)}, \tag{8}$$

where $F_{v_1}^{(1)}$ ($F_{v_2}^{(2)}$) is the excess noise factor at mean-gain $G_{v_1}^{(1)}$ ($G_{v_2}^{(2)}$) and B is the circuit bandwidth.

The photocurrent mean $\overline{\iota_1}$ ($\overline{\iota_2}$) for an APD for deterministic gain $G_{v_1}^{(1)}$ ($G_{v_2}^{(2)}$) is as follows

$$\overline{\iota_1} = G_{v_1}^{(1)}\eta_1\frac{e\lambda}{hc}P_0 \tag{9}$$

and

$$\overline{\iota_2} = G_{v_2}^{(2)}\eta_2\frac{e\lambda}{hc}P_0 \tag{10}$$

where η_1 and η_2 are the quantum efficiencies of top and bottom photodiodes respectively, e is the charge of an electron, h is the Planck's constant, c is the speed of light, and λ is the wavelength of light. Thermal noise is introduced to the avalanche photodiodes by the thermal motion of charged carriers in resistors and other dissipative elements associated with an optical receiver. These motions in turn yield a random thermal electric-current (whose mean value is zero) even in the absence of an external electrical power source. Therefore, the thermal noise is the electric-current variance in a resistance, R, at temperature, T and is expressed as in [18]

$$\sigma_{th}^2 = < i_{th}^2 > = \frac{4k_BTB}{R} \tag{11}$$

where K_B is the Boltzmann constant.

Now, the maximum likelihood (ML) estimates the parameter,$\hat{\theta}_{ML}$, which maximizes the joint probability density function (PDF), $f_{I_{1,}I_2}\ (i_1, i_2\ , \theta)$, for the observed values of photocurrents, i_1 and i_2. The MLE of θ is expressed as follows

$$\hat{\theta}_{ML}(\lambda, P_0)\ = \arg\max_{\theta}\ \ f_{I_{1,}I_2}\ (i_1, i_2\ , \theta) \tag{12}$$

where $\theta\ (\lambda, P_0)$ is a parameter.

Consider that the top photodiode current I_1 has a density $f_{I_1}(i_1)$ and the bottom photodiode current I_2 has a density $f_{I_2}(i_2)$. Since I_1 and I_2 are independent random variables and jointly absolutely continuous for all i_1 and i_2, the joint PDF can be written as follows

$$f_{I_{1,}I_2}\ (i_1, i_2) = f_{I_1}\ (i_1) \times f_{I_2}\ (i_2) \tag{13}$$

Since the additive gain noise and thermal noise are random, we have undertaken Gaussian distribution of PDF in order for parameter estimation. The joint PDF is expressed as follows

$$f_{I_{1,}I_2}\ (i_1, i_2) = \frac{1}{\sqrt{2\pi}\ \sigma_{N_{v_1}^{(1)}}} e^{-\frac{(i_1-\bar{i_1})^2}{2\sigma^2_{N_{v_1}^{(1)}}}} \times \frac{1}{\sqrt{2\pi}\ \sigma_{N_{v_2}^{(2)}}} e^{-\frac{(i_2-\bar{i_2})^2}{2\sigma^2_{N_{v_2}^{(2)}}}}$$

$$f_{I_{1,}I_2}\ (i_1, i_2) = \frac{1}{2\pi\sigma_{N_{v_1}^{(1)}}\ \sigma_{N_{v_2}^{(2)}}} e^{-\frac{1}{2\sigma^2_{N_{v_1}^{(1)}}\sigma^2_{N_{v_2}^{(2)}}}\ ((i_1-\bar{i_1})^2+(i_2-\bar{i_2})^2)} \tag{14}$$

However, it is convenient to use log-likelihoods since it increases the numerical stability of parameter estimates. The joint log-likelihood function is expressed as follows

$$\begin{aligned} l\left(i_1, i_2; \bar{i_1}, \sigma_{N_{v_1}^{(1)}}, \bar{i_1}, \sigma_{N_{v_2}^{(2)}}\right) = &-\ln(2\pi) - \frac{1}{2}\ln\left(\sigma^2_{N_{v_1}^{(1)}}\right) - \frac{1}{2}\ln\sigma^2_{N_{v_2}^{(2)}} \\ &- \frac{1}{2\sigma^2_{N_{v_1}^{(1)}}\sigma^2_{N_{v_2}^{(2)}}}\ ((i_1 - \bar{i_1})^2 +\ \ (i_2 - \bar{i_2})^2) \end{aligned} \tag{15}$$

The parameters of a Gaussian distribution and therefore the log-likelihood function are the mean $\bar{\iota_1}$ ($\bar{\iota_2}$) and variance $\sigma^2_{N^{(1)}_{\nu_1}}$ ($\sigma^2_{N^{(2)}_2}$). The values of mean and variance that maximize the log-likelihood function are the estimated values. Note that wavelength and light intensity parameters are embedded into the mean and variance in the log-likelihood function. In other words, the values of the wavelength and intensity parameters which maximize the log likelihood function are the desired parameters of estimation.

5.4 Application of Algorithm to a Dual Junction P+/N-well/P-sub CMOS APD

5.4.1 Device Structure

The dual-junction P+/N-well/P-sub APD device structures have been fabricated using IBM 0.13-μm CMOS process. Figure 5.1(a) shows the zoomed-in layout view of the photodiode with 20 × 20 μm^2 sub-sections and the schematic ADPD structure (350 × 350 μm^2) is shown in Fig. 5.1(b). The structure is reproduced from [19] which includes a p-substrate layer, a 1.5-μm thick N-well layer, and a 0.3-μm thick N+ layer.

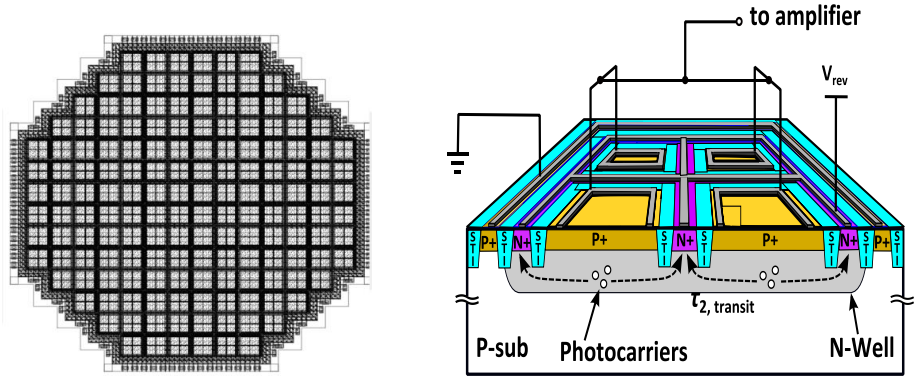

Figure 5.1: A dual-junction Si APD fabricated using IBM 0.13-μm CMOS process: (a) layout view showing 20 × 20 μm^2 sub-sections and (b) P+/N-well/P-sub structure (350 × 350 μm^2). (a)-(b) are reproduced from [19].

5.4.2 Calculation of Mean Gain and Excess Noise Factor

Wavelength dependent mean-gain and excess-noise factor (Fig. 5.4) were calculated using the non-local dead-space multiplication theory (DSMT) for the P+/N-well and N-well/P-sub APDs. The details of analytical calculation method was reported in [19]. It is assumed that the depletion region of APD is extended from $x = 0$ to $x = W$, where W is the depletion-region width. For the P+/N-well APD, the avalanche multiplication process is assumed to be initiated by the photogenerated electron at the high field ($x = 0$) and electrons travel in the positive x-direction within the depletion region ($0 \leq x \leq W$) (Fig. 5.2(a)). For the N-well/P-sub APD, the avalanche multiplication process is initiated by the photogenerated electron at the low-field ($x = W$) and electrons travel in the negative x-direction within the depletion region ($0 \leq x \leq W$) (Fig. 5.2(b)). Aside from electron-injection, the hole-injection and mixed-carrier injection multiplication process were considered in the recursive DSMT model while taking into account the absorption profile of each device [19]. The electric field, multiplication width, electron and hole dead spaces in conjunction with the Si ionization coefficients were used in the DSMT analytical model to predict the avalanche breakdown voltage, mean-gain, and the excess-noise factor while taking into account 460 nm, 542 nm, and 633 nm excitations.

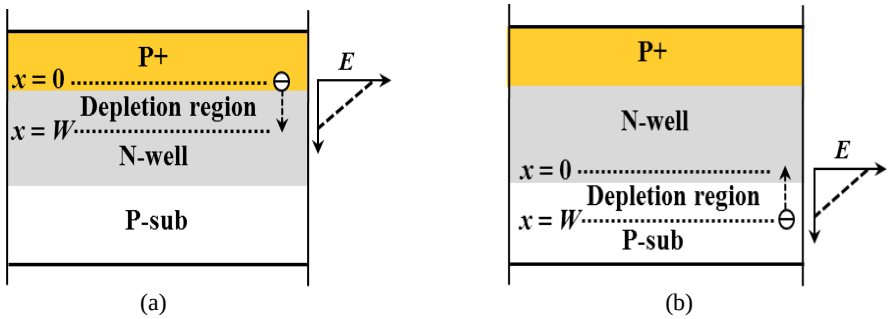

Figure 5.2: P+/N-well APD section showing direction of electron injection (a) and N-well/P-sub APD section showing the direction of electron injection (b). (a)-(b) are reproduced from [19].

5.4.3 Measurement Results

Measured dark-current as a function of applied reverse bias voltage for the P+/N-well/P-sub CMOS DAPD is shown in Fig. 5.3. A Keithley 237 source-meter was used to record

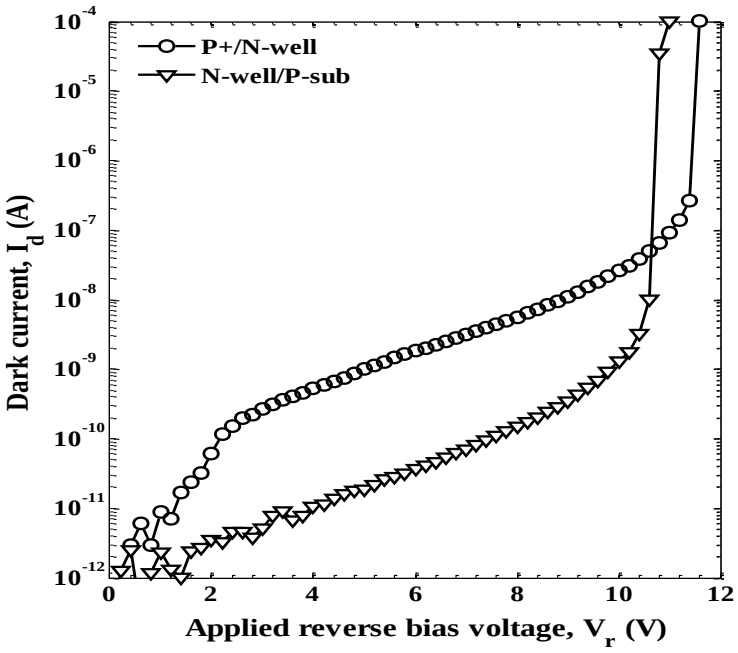

Figure 5.3: Measured dark-current as a function of applied reverse bias voltage for the P+/N-well and the N-well/P-sub APD devices.

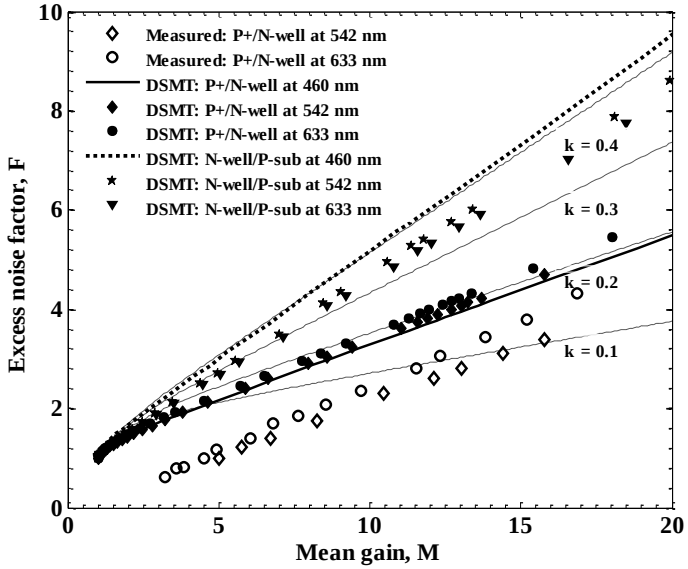

Figure 5.4: Measured excess-noise factor versus mean-gain for the P+/N-well and the N-well/P-sub APDs, respectively, using 542 nm and 633 nm lasers. The wavelength dependent excess-noise factors are calculated using non-local DSMT analytical model. McIntyre's curves are denoted with k = 0.1, 0.2, 0.3, and 0.4.

current voltage characteristics. The P+/N-well and the N-well/P-sub APDs exhibit low dark currents of ~92.3 nA and ~13.5 nA at the linear avalanche breakdown voltages of ~11 V and ~10.5 V, respectively.

The measured wavelength dependent excess-noise factor as a function of the mean-gain is shown in Fig. 5.4. For the P+/N-well APD, a very low excess-noise factor of 4.1 (4) was measured at a mean gain of 16 corresponding to a *k* value of ~0.1, using a 542 (633) nm He-Ne laser. Note that excess-noise factor was not possible to measure at the 460 nm exitation as this wavelength exhibited very low amount of photcurrents.

The measured spectral-responsivity at different applied reverse bias voltages are shown in Figs. 5.5(a) and 5.5(b), respectively for the P+/N-well/P-sub DAPD. A single grating monochromator along with a 100 W tungsten light-source were used for the spectral measurements. The bias voltage was applied to the APD device using a Keithley 236 SMU and the resultant photocurrent was recorded with a SR830 lock-in amplifier (LIA). The unity-gain responsivities were measured to be 0.01 A/W, 0.014 A/W and 0.012 A/W for 460 nm, 542 nm, and 633 nm excitations, respectively for the P+/N-well APD. For the N-well/P-sub APD, the unity-gain responsivities are 0.001 A/W, 0.022A/W, and 0.025 A/W. However, improved spectral responsivity is observed in Figs. 5.5(a) and 5.5(b), with increased reverse bias voltages. Note that higher reverse bias voltage causes widening of the depletion region and the resultant avalanche multiplication process in turn increases responsivity. For the P+/N-well APD, spectral responsivities were measured to be 0.09 A/W, 0.12 A/W, and 0.1 A/W for the 460 nm, 542 nm, and 633 nm excitations, respectively at a linear avalanche breakdown voltage of 10.4 V. For a variant N-well/P-sub APD, responsivities were reported to be 0.31 A/W, 0.47 A/W, and 0.55

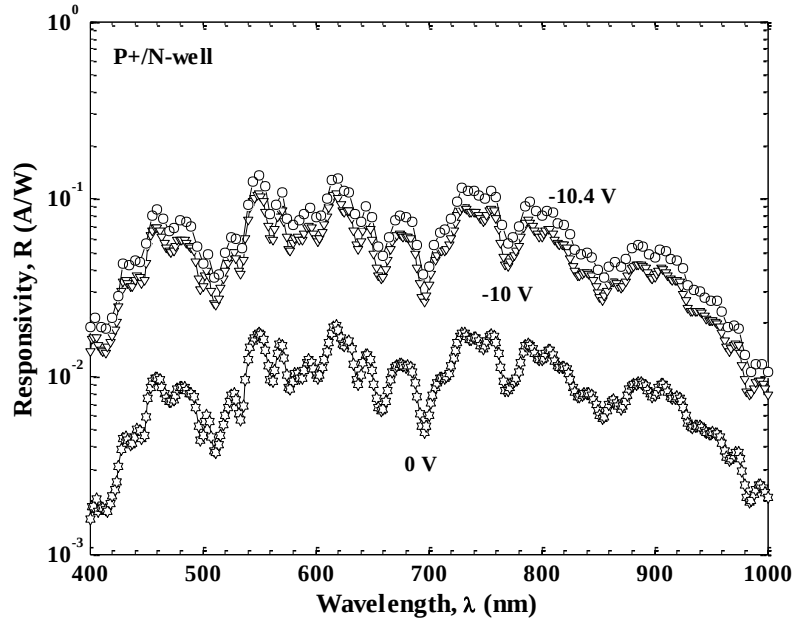

(a)

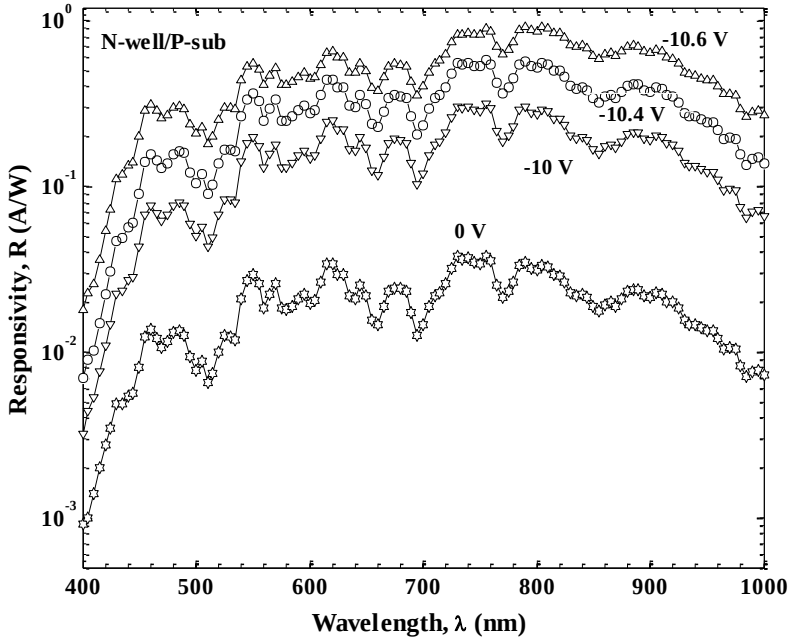

(b)

Figure 5.5: Measured spectral responsivity as a function of wavelength for the P+/N-well (a) and the N-well/P-sub (b) APDs of DAPD device.

A/W at a linear avalanche breakdown voltage of 10.6 V. The measured respsonsivity values are higher for those reported for DPAD at the 95% of breakdown voltage [6].

The ratio of the two photo-currents from the N-well/P-sub and the P+/N-well APDs as a

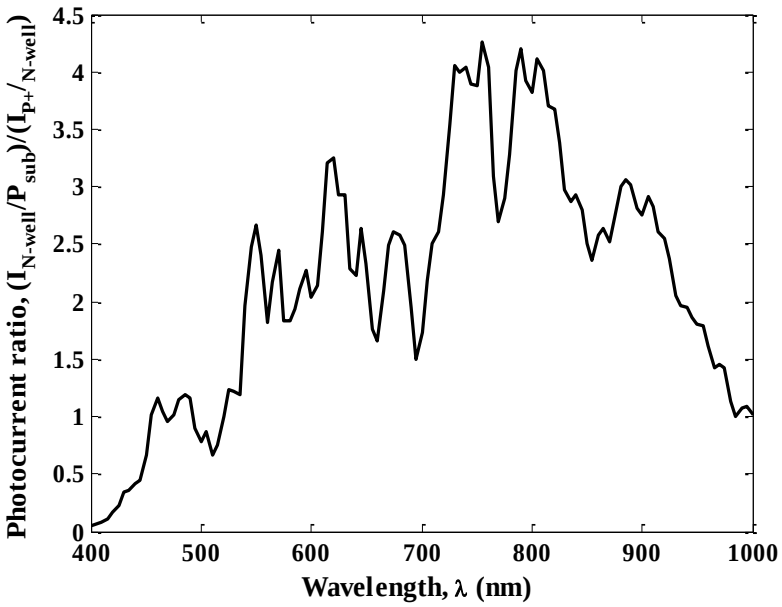

Figure 5.6: Photocurrent ratio of the N-well/P-sub and the P+/N-well APD as a function of wavelength at the applied reverse bias voltage of -10 V.

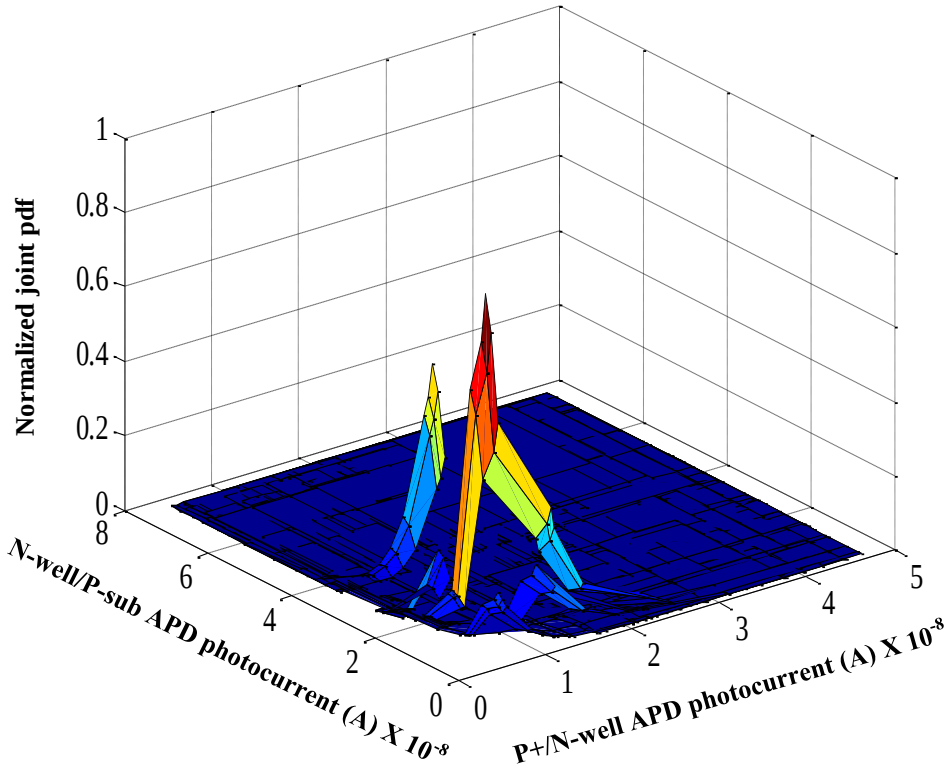

Figure 5.7: Normalized joint pdf as a function of photocurrents from the P+/N-well/Psub DAPD for the color detection using the spectral sensing algorithm. However, this dual APD yields ambiguity in color detection as different peaks appears for a particular wavelength. This is due to the excessive fluctuations in photocurrents which results from irregular transmission characteristics as light passes through the dielectric stack atop the APD surface.

function of wavelength at a applied reverse bias voltage of -10 V is shown in Fig. 5.6. In general, the photocurrent ratios from two ordinary photodiodes yields monotonically increasing function of the wavelength and is served to determine the color and intensity of the incident light [11]. However, in our case, photocurrent ratios in Fig. 5.6 show peaks which results from the optical interference in the dielectric stack above the silicon surface. Note that the P+/N-well/P-sub DAPD was fabricated using IBM 0.13-μm CMOS process. This CMOS process consists of 8 metal layers and 8 dielectric layers as well as a final passivation layer on top of the last metal layer. The metal, dielectric and passivation layers add up to the total stack. As a result, the incident light onto the device undergoes multiple reflections and refractions as well as attenuation through the Stack of materials. This results irregular transmission characteristics as a function of wavelength [20]-[21]. In addition to the total stack, 0.13 μm CMOS technology has ±20% process variation in the thickness of dielectric layers. This process variation also results highly nonlinear light transmittance through the dielectric stack [20]-[21], which yields photocurrents and responsivity fluctuations in the fabricated APDs [6]. As a result, an irregular photocurrent ratio curve as shown in Fig. 5.6 provides ambiguity in determining color and intensity of the incident light. However, the problem of irregular transmission characteristics [20]-[21], spectral response, and therefore photocurrent ratios can be resolved by using the optimized CMOS process which can replace aforementioned dielectric stack with an antireflection (AR) coating [6], [13]. The AR coating is expected to provide smooth variation of photocurrents which in turn provides light-color selectivity from the monotonically increasing photocurrent ratios as function of the wavelength.

The normalized joint pdf as a function of photocurrents from P+/N-well and N-well

APDs is shown in Fig. 5.7 The values of the wavelength and intensity parameters which maximize the likelihood function are the desired parameters of estimation. However, this dual P+/N-well/Psub APD yields ambiguity in color detection as different peaks appears for a particular wavelength. This is due to the excessive fluctuations in photocurrents which results from irregular transmission characteristics as light passes through the dielectric stack atop the APD surface. In order to get rid of this irregular transmisison charecteristics we have designed a novel dual juantion silicon APD where AR coating is used atop the APD surface, as described next.

5.5 Proposed Dual Junction Si APD with an Antireflection Coating

Proposed device structure of the CMOS-compatible double junction, SAM APD is shown in Fig. 5.8. The blue enhanced (top) *p-i-n* SAM APD consists of a *p*+ region, a 0.3 μm *p*- epitaxial layer and a *n*+ region, where *p*- layer is the absorption zone and the junction between *p* well and *n*+ region is the multiplication region. The red enhanced (bottom) *p-i-n* SAM APD consists of the *n*+ region, a 5 μm *p*- epitaxial layer and the substrate region, where the *p*- layer is the absorption zone and the junction between *n*+ and *p* well

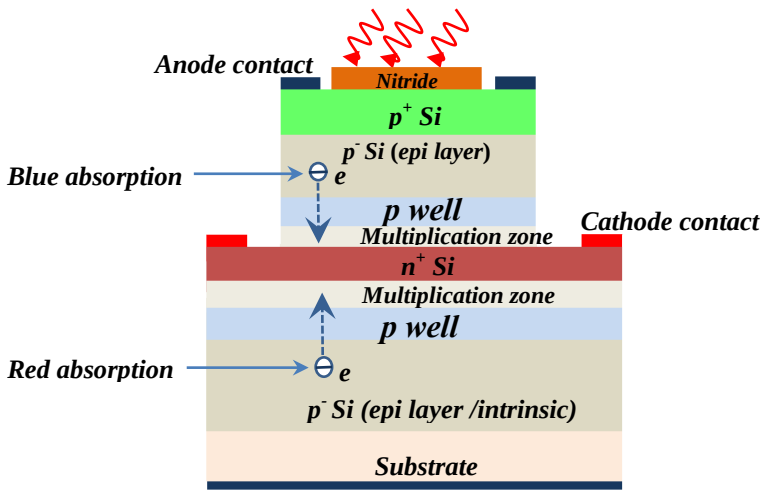

Figure 5.8: Schematic device structure of a double-junciton CMOS-compatible SAM APD [13].

is the multiplication region. A silicon nitride (SiN) layer of 77 nm is used as an anti-reflection coating.

5.5.1 Simulation Results Using Sentaurus TCAD

Simulations were performed using Technology Computer Aided Design (TCAD) Sentaurus™ tool to evaluate the optical and electrical characteristics of a two-dimensional double-junction, CMOS-compatible SAM APD device structure. Reflection, transmission and absorption spectra, zero-bias responsivity and zero-bias quantum efficiency were calculated using transmission matrix method (TMM) optical solvers in conjunction with the complex refractive index model embedded in Sentaurus TCAD [22].

A. Reflection Spectra

The illumination window of 20 μm is used to confine the incident light to a certain part of the photodiode structure. A distribution window of rays (Raytracing) is used to define the set of starting rays. The number of rays in the distribution window is specified as 300 during simulation. As a result of the above specifications, 300 rays start from an illumination window located at a distance of above the bottom surface of the SAM photodiode. These rays are distributed equidistantly to a width equal to the photodiode width. The reflectance spectra, quantum efficiency spectra, and spectral response of the photodiode are simulated by ramping the wavelength and activating the raytracer. In addition, the continuity equations for electrons and holes are solved fully coupled to the Poisson equation. Both the electrodes are kept at zero bias.

The normally incident light rays start from 0.1 μm atop photodiode and travel in the positive y-direction. The three light interaction phenomena occur throughout the device: (1) reflection of incident photons from the top surface of the photodiode; (2) absorption

of photons inside the photodiode, and (3) transmission of photons out of the bottom surface of the photodiode.

The power reflectance, $R(\lambda)$, from the top surface of the photodiode is computed as follows [22]-[24]:

$$R(\lambda) = \frac{N_{top}(\lambda)}{N_{in}(\lambda)}, \tag{16}$$

where $N_{top}(\lambda)$ is the reflected photon flux from the top surface of the photodiode and $N_{in}(\lambda)$ is the incident photon flux.

The power transmittance, $T(\lambda)$, from the bottom surface of the photodiode is computed as follows [22]-[24]:

$$T(\lambda) = \frac{N_{bot}(\lambda)}{N_{in}(\lambda)}, \tag{17}$$

where $N_{bot}(\lambda)$ is the transmitted photon flux through the bottom surface of the photodiode. These photon fluxes are related to the wavelength and the power absorbance, $A(\lambda)$, in the silicon photodiode as [22]-[24]:

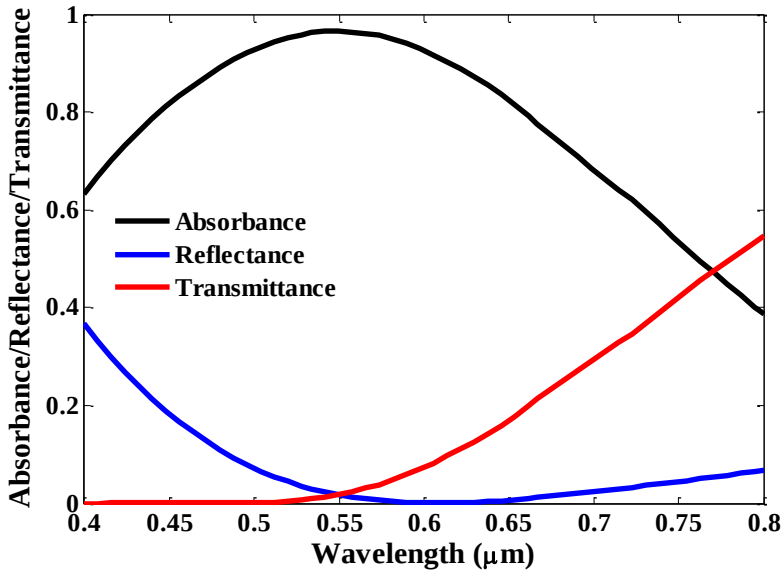

Figure 5.9: Simulated reflection, transmission and absorption spectra as a function of wavelength [13].

$$A(\lambda) = \frac{N_{abs}(\lambda)}{N_{in}(\lambda)} \tag{18}$$

Simulated reflection, transmission and absorption spectra as a function of wavelength is shown in Fig. 5.9. Optical reflectance coefficient is negligible below the 550 nm wavelength and is very low at 635 nm. Optical absorption coefficients were calculated to be 0.6 and 0.55 for 405 nm (blue region) and 635 nm (red region), respectively. In addition, the optical energy conservation is obeyed over the wavelength range 0.4 μm to 0.8 μm. For the structure under consideration and with 77 nm silicon nitride (SiN) layer thickness, the optical reflectance coefficient is almost zero below the 550 nm wavelength and is very low (0.1) at 635 nm. Optical absorbance coefficients are calculated to be 0.6 and 0.55 for 405 nm (blue region) and 635 nm (red region), respectively. For any wavelength, λ, the optical energy conservation is defined as $R + T + A = 1$.

B. Incident, Absorbed and Photogenerated Carrier Fluxes

Consider G_{opt} is the optical generation rate due to photon absorption inside APDs and $I_{ph}(\lambda)$ is photocurrent resulting from those photogenerated carriers reaching the terminals. Assume that $N_{in}(\lambda)$ (s^{-1}), $N_{opt}(\lambda)$ (s^{-1}) and $N_{ph}(\lambda)$ (s^{-1}) are the incident photon flux, photogenerated carrier flux in APD due to optical generation, and photocurrent carrier flux contributing to the photocurrent, at any applied bias, respectively. In addition, $N_{ph0}(\lambda)$ (s^{-1}), is the zero-bias photocurrent carrier flux which contributes to the zero-bias photocurrent, I_{ph0}.

In reality, the relation between the different particle fluxes is [22]-[24]:

$$N_{in}(\lambda) > N_{opt}(\lambda) > N_{ph}(\lambda). \tag{19}$$

The low value of $N_{opt}(\lambda)$ as compared to the $N_{in}(\lambda)$ arises from the optical losses as a result of reflection from top surface and transmittance at the bottom surface of the APDs.

Additionally, the value of N_{ph} (λ) is less than the N_{opt} (λ) due to recombination losses, in the bulk and at surfaces or interfaces.

The incident photon flux, $N_{in}(\lambda)$, is related to the incident light intensity, $I_{in}(\lambda)$, as

$$N_{in}(\lambda) = \frac{\lambda I_{in}(\lambda)}{hc} A_{surf}. \tag{20}$$

Incident optical power, P_{in} (λ), is related to the incident light intensity, I_{in} (λ), as

$$P_{in}(\lambda) = I_{in}(\lambda)\, A_{surf}, \tag{21}$$

where $A_{surf} = w_{tot} L_z$ and w is the total width of the photodiode in x-direction.

The absorbed photon flux, N_{abs} (λ) (s^{-1}) is computed from

$$N_{abs}(\lambda) = L_z \int_R G_{abs}(x, y, \lambda) dA, \tag{22}$$

where L_z is the width of the APD in z direction and G_{abs} (x, y, λ) ($cm^{-3}s^{-1}$) is photon absorption density at each point inside the APD.

The optical generation rate, G_{opt} ($cm^{-3}s^{-1}$), is the rate at which electron–hole pairs are generated due to absorption of photons [22]-[24]:

$$G_{opt} = \eta_{QY}\, G_{abs}, \tag{23}$$

where η_{QY} is the quantum yield which terms as the ratio of the number of electron-hole pairs generated per absorbed photon. In addition, N_{opt} (λ) and N_{ph} (λ) are computed from [22]-[24]:

$$N_{opt}(\lambda) = L_z \int_R G_{opt}(x, y, \lambda) dA. \tag{24}$$

Or,

$$N_{opt}(\lambda) = \eta_{QY}\, N_{abs}, \tag{25}$$

and

$$N_{ph}(\lambda) = \frac{I_{ph}(\lambda)}{q} \tag{26}$$

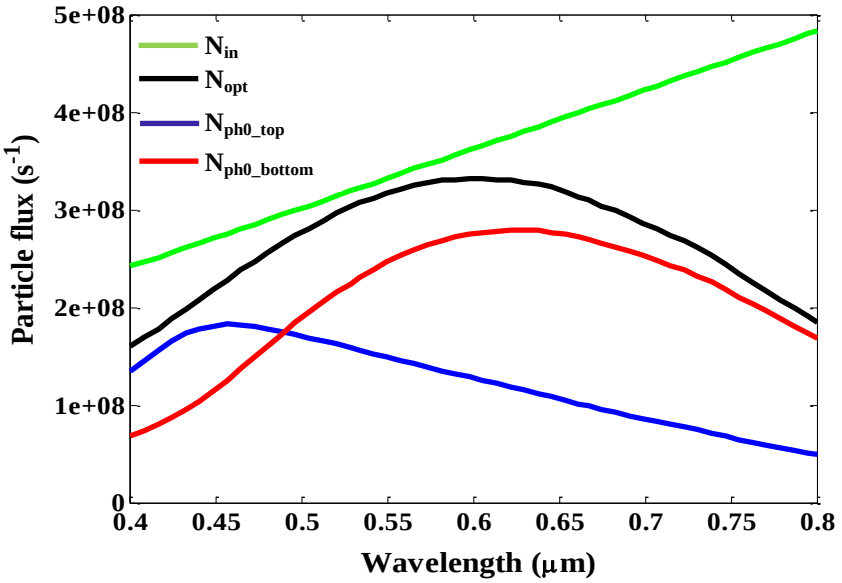

Figure 5.10: Simulated incident (N_{in}), photogenerated (N_{opt}), and zero-bias photocurrent fluxes (N_{ph0}) as a function of visible wavelenghth of light [13].

C. Quantum Efficiency and Responsivity

The quantum efficiency and responsivity (Figs. 5.11 and 5.12) are calculated using the incident, photogenerated and zero-bias photocurrent fluxes for the top and bottom photodiodes, respectively, as shown in Fig. 5.10 and are given by [22]-[24]

$$\eta_i(\lambda) = \frac{N_{ph}(\lambda)}{N_{opt}(\lambda)} \quad \text{and } \eta_{ext}(\lambda) = \frac{N_{ph}(\lambda)}{N_{in}(\lambda)} \tag{27}$$

and

$$R_{ext}(\lambda) = \frac{q\lambda}{hc}\eta_{ext}(\lambda) \text{ and } R_i(\lambda) = \frac{q\lambda}{hc}\eta_i(\lambda). \tag{28}$$

Note that the electron-hole pair generation (from photon absorption) depends on the penetration depth: long wavelength light penetrates silicon deeper than the light with short wavelength. As a result, zero-bias peak spectral responsivities were calculated to be 0.25 A/W at 450 nm and 0.38 A/W at 635 nm for the top and bottom APDs, respectively with a constant input optical power intensity of 10 mW/cm^2 (see Table 5.1).

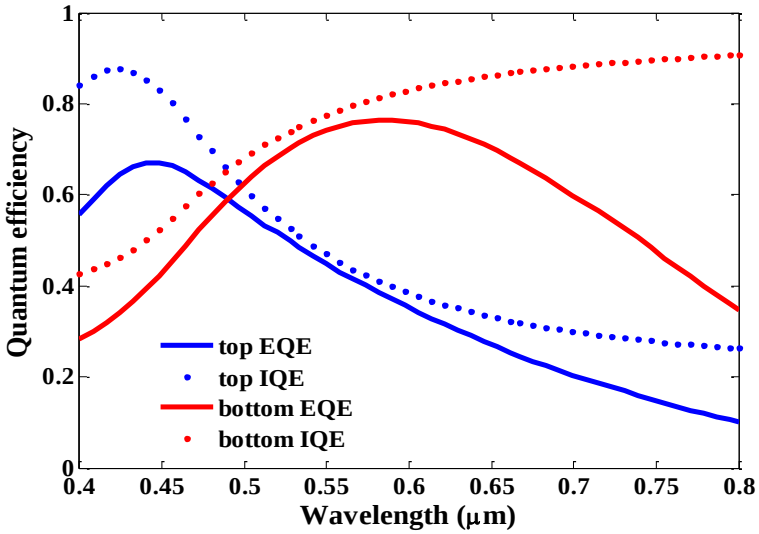

Figure 5.11: Simulated external and internal quantum efficiency (EQE and IQE) for the blue (top) and red enhanced (bottom) photodiodes, respectively [13].

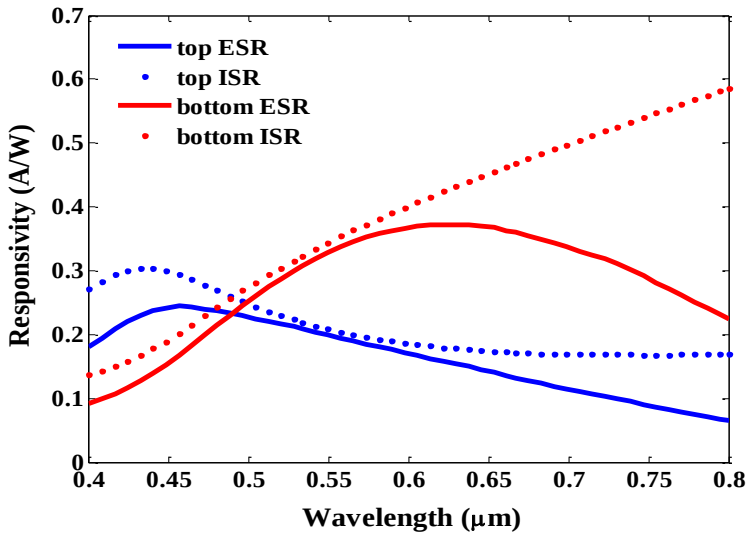

Figure 5.12: Simulated external and internal spectral responsivity (ESR and ISR) for the blue (top) and red-enhanced (bottom) photodiodes, respectively [13].

Table 5.1: Calculated zero-bias quantum efficiency and responsivity [13].

APD	Quantum efficiency	Responsivity (A/W)	Wavelength (nm)
Top	68%	0.25	450
Bottom	70%	0.38	630

5.5.2 Spectral Sensing Algorithm for the Dual-Junction SAM APD

The Technology Computer Aided Design (TCAD) Sentaurus™ Workbench, SDevice, SDE, and SVisual were used to evaluate the photo-current and responsivity characteristics of a dual-junction CMOS APD. Simulated photo-current as a function of wavelength at the reverse bias voltages of 0, -3, -5, and -7 V, respectively is shown in Fig. 5.13. The external resistor me thod was used to extract individual photocurrent I_{top} and I_{bot} from the top and bottom photodiodes, respectively at different bias voltages. The photo-currents depend on the applied reverse bias voltage as well as the incident wavelength onto the active area of the APD. Photo-current increases with the increased reverse bias voltage. Increased reverse bias voltage results widening of the depletion region in photodiode. At a linear-mode avalanche breakdown voltage, photo-generated carriers (electrons and holes) are strongly accelerated by the strong internal electric field generating secondary carriers. This avalanche process contributes to higher photo-current as well as increased quantum efficiency and spectral responsivity (see Fig. 5.14). Note that the electron-hole pair generation (from photon absorption) depends on the penetration depth: long wavelength light penetrates silicon deeper than the light with short wavelength. As a result, zero-bias peak spectral responsivities were calculated to be with a constant input optical power intensity of 10 mW/cm^2 (see Table 5.1).

Incident light on photodiodes gives rise to two photocurrents, I_{top} and I_{bot}

$$I_{top}(\lambda) = PG_{V_1}^{(top)} R_{V_1}^{(top)}(\lambda) \tag{29}$$

and

$$I_{bot}(\lambda) = PG_{V_1}^{(bot)} R_{V_1}^{(bot)}(\lambda) \tag{30}$$

0.25 A/W at 450 nm and 0.38 A/W at 635 nm for the top and bottom APDs, respectively,

where p is the incident light intensity, G_{v1} (top) and G_{v1} (bot) are the gains of top and bottom photodiodes, respectively corresponding to a applied bias voltage V_1, R_{v1} (top) and R_{v1} (bot) are the wavelength dependent spectral responsivities.

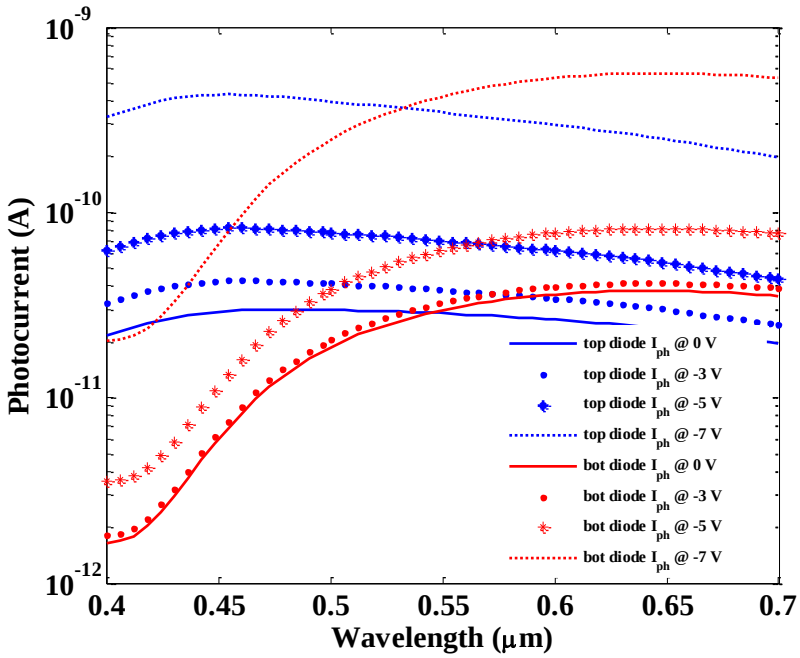

Figure 5.13: Simulated photo-current as a function of wavelength at the bias voltages of 0, -3, -5, and -7 V, respectively.

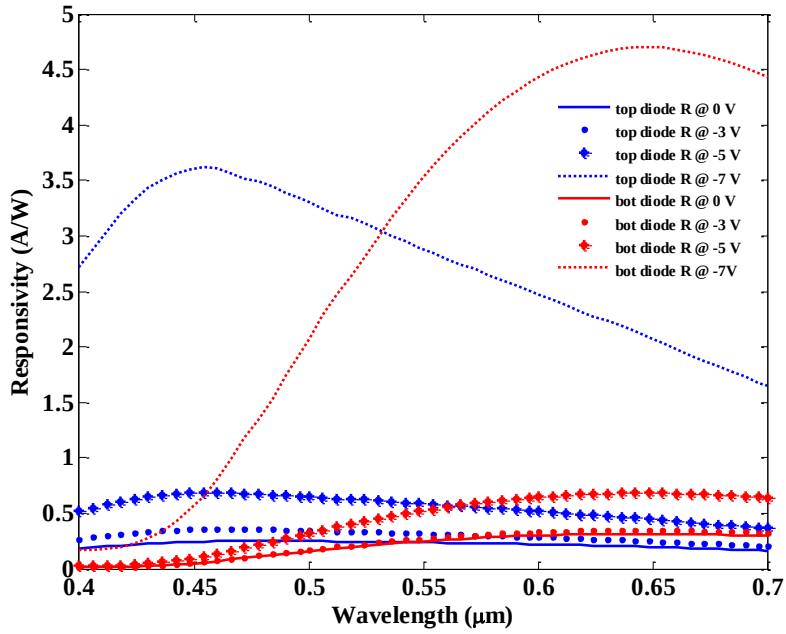

Figure 5.14: Simulated responsivity as a function of wavelength at the bias voltages of 0, -3, -5, and -7 V, respectively.

The ratio of the two photo-currents, I_{bot} (λ)/I_{top} (λ), yields monotonically increasing function of the wavelength as shown in Fig. 5.15. This curve can be served to determine color and intensity of the incident light at different bias voltages. However, this approach of color detection suffers from wavelength resolution. Color determination with better wavelength resolution is the ongoing algorithmic work while taking into account photo-current noise fluctuation and gains at different applied bias voltages. This algorithm adopts maximum likelihood estimator in order to estimate wavelength and intensity parameters of the dual-junction CMOS APD. Color detection from a dual-junction CMOS APD using the spectral sensing algorithm with ML estimator is shown in Fig. 16. The values of wavelength and intensity for which joint pdf yields maxium value are the estimated parameters. It has been shwon in Table 5.2 and 5.3 that estimated wavelengths are the 10 nm spectral resolation while taking into account photocurrent noise fluctuations in the spectral sensing algorithm.

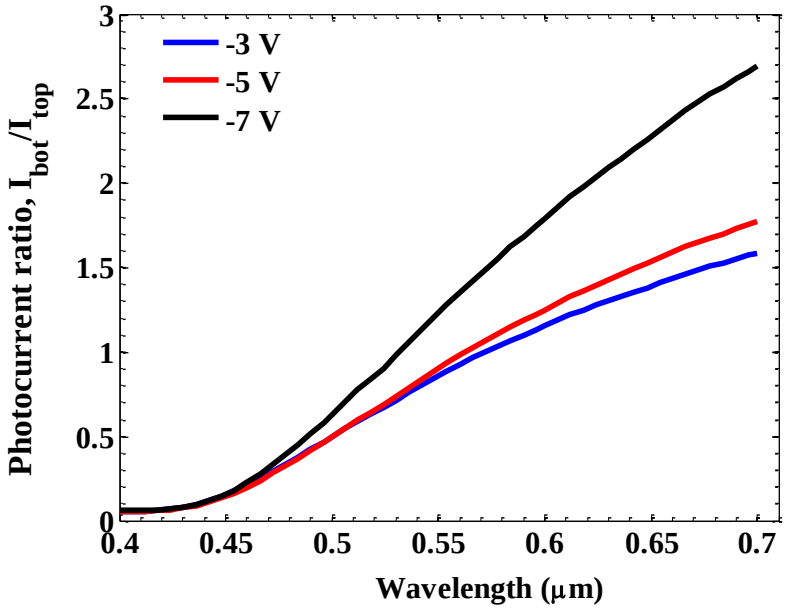

Figure 5.15: Photocurrent ratio as a function of wavelength at the bias voltages of 0, -3, -5, and -7 V, respectively.

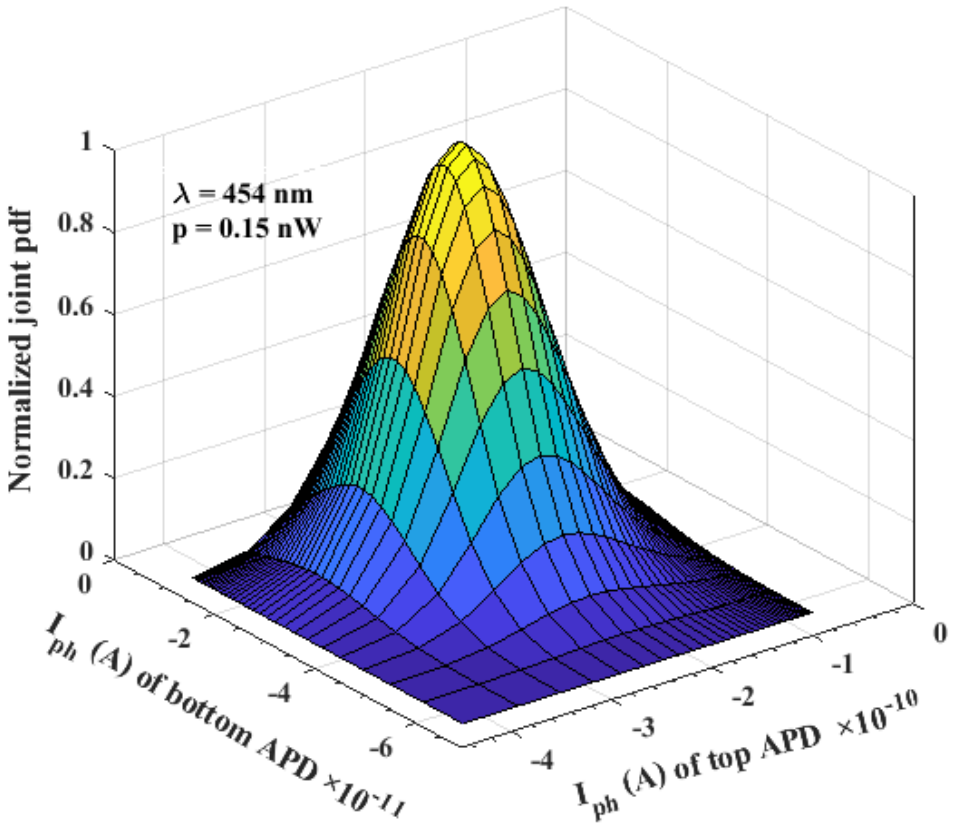

Figure 5.16: Color detection from dual-junction CMOS APD using the spectral sensing algorithm with maximum likelihood estimator.

Table 5.2: Estimated wavelength (RMSE = $\Delta\lambda$ = 4.83 nm) and optical input power

Case	APD	Noise level (A)	True λ (nm)	True P (nW)	Estimated λ (nm)	Estimated P (nW)
1	Top APD	6.76×10^{-11}	448	0.12	454	0.15
	Bottom APD	9.66×10^{-12}				
2	Top APD	4.97×10^{-11}	548	0.12	551	0.10
	Bottom APD	7.44×10^{-11}				
3	Top APD	3.11×10^{-11}	636	0.12	631	0.14
	Bottom APD	9.93×10^{-11}				

5.6 Wavelength Resolution

In order to determine wavelength resolution, noisy photocurrent signals are used in the spectral sensing algorithm. The wavelength resolution is determined as described next. The Gaussian noise is generated using MATLAB software tools with randn(*n*) function,

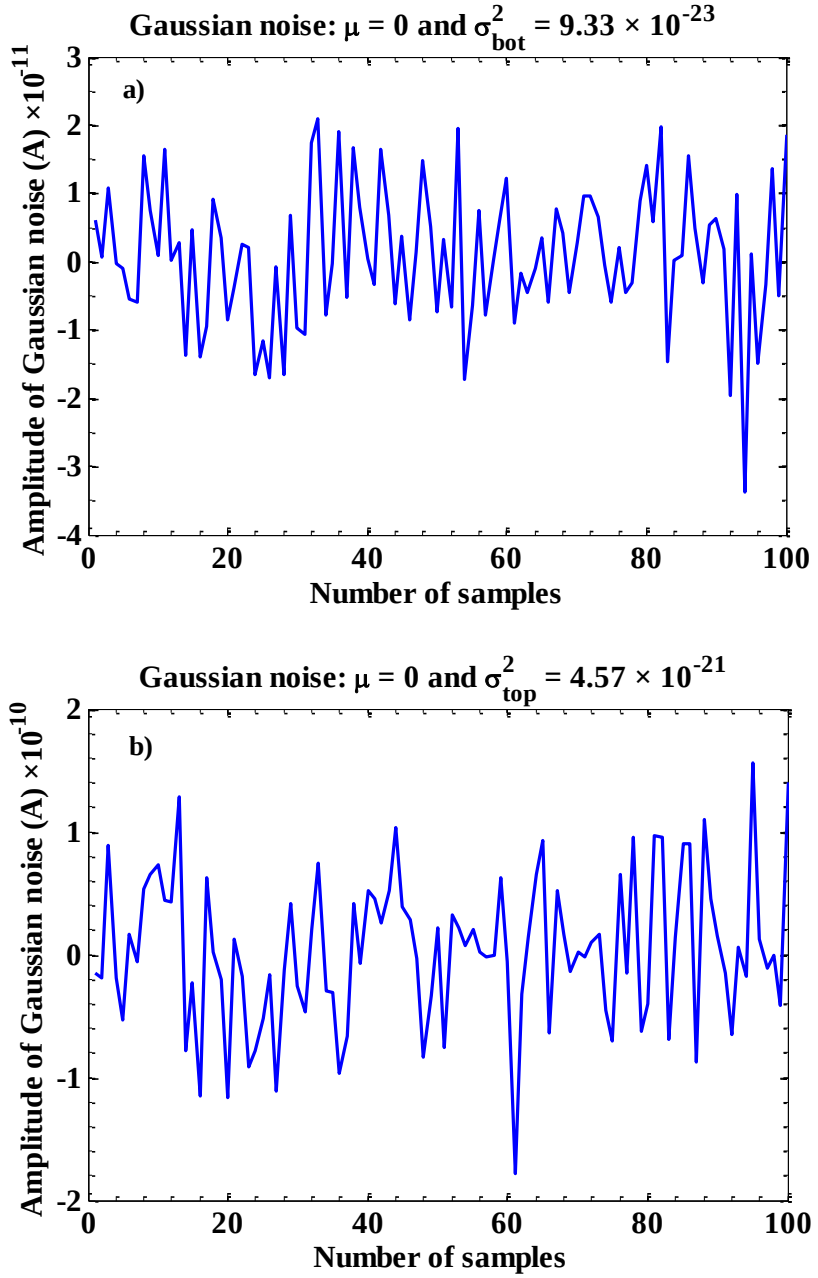

Figure 5.17: Generation of random noise (Gaussian) using MATLAB software tools with variances of 4.57×10^{-21} and 9.33×10^{-23} for the top and bottom APDs, recpectively. This randomly generated noise is added to the Semtaurus generated photocurrent signal for 448 nm wavelength.

where *n* is the number of samples. The random noise generation is based on the zero mean and total variances (thermal noise and shot noise). The choice of thermal noise stems from the fact that the value of thermal noise variance is little bit higher than the shot noise variance for the photocurrents associated with low bias voltages. The amplitude of random-Gaussian-noise is added to the Sentaurus generated photocurrent signals from the top and bottom APDs. Note that dual APD outputs two photocurrents simultaneously, one for each junction, and each junction is controlled independently via a bias voltage so that each photocurrent can exhibit its own avalanche amplification factors and sensitivity. The noisy photocurrents for a pair of applied bias voltages are used in the spectral sensing algorithm to estimate wavelength using ML estimator. The estimated wavelength deviates from true value due to the noise variance in the photocurrent signals. Therefore, an error is calculated between the estimated and actual wavelengths and squared. The above process is repeated for each of the randomly added noise to the photocurrent signals for different pair of applied bias voltages. For all the samples under consideration, root mean-square-error (RMSE), $\Delta\lambda$, is calculated. $\Delta\lambda$ is the performance parameter which indicates accuracy of predicting wavelength by using the spectral sensing model with ML estimator. The low value of $\Delta\lambda$ indicates better prediction. The error term, $\Delta\lambda$ is important because predictions are expected to be very close to the true values. The precision in $\Delta\lambda$ is obtained for the increased number of samples. To maintain the stability of $\Delta\lambda$, 40 samples are taken into consideration.

The error calculation ($\Delta\lambda$) associated with wavelength estimation is summarized in Table 5.3. It has been shown that the value of $\Delta\lambda$ decreases for high values of applied bias voltages. Then the minimum errors of 4.38, 4.31, and 4.52 are obtained for a set of

Table 5.3: Determination of wavelength resolution for the estimated wavelength (true wavelength values: 448 nm, 548 nm, and 636 nm)

Top APD bias voltage	Bottom APD bias voltage	Δλ (nm) For 448 nm	Δλ (nm) for 548 nm	Δλ (nm) for 636 nm
2	1.8	12.13	11.32	12.56
2.9	2.4	10.19	9.84	11.02
3.4	3.0	8.95	8.86	9.77
4.1	4.6	8.13	7.98	8.25
5.7	4.9	7.67	7.45	7.84
6.5	5.4	6.08	6.18	6.27
6.8	5.9	5.45	5.52	5.39
7.1	6.7	5.12	4.92	5.19
7.3	6.9	4.83	4.76	4.79
7.4	7.0	4.67	4.59	4.63
7.6	7.2	4.38	4.31	4.52
7.8	7.5	4.43	4.47	4.64
7.9	7.8	4.58	4.63	4.71
8.1	8.0	4.67	4.74	4.89
8.3	8.2	4.95	5.09	5.04
8.5	8.3	5.62	5.89	5.74
8.7	8.5	7.50	7.68	7.83
8.9	8.7	9.04	8.92	10.04

optimal bias voltages of 7.6V and 7.2 V corresponding to the top and bottom APDs, respectably. This indicates that we can estimate wavelength with a resolution of 10 nm in the spectral range of 440 to 650 nm. The minimum value of Δλ is obtained due to the increase in mean gain associated with the increased bias voltages. At this point, shot noise is clearly dominant over thermal noise. However, Δλ starts to increase for very high applied bias voltages beyond the pair of optimum bias voltages (7.6 V and 7.2 V). This is due to the fact that gain fluctuation, i.e., excess noise factor starts to play dominant role. The increase in bias voltage beyond 7.6 V and 7.2 V shows clear degradation in Δλ.

The optimal bias does not change with the estimated wavelength in the spectral range from 440 to 650 nm. However, there is a little variation in Δλ for the estimated wavelengths corresponding to the true wavelengths of 448 nm, 548 nm, and 636 nm, respectively. This is mainly due to randomly generated noise which is added to the

photocurrent signals. This covers robustness of the ML technique to the variation of wavelength for a certain range from 440 nm to 650 nm.

5.7 Conclusion

Design and modeling of a dual-junction Si CMOS APD are presented. The calculated results of reflection, transmission and absorption spectra, responsivity and quantum efficiency are also reported. More specifically, a spectral sensing algorithm has been developed to enable color (visible) and intensity selectivity by means of post-processing using maximum likelihood estimation. The spectral resolution is within 10 nm for the wavelength range from 440 nm to 650 nm while taking into account photocurrent noise fluctuations. The reported device benefits from the high-speed sensing capability required for the lighting enabled systems and applications including adaptive lighting and visible light communication.

5.8 Future Work

The following research goals that we plan to focus in the near future: (1) Fabrication dual-junction (blue and red enhancement) CMOS Si APD using 0.35-μm AMS process; (2) Measurements of quantum efficiency, spectral responsivity, avalanche breakdown voltage, mean-gain and excess-noise factor for the fabricate APDs; (3) Use of the developed spectral-sensing algorithm to determine color and intensity of the light by means of post-processing; and (4) Test the devices for adaptive-lighting and VLC systems.

References

[1] https://lesa.rpi.edu/

[2] Z. Zhan, B. Zhoua, Z. Fu, F. V.Bright, A. N. Cartwrighta, C. M. Bartsch, A. H. Titus, "Filterless optical oxygen sensor based on a CMOS buried double junction photodiode," *Sensors and Actuators B: Chemical*, vol. 176, pp. 729-735, Jan. 2013.

[3] http://www.foveon.com/article.php?a=67

[4] C. Richard, T. Courcier, P. Pittet, S. Martel, L. Ouellet, G-N Lu, V. Aimez, and P. G. Charette, "CMOS buried Quad p-n junction photodetector for multi-wavelength analysis," *Opt. Express*, vol. 20, no. 3, pp. 2053-2061, Jan. 2012.

[5] H. Zimmermann, K. Kieschnick, T. Heide, and A. Ghazi, "Integrated high-speed, high-responsivity photodiodes in CMOS and BiCMOS technology," *Proc. 29th Eur. Solid-State Dev. Res. Conf.*, Leuven, Belgium, pp. 332-335, 13-15 Sept. 1999.

[6] M. Atef, A. Polzer, and H. Zimmermann, "Avalanche double photodiode in 40-nm standard CMOS technology," *IEEE J. Quantum Electron.*,vol. 49, no. 3, pp. 350–356, Mar. 2013.

[7] A. Nemecek, G. Zach, R. Swoboda, K. Oberhauser, and H. Zimmermann, "Integrated BiCMOS p-i-n photodetectors with high bandwidth and high responsivity," *IEEE J. Sel. Topics Quantum Electron.*,vol. 12, no. 6, pp. 1469 – 1475, Nov./Dec. 2006.

[8] B. Steindl, R. Enne, S. Schidl, and H. Zimmermann, "Linear mode avalanche photodiode with high responsivity integrated in high-voltage CMOS," *IEEE Electron Device Lett.*, vol. 35, no. 9, pp. 897 – 899, Sept. 2014.

[9] B. Steindl, W. Gaberl, R. Enne, S. Schidl, K. Schneider-Hornstein, and H. Zimmermann, "Linear mode avalanche Photodiode with 1-GHz bandwidth fabricated in 0.35-µm CMOS," *IEEE Electron Device Lett.*, vol. 26, no.15, pp. 1511 – 1514, Aug. 2014.

[10] F. Villa, D. Bronzi, Y. Zou, C. Scarcella, G. Boso, S. Tisa, A. Tosi, F. Zappa, D. Durini, S. Weyers, U. Paschen, and W. Brockherde, "CMOS SPADs with up to 500 µm diameter and 55% detection efficiency at 420 nm," *J. Modern Opt.*, vol. 61, no. 2, pp. 102-115, Jan. 2014.

[11] G. N. Lu, M. B. Chouikha, G. Sou, and M. Sedjil, "Colour detection using a buried double p-n junction structure implemented in the CMOS process," *Electron. Lett.*, vol. 32, pp. 594-596, Mar. 1996.

[12] G. N. Lu, G. Sou, F. Devigny, and G. Guilland, "Design and testing of a CMOS BDJ detector for integrated microanalysis systems," *Microelectron. J.*, vol. 32, no. 3, pp. 227-234, Mar. 2001.

[13] M. M. Hossain and M. M. Hayat, "High responsivity double-junction CMOS-compatible avalanche photodiode," *Proc. 29th IEEE Photonics Conference*, Waikoloa, Hawaii, USA, pp. 262-263, Oct. 2-6, 2016.

[14] M. M. Hossain, J. Ghasemi, P. Zarkesh-Ha, and M. M. Hayat, "Design, modeling and fabrication of a CMOS compatible *p-n* junction avalanche photodiode," *Proc. 26th IEEE Photonics Conference,* Bellevue, WA, USA, pp. 584-585, Sept. 08-12, 2013.

[15] M. M. Hossain, P. Zarkesh-Ha, J. P. R. David, and M. M. Hayat, "Low voltage CMOS compatible p-n junction avalanche photodiode," *Proc. 27th IEEE Photonics Conference,* La Jolla, San Diego, CA, USA, pp. 170-171, Oct. 12-16, 2014.

[16] M. M. Hossain, P. Zarkesh-Ha, and M. M. Hayat, "Linear mode CMOS compatible p-n junction avalanche photodiode with operating voltage below 9V," *Proc. 28th IEEE Photonics Conference*, Reston, Virginia, USA, pp. 436-437, Oct. 4-8, 2015.

[17] A. Neumann, J. Ghasemi, S. Nezhadbadeh, X. Nie, P. Zarkesh-Ha, and S. R. J. Brueck, "CMOS-compatible plenoptic detector for LED lighting applications," *Opt. Express*, vol. 23, no. 18, pp. 23208-23216, Aug. 2015.

[18] B. E. A. Saleh and M. C. Teich, Fundamentals of Photonics, New York:Wiley, 2007.

[19] M. M. Hossain, S. Ray, J. S. Cheong, L. Qiao, A. N. A. P. Baharuddin, M. M. Hella, J. P. R. David, and M. M. Hayat, "Low-noise speed-optimized large area CMOS avalanche photodetector for visible light communication," *IEEE/OSA J. Lightwave Technol.*, vol. 35, no. 11, pp. 2315-2324, June 2017.

[20] F. Tavernier and M. S. J. Steyaert, "High-speed optical receivers with integrated photodiode in 130 nm CMOS," *IEEE J. Solid-State Circuits*, vol. 44, no. 10, pp. 2856-2867, Oct. 2009.

[21] B. Nakhkoob, S. Ray, and M. M. Hella, "High speed photodiodes in standard nanometer scale CMOS technology: a comparative study," *Opt. Exp.*, vol. 20, no. 10, pp. 11256-11270, May 2012.

[22] Sentaurus™ Device User Guide, 2015.

[23] Sentaurus Technology Template: Simulation of 2D n+-on-p HgCdTe photodiode with raytracer, 2013.

[24] Sentaurus Technology Template: Simulation of 2D single-junction GaAs solar cell, 2014.